Exploration of binary metallic systems for plasmonic applications and stimulated electron energy gain spectroscopy of plasmonic nanostructures

A Dissertation Presented for the

Doctor of Philosophy

Degree

The University of Tennessee, Knoxville

Robyn Marie Collette

August 2020

DEDICATION

To Ollie, my faithful companion.

ACKNOWLEDGEMENTS

First of all, I am thankful to my parents, John and Lisa, for always encouraging me to follow my dreams. They have been my number one fans and have always had a listening ear when it comes to my studies. I am also thankful to my siblings, Cory and Sam, and to my fiancé, Carl.

Thank you to my mentors at Shippensburg University, Dr. Allen Armstrong and Dr. Kate Shirk, who sparked my interest in the field of nanoscience and encouraged me to pursue my graduate degree. Thank you to my running community, RunKNOX, which encouraged me to keep pace and push through stressful times. To my running partners who entertained hours of conversation on the run. I am thankful to my church community at Emmanuel Assembly of God, who welcomed me as family and has served as a listener and prayer partner through my time at UT.

Thank you to all my coworkers in graduate school for their friendship. Specifically, Dr. Yueying Wu for training me in in the realm of thin films and cleanroom processes and having many useful conversations. Thank you to David Garfinkel for enduring many hours helping me with laser TEM troubleshooting and data collection and to Grace Pakeltis for our many plasmon discussions and help in the lab. Thank you to John Dunlap for training me on the TEM at JIAM and allowing us to use the microscope for hours on end to complete our experiments. I am also thankful to Michael Kohler and the JIAM Diffraction Facility for assistance with diffraction experiments and helpful discussions related to diffraction data analysis. I am also grateful to the staff members at the Center for Nanophase Materials Science at ORNL for always lending a helpful hand with training and troubleshooting equipment in the cleanroom. Thank you also to my committee members, Jason Fowlkes, Gerd Duscher, and Gong Gu for your feedback and suggestions.

Finally, thank you to my advisor, Philip Rack, for accepting me into his group as a second-year graduate student. Thank you for being an exemplary model in leadership, research, and communication. Thank you for always encouraging me to strive for my best. I am truly grateful to have been part of your research team.

ABSTRACT

This dissertation fully interrogates two bimetallic material systems for plasmonic applications and also evaluates the ability of a new optical delivery system mounted on a (S)TEM for stimulated near field imaging of plasmonic modes.

Plasmonics involves the collective oscillation of free electrons which are weakly bound to lattice ions. Despite the term 'plasmonics' being coined as the name for the field of study only in 2001, plasmonics has played a role in history dating back to the famous Lycurgus cup in the 4th century AD which displays a red color in transmission and a green color in reflection due to the presence of metal nanoparticles. Current plasmonics research is driven by developments in optical antennas, photothermal therapy for cancer, sensing, photovoltaics, and metamaterials. Silver and gold have been at the forefront of plasmonic materials due to strong local field enhancement, low losses, and biocompatibility (gold). Recently, however, significant research is devoted to finding novel plasmonic materials which overcome the limitations of traditional materials. Additionally, advancement in characterization methods is beneficial for increased understanding of plasmonic materials.

In Chapter 1, the fundamentals of plasmonics are presented. The dielectric function and characterization methods are discussed with a focus on electron energy loss and gain spectroscopy. Additionally, examples of popular plasmonic materials are presented for monatomic materials and bimetallic materials. Chapters 2 and 3 explore two binary metallic systems, Au-Al (Chapter 2) and Au-Ni (Chapter 3), as potential plasmonic materials. Mixed metallic alloys are an important exploratory pathway to tune the plasmon resonance or combine or combine plasmonic properties with other functionalities. These studies explore the full compositional space of the two mixed systems by correlating the optical properties with composition and crystallographic phases. Chapter 4 explores optically stimulated near field imaging of plasmonic nanostructures. A (S)TEM mounted optical delivery system developed by Waviks Inc. is used to optically stimulate Au nanorods. We demonstrate the ability to image the near field of the m = 1, 2, and 3 longitudinal localized surface plasmon modes using cw excitation.

TABLE OF CONTENTS

LIST OF TABLES

LIST OF FIGURES

Chapter 1

Introduction

1.1. Background

Despite the term 'plasmonics' being coined as the name for the field of study only in 2001[1], plasmonics has played a role in history dating back to the famous Lycurgus cup in the 4th century AD which displays a red color in transmission and a green color in reflection due to the presence of gold nanoparticles[2]. Fast forward to present day, plasmonic materials find uses in sensors[3], catalysts[4], photovoltaics[5], biomedical applications[6], and electronics[7]. A plasmon is defined for metals as a collective oscillation of free electrons which are weakly bound to the lattice ions[8]. A volume plasmon is a longitudinal oscillation which occurs within a bulk metal. Volume plasmons can only be excited by the impact of a particle and are typically measured through electron energy loss spectroscopy (EELS). The complex dielectric function of an ideal metal is described by the Drude model,

$$\varepsilon(\omega) = 1 - \frac{\omega_p^2}{\omega^2 + i\gamma\omega}, \tag{1.1}$$

where γ is the electron collision frequency (damping term) and ω_p is the frequency of the volume plasmon expressed as,

$$\omega_p = \sqrt{\frac{ne^2}{\varepsilon_0 m}}, \tag{1.2}$$

where *n* is the free electron density of the material, *e* is the charge of the electron, *m* is the electron mass, and ε_0 is permittivity of free space. Most metals have a volume plasma frequency in the UV region due to a large free electron density; some common metals will be discussed below[8].

A plasmon confined to the surface of a metal is called a surface plasmon. The surface plasmon occurs when electrons are bound to oscillate between a metal and a dielectric interface. Surface plasmon polaritons (SPP) are a subset of surface plasmons which propagate along the metal surface when the incident electromagnetic wave couples to the electron cloud of the metal at its surface. In order to excite an SPP, the momentum of the surface plasmon must be matched to that of the incident light which is commonly done

using prism coupling or grating[8]. Common techniques for exciting an SPP include the Grating, Otto, and Kretschmann configurations.

A localized surface plasmon resonance (LSPR) occurs when light couples with the free electrons of a structure whose size is similar to the wavelength of light. As its name suggests, these plasmon excitations are localized and non-propagating. LSPRs can be excited directly by light. An applied external field causes the conduction electrons of a material to be displaced from the positively charged lattice ions. The Coulomb attraction acts as a restoring force causing a resonance to occur between the electrons and lattice[9]. The LSPR frequency refers the frequency of the electron oscillation. For particles much smaller than the wavelength of light, the electrostatic approximation can be applied, effectively treating the system as a mass on a spring. Upon solving the Laplace equation with appropriate boundary conditions, the polarizability of the sphere is described as,

$$\alpha = 4\pi a^3 \frac{\varepsilon - \varepsilon_m}{\varepsilon + 2\varepsilon_m} \tag{1.3}$$

where a is the radius of the particle, ε is the complex dielectric function of the particle, and ε_m is the dielectric function of the surrounding medium. The polarizability describes how easily an external electric field may displace electrons within an object and is enhanced when the denominator is a minimum[9]. If $Im(\varepsilon)$ is small near the resonance frequency, the minimization for the denominator is written as

$$Re(\varepsilon) = -2\varepsilon_m. \tag{1.4}$$

This is called the Frölich condition and the wavelength satisfies this condition is the wavelength of the dipolar LSP. Furthermore, the polarizability dictates the degree of strength to which a particle may scatter and absorb light[9]. The scattering and absorption cross sections can be calculated using the polarizability as,

$$C_{sca} = \frac{k^4}{6\pi}|\alpha|^2 = \frac{8\pi}{3}k^4 a^6 \left|\frac{\varepsilon - \varepsilon_m}{\varepsilon + 2\varepsilon_m}\right|^2 \tag{1.5}$$

$$C_{abs} = k\mathrm{Im}[\alpha] = 4\pi k a^3 Im\left[\frac{\varepsilon - \varepsilon_m}{\varepsilon + 2\varepsilon_m}\right] \tag{1.6}$$

where k is $2\pi/\lambda$, a is the radius of the particle, ε is the dielectric function of the particle, and ε_m is the dielectric function of the surrounding medium[8]. These cross sections depend

on the polarizability and consequently depend on the LSPR. A method to characterize the LSPR using scattering and absorption will be discussed later. The electrostatic approximation holds well for particles much smaller than the wavelength of light. For larger structures, retardation effects need to be considered. Additionally, higher order multipoles have an increasing contribution as the size of the structure gets larger and the bulk plasma frequency limits the range of energy allowed for the LSP modes[10]. Hence, for larger particles that cannot be approximated by a dipole, Mie Theory is required which involves solving Maxwell's equations to describe how electromagnetic radiation is absorbed and scattered in a sphere.

1.2. The Dielectric Function

The plasmonic response of a material is governed by its complex dielectric function where the real part describes the polarizability of the material and the imaginary part describes the losses (absorption) in the material[11–13]. Consequently, the dielectric function has been studied in great detail for many materials[14]. Two common methods to measure the dielectric function of a material are reflection/transmission and ellipsometry[15]. The former requires measuring the intensity of light reflected by and transmitted through a material which can then be used to determine the dielectric function. Spectroscopic ellipsometry, measures how the polarization of light changes upon reflection on a material. Specifically, the amplitude ratio (psi) and phase difference (delta) of the polarized light are measured as illustrated in **Figure 1.1**. Initially, light with equal amounts of parallel (p) and perpendicular (s) polarized components is directed at an angle, θ, onto a sample. The light is reflected off the sample surface; due to the dielectric function, the phase of one component of the light will be delayed compared to the other and the amplitude will also be different. The phase difference, Δ, and amplitude difference, Ψ, are reported over the range of energies measured. Assuming an optical model which has an infinitely thick film on a flat substrate, we can arrive at the pseudo-dielectric function directly from the measured ellipsometric values, Ψ and Δ:

$$\langle \varepsilon \rangle = sin^2\,\theta_i \left[1 + tan^2\,\theta_i \left(\frac{1 - tan\Psi\; e^{i\Delta}}{1 + tan\Psi\; e^{i\Delta}} \right)^2 \right] \tag{1.7}$$

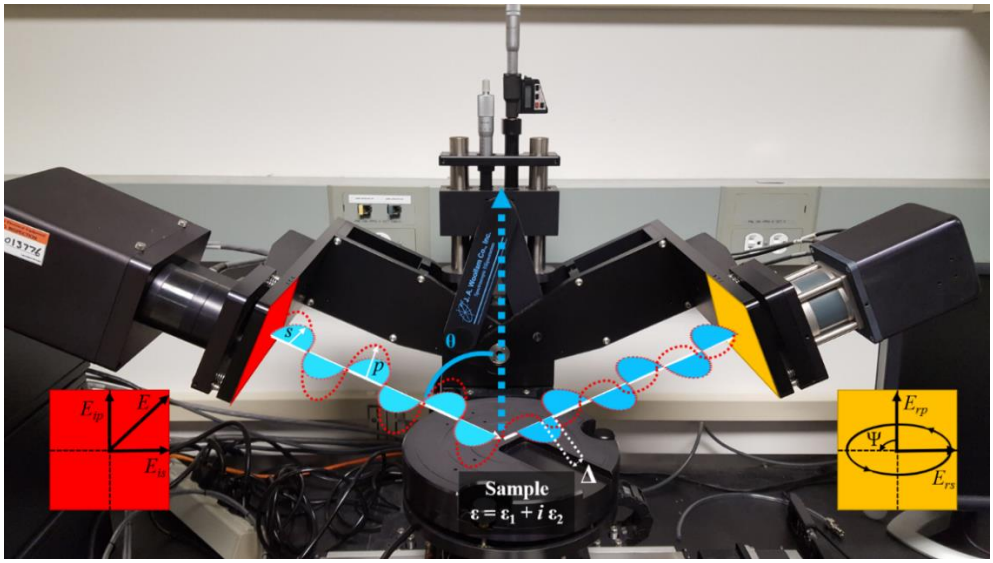

Figure 1.1. Geometry of spectroscopic ellipsometry instrument and measurement.

where, θ_i is the incident angle of light[15].

As mentioned above, the dielectric function of an ideal metal can be described by the Drude model. In reality, however, very few metals are accurately described by the Drude model due to interband transitions which modify the complex dielectric function. The Drude model only accounts for the free electron behavior. Interband transitions are typically represented by a number of Lorentz oscillators. Combining these gives the Drude-Lorentz model[16];

$$\varepsilon(\omega) = \varepsilon_\infty - \frac{\omega_p^2}{\omega^2 - i\omega\gamma} + \sum_{j=1}^{N} \frac{f_j \omega_{0j}^2}{\omega_{0j}^2 + \omega^2 + i\Gamma_j \omega} \tag{1.8}$$

where ε_∞ is the high frequency dielectric constant, f_j is an amplitude term, ω_{0j}^2 is the energy of the interband transition, and Γ_j is a broadening term. In some cases, an arbitrarily large number of Lorentz oscillators are required to accurately capture the behavior of the dielectric function. However, this is unphysical and consequently, other models have been proposed to replace the Lorentz oscillators. One group utilizes a modified Lorentzian which incorporates a phase term which allows for asymmetric line shapes and has demonstrated

success in representing the dielectric function of gold using the Drude component with two modified Lorentz terms[17]. Others have employed band structure analysis to better represent the dielectric function. Critical points in the joint density of states (jDOS) contribute to important features in the dielectric function and thus, by accurately modeling the jDOS, the dielectric function can also be modeled. They demonstrated this model worked for a range of Au-Ag alloys as well as the pure constituents utilizing the Drude model with two critical point terms[18,19]. The various models discussed here are demonstrated in **Figure 1.2** for gold in comparison with experimental data.

Using the dielectric function, we can introduce the quality factor (Q) which estimates the efficacy of the material for plasmonic applications in the optical region of interest[20]. Quality factors are application and geometry specific and thus many expressions of Q exist. The quality factors for LSPRs, surface plasmon polaritons, transformation optics, and super lenses are discussed in reference[11]. The quality factor for an LSPR is a ratio of the local field enhancement to the incident field and is given for a sphere by[11],

$$Q_{LSPR}(\omega) = -\frac{\varepsilon_1(\omega)}{\varepsilon_2(\omega)} \tag{1.9}$$

where ε_1 is the real part of the dielectric function and ε_2 is the complex part of the dielectric function. Higher values of Q_{LSPR} are desired for a sharp resonance with strong near field enhancement[21]. The LSPR quality factor of a sphere is plotted for various metals as a function of wavelength in **Figure 1.3**.

The plasmonic response of a structure depends on many factors. The dielectric function is an intrinsic material property, and consequently the plasmonic response of a material depends on the material itself. **Figure 1.4a** shows the extinction spectrum for similar sized Ag, Au, and Cu nanoparticles, demonstrating the dependence of the LSPR on the material. Interband transitions associated with a material may limit the energy range that a strong LSP can be supported. The dielectric function of the surrounding environment also modifies the energy of the LSPR. The LSPR energy of Au nanospheres embedded in a TiO2 film is sensitive to the position of the nanosphere in the film[22]. Substrate effects on the LSPR properties has also been studied[23].

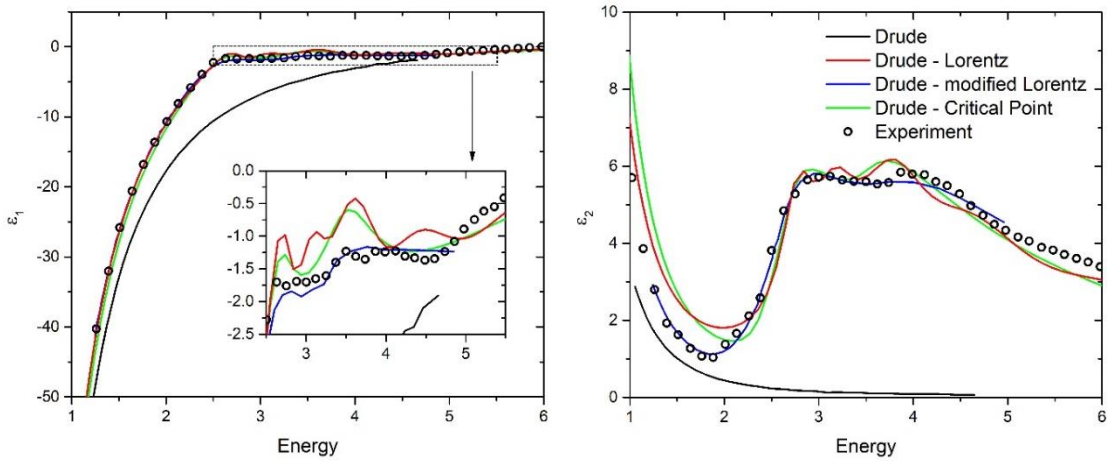

Figure 1.2. Real and imaginary components of the Au dielectric function for the Drude[18], Drude-Lorentz[19] (5 Lorentz terms), Drude-modified Lorentz[17], and Drude-critical point[19] models compared with experiment[24] .

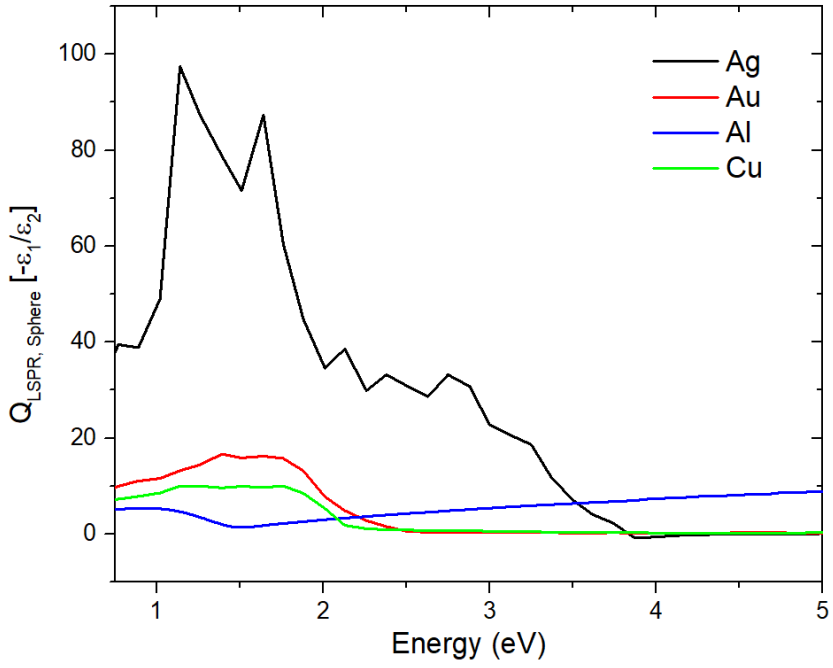

Figure 1.3. LSPR quality factor for various metals[11].

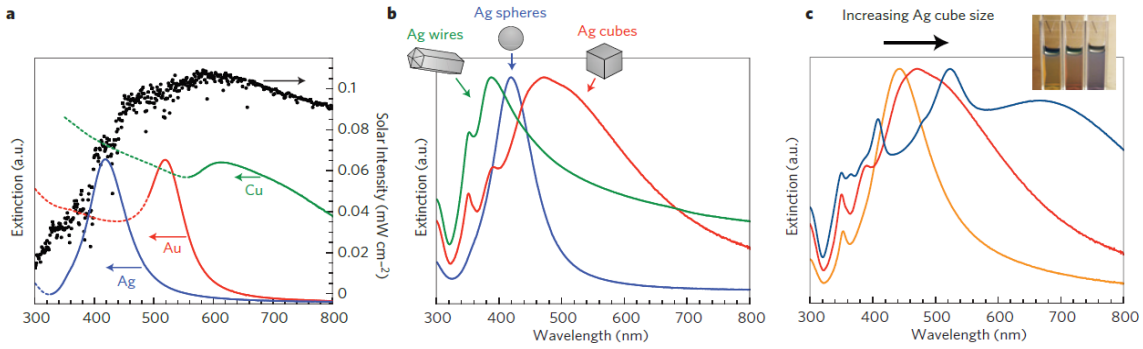

Figure 1.4. Extinction spectra demonstrating composition (a), shape (b), and size (c) dependence of LSPR wavelength from source[25].

The geometry of a nanostructure also influences the LSPR energy as demonstrated in **Figure 1.4b**. Increasing the complexity of the structure or increasing the number of vertices has an impact on the plasmon resonance[26]. Gonzalez and Noguez theoretically showed for Ag nanoparticles that as the truncation of a cubic particle increases, the LSPR blue shifts and the FWHM of the main resonance increases due to overlapping other resonances[27,28]. Additionally, nanoparticles with fewer faces display more resonances and the presence of corners causes the resonance to be over a wider energy range[28]. The theoretical work agrees well with the experimental work on silver nanocrystals by Tao et al[29]. The size of the nanostructure also impacts the LSPR energy. As demonstrated in **Figure 1.4c**, increasing the size causes the LSPR to red shift. This has been widely demonstrated in Ag cubes[4], Pd cubes[4], Ag bipyramids[30], Au cubes[30], Ag spheres[31], and Cu lithographically patterned nanoparticles[32].

1.3. Plasmonic Materials

The plasmonic response of a material is governed by its dielectric function and therefore each material has a unique response. Silver, gold, and copper nanostructures all sustain LSPRs in the IR region. Aluminum nanostructures may sustain LSPRs in the UV region. The complex dielectric function of each of these elements is shown in **Figure 1.5**. Here, we will discuss the plasmonic responses of Ag, Au, Cu, and Al and comment on their limitations.

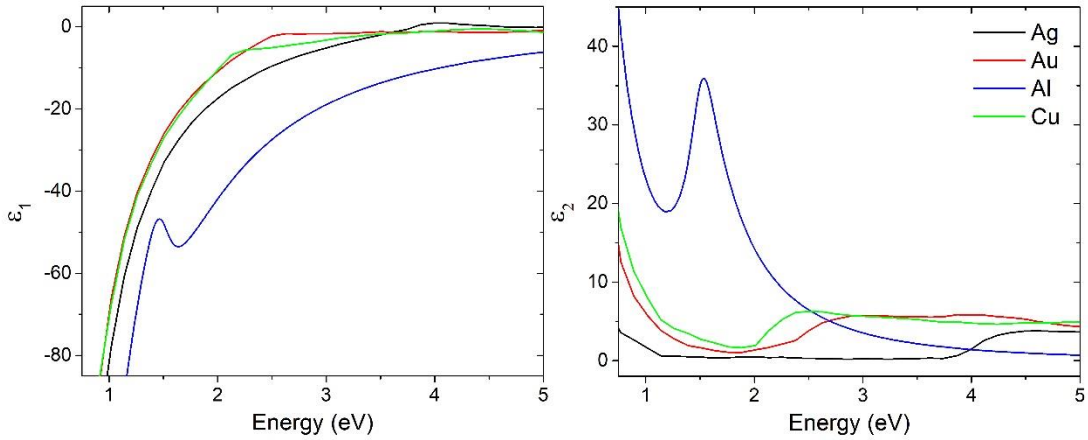

Figure 1.5. Real (a) and complex (b) parts of the dielectric function for Al[33], Cu, Au, and Ag from source[24].

Silver has long stood out as a material with superior plasmonic properties. It exhibits losses much lower than that of gold and also has strong field enhancement[34]. The LSPR is typically in the visible-nIR region. For example, 10 nm spheres in water exhibit a maximum in absorption at 390 nm due to the LSPR[35]. The dependence of size and shape for colloidal silver nanoparticles was studied for spheres, pentagons, and triangles in the range of 40 – 120 nm. They showed LSPR wavelengths spanning the visible wavelength region[36]. Unfortunately, Ag lacks chemical and thermal stability. Consequently, the effects of oxidation on the plasmonic response of Ag nanostructures needs to be understood. Han et al. observed significant decrease in surface enhanced Raman spectroscopy (SERS) enhancement factor in the presence of only a sub-monolayer of oxide coverage on Ag nanoparticles[37]. Although, Wang et al. showed the particles to be stable for 14 weeks after a dehydration process[34]. Silver nanoparticles find plasmonic applications in photothermal therapy[38], diagnostics[39], and light harvesting[40].

Gold has a strong plasmon resonance in the visible range and is physically and chemically stable making it an attractive plasmonic material[2]. For a 10 nm sphere, the absorption maximum occurs at 520 nm[35]. Au does have higher losses below 500 nm due to interband transitions[11]. Extensive work has been conducted to study gold nanoparticles which was

recently reviewed[2]. Gold has found plasmonic applications in sensing[41], cancer therapy[6], and other biomedical applications[42].

Copper is among the noble metals that exhibit promising plasmonic characteristics with a LSPR in the visible region, similar to Au and Ag. It is less expensive than Ag and Au, is a low-loss material, and has a high electrical conductivity[43]. Cu may find applications in waveguides[44] and power conversion[45]. Unfortunately, Cu suffers from surface oxidation and will form Cu_2O and CuO at room temperature which inhibit the plasmonic properties[11]. Although, oxide free Cu nanoparticles exhibit a sharp plasmon peak comparable to that of Ag and Au[32].

Aluminum has recently been of interest for plasmonics in the UV region. The bulk plasmon is located at 15 eV[46]. It has been shown that Al plasmons can be tuned within the UV-vis region by varying particle diameter[47]. Al is also attractive because it is abundant, cheap, and easy to incorporate into manufacturing processes via physical vapor deposition PVD techniques. Of course, Al is subject to oxidation but is passivated by a 3 nm thick native oxide. The presence of Al_2O_3 does decrease the plasmonic response by decreasing $\mathrm{Im}(\varepsilon)$ and increasing $\mathrm{Re}(\varepsilon)$[47]. Recently, arrays of Al nanostructures with a corrosion protection coating (polydopamine, a mussel-inspired polymer) exhibited an efficiency increase of 300% for photo-chemical conversion making it a viable option for light harvesting[48]. Al nanoparticles have also been used to enhance fluorescence in the UV region for biomolecule detection without labels[49].

Recently, there has been an effort to search for alternative plasmonic materials[11,16,50,51]. Alloying may be used to realize superior plasmonic properties than that of single elements. The main idea is to control the dielectric function of the material by varying composition. In doing so, the material can be tailored to exhibit a LSPR at a specific energy of interest. Alloying may also improve the stability of a material in regard to oxidation, corrosion, and temperature. Additionally, alloying may be employed to achieve materials with multifunctionality such as combining magnetic and plasmonic properties (magneto-plasmonics) or by using plasmonics to assist catalytic materials. Here, we present a summary of a few plasmonic alloy systems.

One obvious motivation for alloy plasmonics is improving the plasmonic response. While often times alloying reduces the plasmonic response, the response has been enhanced in a few cases. Gong and Leita investigated Au-Ag, Au-Cu, and Ag-Cu binary alloys and showed some alloy compositions minimized optical losses and exhibited enhanced SPP lengths[13]. Another study concluded that heterodimers with large Ag and small Au nanoparticles showed large enhancement of the plasmon peak and that by carefully selecting sizes, the sensor signal could be increased[3].

Another important consideration for plasmonics is the stability of the material. Alloys can also be employed to improve the stability of material. Au-Ag alloys have been shown to combine the chemical stability of Au and the superior Ag plasmonic properties[52]. In the Cu-Zn system, as little as 5% addition of Zn to Cu nanoparticles helped to stabilize them from oxidation[53].

Alloys can also be used to combine the plasmonic functionality of one element with a different functionality of another element. For example, magneto-plasmonic materials combine magnetic materials, such as Ni, Co, and Fe, that have low plasmonic responses with elements like Ag and Au whose plasmonic properties were discussed above. A detailed review of magneto-plasmonics was recently published[54]. In the case of Au-Co, the Co magnetic component is used to control the surface plasmon wave vector of Au which could be used for ultra-fast magneto-plasmonic switching[55]. Another combined functionality is plasmonic photocatalysts which employs a plasmonic material and a catalytic material[56]. Conventional photocatalytic materials are not efficient at light harvesting due to having a large bandgap. By adding a plasmonic nanostructure component to a photocatalytic material, the photocatalytic behavior is enhanced due to plasmon assisted increases in electron-hole separation rates[57]. Examples of these material systems include Au-TiO2 core-shell structures[58] and Ag/AgCl/TiO2 nanotubes[56].

Noble metal alloys are the most widely studied alloys for plasmonics. Gong and Leita recently experimentally determined the dielectric function (**Figure 1.6**) of Au-Ag, Au-Cu, and Ag-Cu binary alloys. Based on the calculated quality factor for surface plasmon polaritons for each composition, they showed that $Ag_{0.5}Au_{0.5}$, $Au_{0.1}Cu_{0.9}$, and $Cu_{0.1}Ag_{0.9}$ had higher Q-factors than that of the pure constituent metals in certain optical regions.

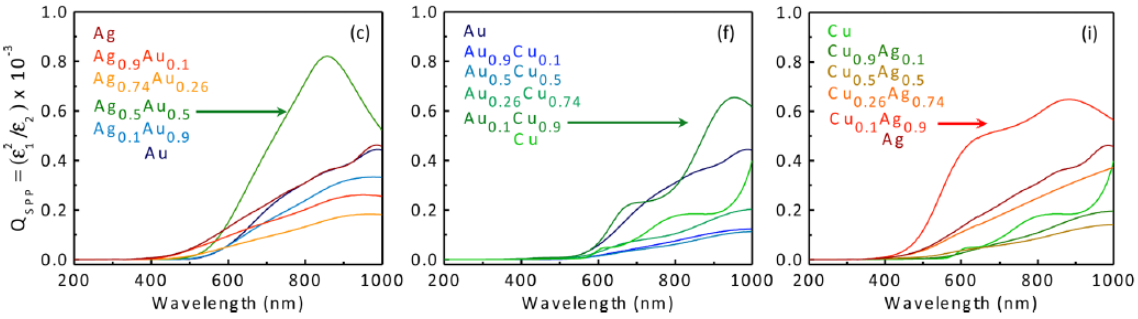

Figure 1.6. SPP quality factor for binary noble metal alloys[13].

Bansal et al. calculated the scattering efficiency and LSPR wavelength for Ag-Au nanoparticles using Mie theory. The LSPR can be tuned from 530 nm (pure Ag) to 610 (pure Au) for 50 nm radius particles in a silica environment. Based on the linewidth, scattering, and frequency range of the LSPR, they suggest that an alloy may be superior in solar cell applications[59]. Recently, Wu et al. examined truncated Au-Ag nanospheres with EELS and showed that all LSPR modes linearly red-shift with increasing Au concentration[60]. Scientists have also investigated Au-Ag-Cu ternary alloys and showed wide spectral range tunability of the plasmon resonance as well as electromagnetic field enhancement higher than that of pure Au[61].

1.4. Characterization

Experimentally, there are several ways to characterize the LSP of nanostructures. These techniques can be grouped into two categories: photon driven and electron driven.

1.4.1. Photon Driven Techniques

Common optical methods include transmission UV-vis spectroscopy and dark-field light scattering. Transmission UV-vis spectroscopy interrogates ensembles of nanostructures by measuring the extinction spectrum (scattering and absorption). For nontransparent samples, reflection spectroscopy can be used in which case the reflected light is collected and analyzed. Smaller ensembles and single nanostructures may be interrogated using dark-field light scattering where the light scattered by the nanostructures is analyzed.

Advantageously, this method avoids the strong background that reflection and transmission measurements contain, making it easier to detect weaker signals.

1.4.2. Electron Driven Techniques

The LSPR of individual nanoparticles may also be characterized through electron energy loss spectroscopy (EELS), specifically low-loss spectroscopy. In this case, electrons with a known energy interact with a sample. The electrons are then recollected, and their energy distribution analyzed[46]. Nanostructures may either be probed through the particle itself to observe the volume plasmon or by positioning the electron beam in an aloof position, next to the particle, to observe surface plasmons[62]. Additionally, spectrum imaging may be used for LSP mapping. In this case, an energy of interest may be selected, and the spectral intensity mapped as a function of position. The use of EELS for analyzing nanoparticle plasmons was recently reviewed[62]. **Figure 1.7** displays a representative EEL spectrum and spectrum images for a gold nanorod. Here, we see four distinct plasmon modes at 0.8 eV, 1.6 eV, 2.3 eV. Spectrum images enable the viewing of the near field distribution of the plasmon modes. From the spectrum images, the mode at 0.8 eV can be assigned as the bright dipolar or $m = 1$ mode because it has antinodes at each end of the rod. The mode at 1.6 eV can be assigned to the dark quadrupolar or $m = 2$ mode because it has three antinodes. In conventional optical techniques, dark modes are unable to be measured due to having no net dipole moment. Uniquely, the electron beam can probe both bright (odd ordered) and dark (even ordered) modes, providing a more comprehensive understanding of the structure's LSP modes[63].

Photon excitation and electron interrogation have been combined in the development of novel ways of understanding plasmons. Electron energy gain spectroscopy (EEGS) was first proposed as a new spectroscopy technique by Howie in 1999[64]. **Figure 1.8** demonstrates that when an electron in vacuum travels close to a surface, it can absorb the energy from a photon and be accelerated. This gain in energy will appear on the negative side of the zero loss peak in a traditional electron energy loss spectrum. Initial theories predicted EEGS to have an improved energy resolution due to the narrow linewidth of the external light source which could be brought into the sub-meV range[65].

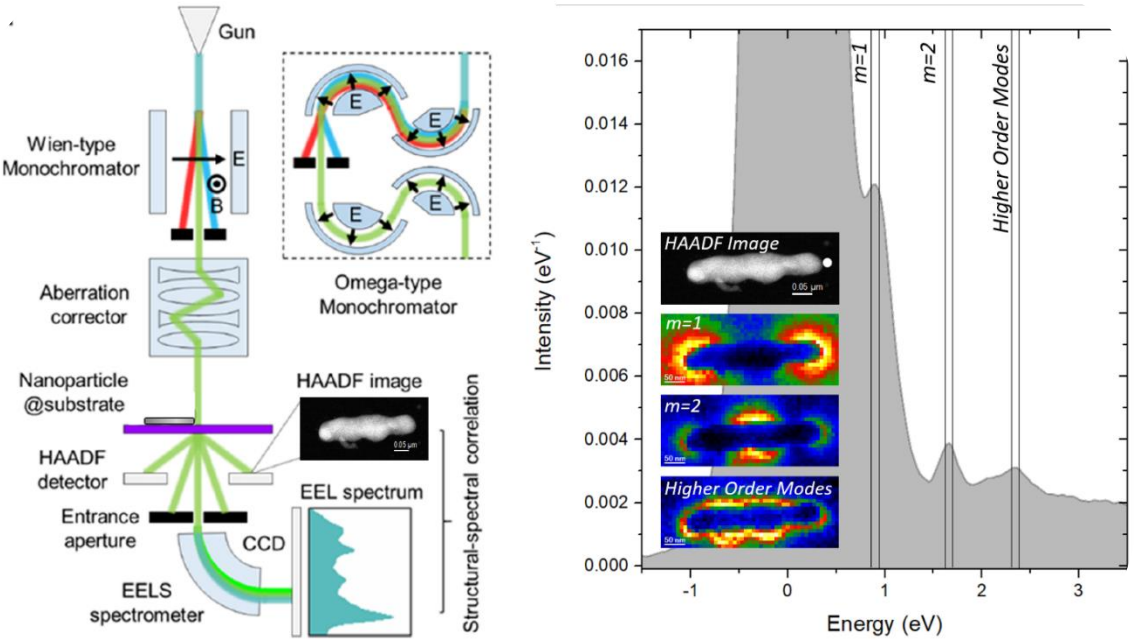

Figure 1.7. (a) Scanning transmission electron microscope (STEM) EEL spectrum acquisition schematic[62]. (b) EEL spectrum for the point marked in the HAADF image with corresponding EEL spectrum images for the $m = 1$, $m = 2$, and higher order plasmon modes.

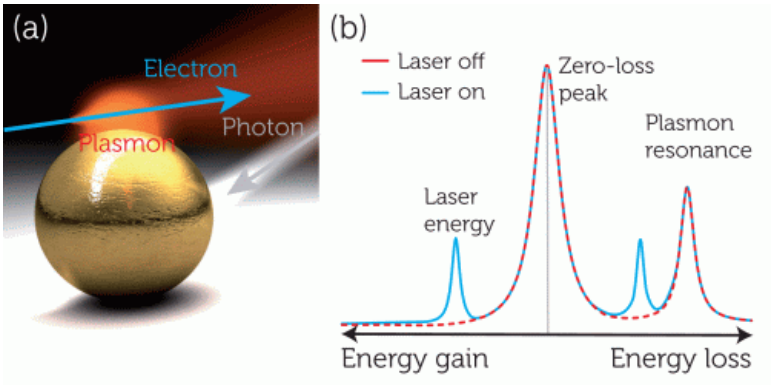

Figure 1.8. (a) Schematic showing an Au nanoparticle plasmon excited by a photon. The electron passes through the evanescent tail of tail of the plasmon. (b) EEL spectrum demonstrating the additional sEEG and sEEL peaks which appear when the laser is on.

However, it was later demonstrated that the resolution of EEG peaks is still limited by the resolution of the electron analyzer[66].

Along these lines, a few techniques have been developed to image the near field of optically excited nanostructures. The first of these is photoinduced near field electron microscopy (PINEM) in which electron beamlets or single electrons are photo-ejected from a cathode using a pulsed laser. A second laser pulse interacts directly with the sample and arrives at the sample coincident with the electrons. Photon stimulated EEG and EEL peaks emerge in the standard EEL spectrum upon appropriate irradiance. By adjusting the timing of the cathode and laser pulse, PINEM allows for temporal interrogation of structures[65,67,76–78,68–75]. An additional technique which utilizes a continuous current electron source and a nanosecond pulsed laser has been demonstrated to generate sEEL and sEEG signatures by appropriately gating the EEL spectrometer[79]. Lastly, it was demonstrated that a continuous current electron source and continuous wave laser could be used to produce the sEEG and sEEL signatures as well as image the near field distribution of optically stimulated plasmons[66].

Chapter 2

Combinatorial Thin Film Sputtering Au_xAl_{1-x} Alloys: Correlating Composition and Structure with Optical Properties

2.1. Preface

A version of this chapter was originally published by R. Collette et al.:

Collette, R.; Wu, Y.; Olafsson, A.; Camden, J. P.; Rack, P. D. Combinatorial Thin Film Sputtering Au_xAl_{1-x} Alloys: Correlating Composition and Structure with Optical Properties. *ACS Comb. Sci.* **2018**, *20*, 11, 633-642.

Robyn M. Collette and Yueying Wu conducted experiments reported in this manuscript. Robyn M. Collette analyzed the data. Agust Olafsson conducted SERS experiments and analysis. All co-authors discussed results.

2.2. Combinatorial Thin Film Sputtering Au_xAl_{1-x} Alloys: Correlating Composition and Structure with Optical Properties

2.2.1. Abstract

The Au-Al alloy system was investigated via a combinatorial thin film sputtering method for its potential as a plasmonic material. Au_xAl_{1-x} combinatorial libraries were co-sputtered from Au and Al elemental targets and the composition, phase, and dielectric function of an ~350 nm film was determined using energy dispersive spectroscopy (EDS), grazing incidence x-ray diffraction (GIXRD), and spectroscopic ellipsometry, respectively. The phase evolution and optical properties were analyzed after annealing various compositions under vacuum. The phases present matched the expected phases based on the published Al-Au binary phase diagram at all compositions. Interestingly, the mixed phase Al-$AuAl_2$ region showed the most optical tunability, where a maximum in the real part of the dielectric function progressively shifted to higher energy for increasing gold concentration. For almost pure $AuAl_2$, the imaginary component is largely reduced in the visible range and is comparable to that of pure Al in the UV region. A 20 nm thick film with composition $Au_{0.74}Al_{0.26}$ was studied using a (scanning) transmission electron microscope with an *in situ* laser heating system. The structure of the as deposited and laser annealed films were determined using selected area diffraction and the bulk plasmon of $AuAl_2$ and Al realized

with electron energy loss spectroscopy. Lastly, the Au-rich solid solution region was investigated as a surface enhanced raman spectroscopy (SERS) substrate using the benezenethiol (BT) molecule. Good SERS intensity was maintained up to 30% Al addition where enhancements of 10^5-10^7 were still observed.

2.2.2. Introduction

Rapid synthesis of thin film material libraries is critical for developing many solid state materials solutions. To this end, our group has employed a combinatorial thin film sputtering method to synthesize material libraries. The system is equipped with four individual sputtering sources with adjustable tilt, which can be used to adjust the compositional gradient of the combinatorial library. Our system has been exploited to explore various thin film materials ranging from catalytic [80,81], magnetic [82,83], optical [60,84–90], electrical [91], mechanical [82,92–94] and radiation hard materials [95,96]. Other groups have employed similar approaches to combinatorial thin films. Prominent groups have explored, for example, catalytic [97–100], bulk metallic glass [101], magnetic [102,103], optical [13,104,105], electrical [105–108], and mechanical [109] materials. Additionally, a few reviews on the subject have been published [110–113]. Mixed metallic alloys are an important means to tune the plasmon resonance or combine plasmonic properties with other functionalities [114], which may be superior to that of the individual elements. Using combinatorial approaches, Gong *et al* for instance, found that $Ag_{0.5}Au_{0.5}$, $Au_{0.1}Cu_{0.9}$, and $Cu_{0.1}Ag_{0.9}$ have lower optical losses and exhibited enhanced surface plasmon polariton lengths in certain optical regions relative to individual elements [13]. Au-Ag alloys have been shown to combine the stability of Au with the superior properties of Ag [52]. Others have shown that 5% Zn addition enhances the oxidation resistance of Cu [53]. Because of the vast composition space needed to be explored, combinatorial approaches can facilitate research into multicomponent alloys for advanced plasmonic applications. The dielectric properties of a number of alloy systems, such as Au-Ag [13,115], Ag-Cu [13,116], and Au-Cu [13], have been examined using optical spectroscopy and more recently the Au-Ag system by both ellipsometry and electron energy loss spectroscopy (EELS) [60]. The correlation of the dielectric properties with alloy composition not only reveals interesting physics but also facilitate the rationale design and synthesis of

alloy plasmonic nanostructures. Among various plasmon active alloys, the Au_xAl_{1-x} system is potentially interesting due to the fact that elemental Au [2] and Al [47] have strong plasmon resonances in the visible and ultraviolet (UV) region, respectively. Thus, the capability of tuning the plasmon resonance from the visible to the UV region via Au_xAl_{1-x} alloys for low loss plasmonic applications is intriguing. Indeed, the potential importance of $AuAl_2$ as a plasmonic material has been suggested both theoretically and experimentally [117,118]. Furthermore, the effect of Al additions on the optical properties of Au has been explored previously [119]. However, a systematic study of the complete Au_xAl_{1-x} system which correlates the phases present and optical properties is lacking.

In this study, we leverage a combinatorial thin film co-sputtering approach to rapidly synthesize an Au_xAl_{1-x} library [87]. Several critical points on the phase diagram are targeted and the phase evolution of the as-deposited and annealed films are correlated to the resultant dielectric functions. The alloy composition and phase structures are analyzed using energy dispersive x-ray spectroscopy (EDS) and grazing incidence x-ray diffraction (GIXRD), respectively. The dielectric constant as a function of energy is measured via spectroscopic ellipsometry. The phase evolution of the $Au_{0.26}Al_{0.74}$ composition is determined via *in situ* laser annealing in the transmission electron microscope and correlated to the low-loss electron energy loss spectroscopy correlate the plasmonic properties to the evolving microstructure. Finally, the Au-rich region of the phase diagram was tested as a SERS substrate for rhodamine-6G and benzenethiol molecules.

2.2.3. Experimental Procedures

2.2.3.1. Au-Al Alloy Thin Film Synthesis

Au_xAl_{1-x} alloy films ~ 350 nm thick were sputter deposited by RF magnetron sputtering onto 100 mm × 15 mm polished [100] silicon substrates or onto 5μm of thermally grown SiO_2. The alloys were deposited by co-sputtering pure Au and Al elemental targets, which were confocally directed toward the substrate as demonstrated in **Figure 2.1**. The substrates were positioned such that one end was closer to the Au target and the other closer to the Al target; thus, a composition gradient across the long axis of the sample was realized. The RF power supplied to each target is summarized in **Table 2.1** for each

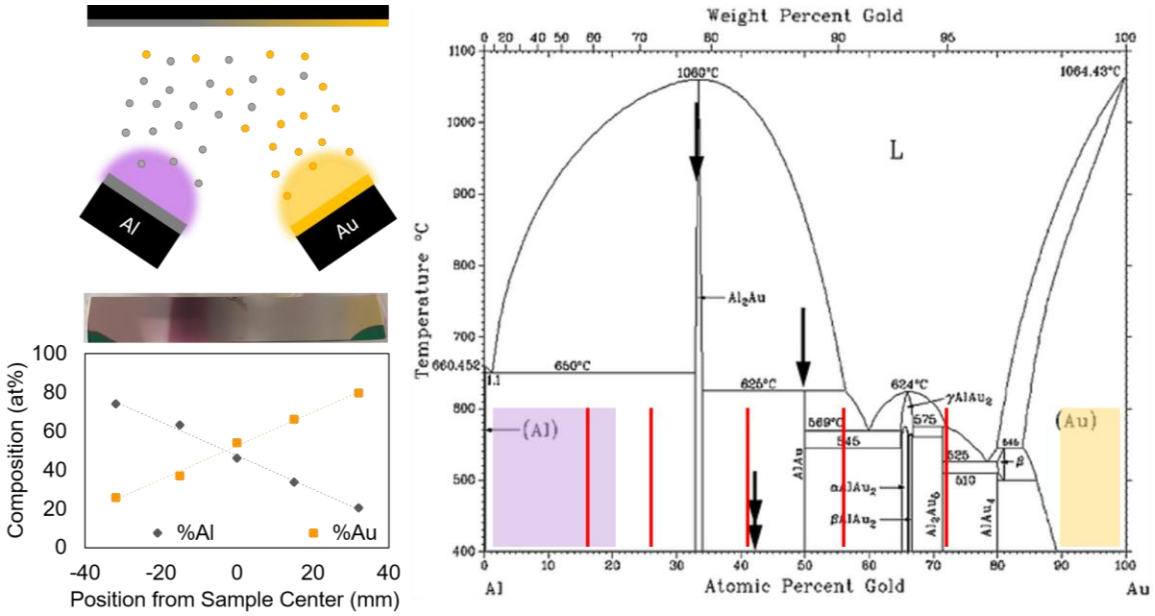

Figure 2.1. Schematic illustrating combinatorial sputtering arrangement to achieve a compositional gradient across a sample. Binary Au-Al phase diagram [120] with red lines corresponding to the initial compositions studied, and the subsequent regions that were studied highlighted in gold (corresponding to Au-rich solid solution region of the phase diagram) and purple (corresponding to the Al-AuAl2 mixed phase region).

Table 2.1. Au and Al Sputter Deposition Parameters

Composition	Target Power (W)		Deposition Time (hr:min)	Approximate Deposition Rate (nm/min)		Composition Gradient (Δx/mm)
	Al	Au		Al	Au	
Pure Au	0	40	1:40	0	3.3	-
Pure Al	200	0	1:40	3.5	0	-
0.15 < x < 0.72	100	20	1:40	2.0	1.5	0.006
0.9 < x < 1.0	30	40	1:27	1.1	3.3	0.001
0 < x < 0.2	200	10	1:20	3.5	0.25	0.002

gradient of interest. Several samples of each composition gradient were deposited as various annealing conditions were explored to correlate the phase evolution to the observed optical properties. For the $0.15 < x < 0.72$ composition gradient, the samples were subsequently annealed under vacuum for 30 minutes at 100 °C, 300 °C, and 500 °C and for the $0 < x < 0.2$ and $0.9 < x < 1$ composition gradients as-deposited and 500 °C annealed samples were investigated.

2.2.3.2. Composition measurement by EDS

The chemical composition of the film was measured at several locations along the sample for each gradient variety using a scanning electron microscope (Zeiss Evo) equipped with an energy dispersive x-ray spectroscopy detector (Bruker XFlash 6130). The spot size was around 1µm x 1µm. The accelerating voltage was set to 10 keV to record the spectra which allowed for observation of Al (Kα 1.486 keV) [121] and Au (Mα 2.123 keV) [121] peaks for quantification. The recorded compositions were plotted as a function of sample position and used for determining spot locations in subsequent measurements. The change in composition per mm for each sample is reported in **Table 2.1**. All subsequent measurements have a sufficiently small spot size such that the composition within the spot is approximately constant.

2.2.3.3. Phase Region Analysis

Grazing incidence x-ray diffraction (Panalytical X'Pert3 MRD) was used to measure the crystallographic structure of the films within a 4 mm × 9 mm region. Note that the composition on the sample was non-uniform along the 4 mm direction but was uniform in the 9 mm direction. The density of the film was approximated as an average of that of Au and Al and used to calculate the approximate penetration depth of the incident x-ray beam as a function of angle. The incidence angle for measurement was chosen to be 1.2° with an approximate penetration depth of 400 nm thus allowing the measurement to probe the film only and to prevent substrate effects. The diffracted beam intensity was recorded over 20° to 60°, a range which contained the main peaks for all Au-Al alloy compositions we would expect. Peaks were analyzed using Panalytical HighScore Plus software.

2.2.3.4. Determination of dielectric function of alloyed films

The dielectric function was measured using a J.A. Woolam M-2000U variable-angle spectroscopic ellipsometer over wavelengths between 245 and 999 nm with a spot size of 4mm × 8mm. The dielectric function of an alloy film was calculated from the ellipsometrically measured Ψ (Psi) and Δ (Delta), which is a measurement of the change in polarization of incident beam when it interacts with the alloy film, Because the alloy films are all optically thick and smooth, R(ε) and Im(ε) were obtained by point-by-point fitting of the calculated data. No dispersion model was used to fit the result, considering there is no existing model suit perfectly for the polycrystalline alloy films in our case due to complex phase structure, crystalline size, and energy band composition in each alloy. The measurement was performed at a fixed angle (65°) after preliminary test measurements were done at different angles and yielded consistent results.

2.2.3.5. TEM and EELS Experiment

$Au_{0.26}Al_{0.74}$ was sputtered to a thickness of ~20 nm onto a 20 nm thick SiO2 TEM membrane. monochromated Carl Zeiss LIBRA 200MC (S)TEM with an operating voltage of 200 kV. TEM images were taken at 31.5 kX. A 20 μm aperture was used for the as deposited SAED and a 5 μm aperture for the annealed area. SAED images were radially averaged using a rotational averaging [122] within Gatan Digital Micrograph™. The STEM images were performed with a convergence semiangle of 10 mrad, and a collection semiangle of 15 mrad. The low loss spectra were collected with a slit of 0.5 μm, and a dispersion of 29 meV per channel. The measured energy resolution (defined as the full width at half-maximum of the zero-loss peak) is 180 meV with the electron beam penetrating the SiO_2 substrate only. For the spectrum image in **Figure 2.9**, a ROI was chosen as 6 × 16 pixel spectra (1 pixel ∼10 nm × 10 nm) for c, 18 × 22 pixel spectra (1 pixel ∼10 nm × 10 nm) for top panel in g, and 7 × 27 pixel spectra (1 pixel ∼10 nm × 10 nm) for middle and bottom panel in g. The bulk plasmon maps in **Figure 2.9 c** and **g** were obtained by plotting spectra intensity in designated energy slices. The point EEL spectra in **Figure 2.9h** were normalized to zero-loss peak (ZLP) and the background spectrum was subtracted.

2.2.3.6. SERS Sample Preparation and Measurement

Si [100] wafers were cut into 5 mm × 5 mm size pieces. The unpolished backside of Si [100] 5 mm × 5 mm wafers were irradiated using a KrF excimer laser (248 nm, 18 ns) with an energy density of 2 J/cm^2 to create a textured surface. Au_xAl_{1-x} (x= 0.76, 0.81, 0.88, 0.96) films were sputtered to a thickness of 200 nm on the surface using the combinatorial sputtering system described above. A lab-built Raman spectrometer (HeNe 633 nm, Thorlabs) was used to collect spectra under ambient conditions. The beam was focused onto the sample (typical power 65 μW) using an inverted microscope objective (Nikon 20x, NA=0.5). Scattered light was collected in the same objective, passed through a Rayleigh rejection filter (Semrock), and dispersed in a spectrometer (PI Acton Research, f=0.3 m, 1200 grooves per mm). Light is detected by a back illuminated deep-depletion CCD (PIXIS, Spec-10, Princeton Instruments). Winspec 32 software (Princeton Instruments) operates the CCD and spectrometer. SERS spectra were collected in 5s acquisitions, for a total time of 60s at 3 regions of interest per Au_xAl_{1-x} substrate.

2.2.4. Results and Discussion

2.2.4.1. Investigation of compositions 0.15 < x < 0.72

Au_xAl_{1-x} alloys of compositions ranging from 0.15 < x < 0.72 were initially investigated, and the experimentally measured dielectric functions were correlated to the phase structures of as-deposited and annealed alloys at specific compositions. The compositions that were specifically examined were: x = 0.16, 0.26, 0.41, 0.56, and 0.72. The GIXRD of the as-deposited and 500°C-30 minute anneal patterns are shown in **Figure 2.2** and the phases identified at each sample composition are summarized in **Table 2.2** with the dominant phase in bold. The real and imaginary part of the dielectric function as a function of energy for each as-deposited and annealed composition is shown in **Figure 2.3**.

For the composition where x = 0.72, the equilibrium phase diagram suggests a mixture of Al_2Au_5 and $AlAu_4$ should be present. While many equilibrium phase diagrams suggest the composition Al_2Au_5, however it has since been shown that the Al_2Au_5 phase is actually Al_3Au_8 [123] although both continue to be used in literature. GIXRD suggests that the as-deposited samples contain primarily Al_3Au_8. However, upon annealing, $AuAl_4$ becomes

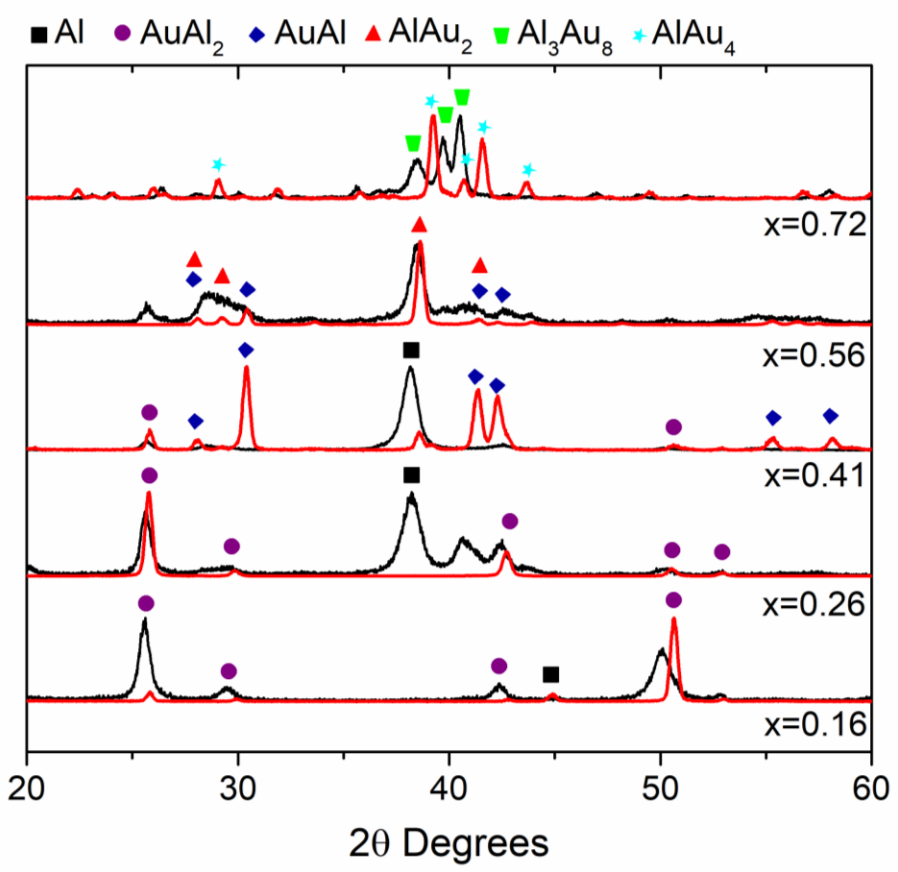

Figure 2.2. GIXRD results for Au_xAl_{1-x} film samples. As deposited samples shown in black while annealed samples are shown in red.

Table 2.2. Phases present in 0.15< x < 0.72 films determined by GIXRD with primary phases in bold print.

Anneal Condition	Distance from sample center (mm) and Chemical Composition				
	-32 $Au_{0.16}Al_{0.84}$	-15 $Au_{0.26}Al_{0.74}$	0 $Au_{0.41}Al_{0.59}$	15 $Au_{0.56}Al_{0.44}$	32 $Au_{0.72}Al_{0.28}$
As Deposited	Al, $AuAl_2$	Al, $AuAl_2$, AuAl	$AlAu_2$, $AuAl_2$, Al	$AlAu_2$, Al_3Au_8	Al_3Au_8
500 °C Anneal	Al, **$AuAl_2$**	**$AuAl_2$**	AuAl, $AlAu_2$	**$AlAu_2$**, Al_3Au_8	**$AlAu_4$**, Al_3Au_8

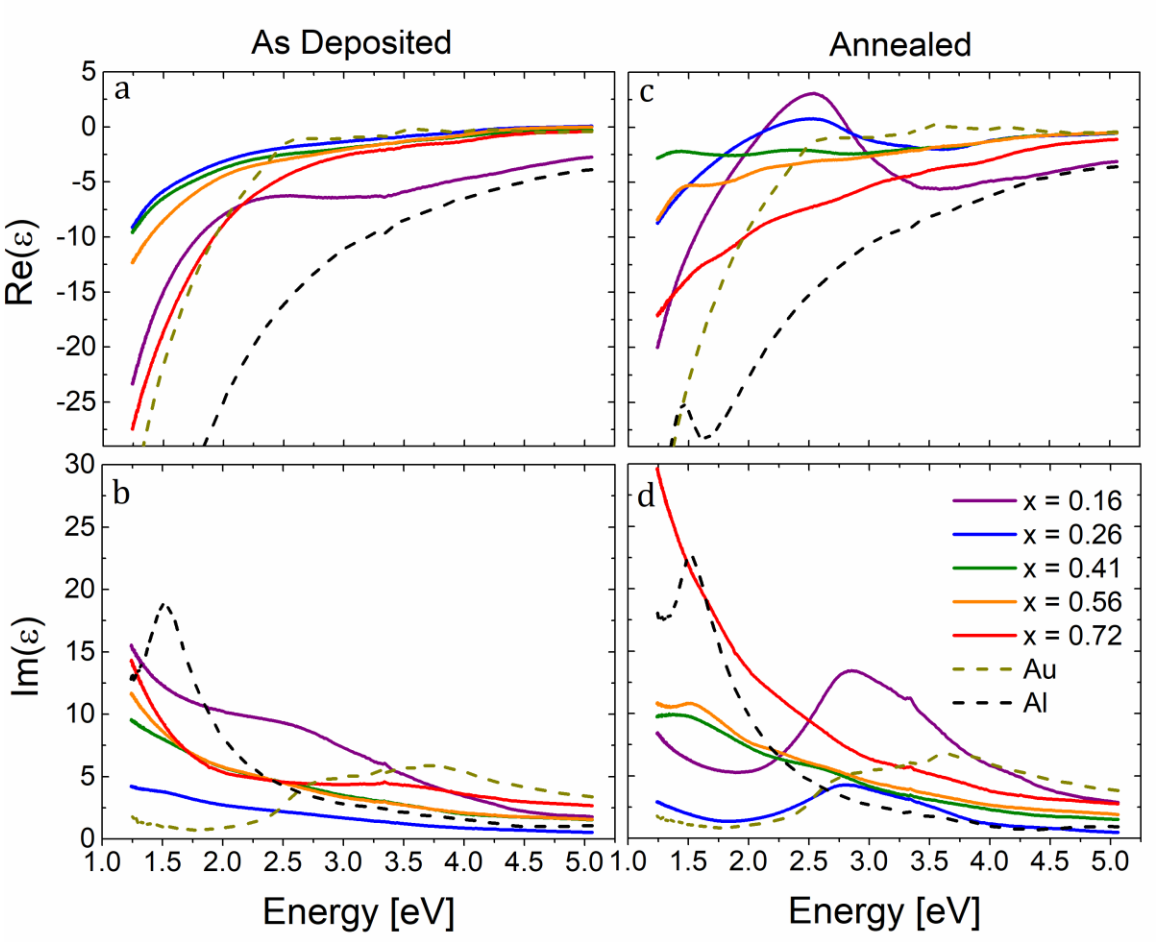

Figure 2.3. Dielectric function for Au_xAl_{1-x} film samples. Real (a) and imaginary (b) components of the dielectric function of the as deposited sample in the first column and the real (c) and imaginary (d) components for the annealed sample in the second column.

the dominant phase with some Al_3Au_8 reflections remaining. This agrees well with Manji et al. where they showed that Al_2Au_5 (really Al_3Au_8) is the first compound to form at the interface in bi-layer Au-Al films deposited and aged at room temperature [124,125].

At x = 0.56, we expect a mixture of AuAl and $AlAu_2$ and these are in fact the reflections observed in the as-deposited sample. Subsequent to annealing, the $AlAu_2$ emerges as the dominant phase. The Au_xAl_{1-x} phase diagram suggests a mixture of AuAl and $AuAl_2$ should be present at x = 0.41. The as-deposited sample has many phases that appear to be present with mainly low intensity reflections and one large pure Al reflection as indicated in **Table 2.2**. Upon annealing, the pure Al reflection disappears and AuAl and $AuAl_2$ are the only phases present.

At x = 0.26, we expect a mixed composition containing $AuAl_2$ and Al. The as-deposited sample contains Al, $AuAl_2$, and AuAl. Upon annealing, the $AuAl_2$ reflection dominates with a very weak reflection from Al. Al has a much lower x-ray atomic scattering factor than Au [126] and the change in intensity cannot be used to quantify relative phase amounts.

At x = 0.16, reflections from Al and $AuAl_2$ exist in both the as-deposited and annealed sample. After annealing, the reflections from $AuAl_2$ increase in intensity and sharpen. The Al reflection at 44.8 2θ also emerges upon annealing.

On the basis of the composition and phases summarized in **Table 2.2**, we examined how the dielectric constant (ε) varies as a function of the composition as well as the impact of the annealing treatment. In general, the real part (Re(ε)) becomes less negative and the imaginary part (Im(ε)) decreases for < 2.6 eV and increases >2.6 eV as the atomic fraction of Au increases. However, unlike a uniform binary solid solution system such as Au-Ag [115], the dielectric response of Au_xAl_{1-x} alloys is affected by its intermetallic compound formation and the fraction of each composition; thus, the dielectric constant does not simply continuously change as a function of composition. The Au_xAl_{1-x} system is composed of multiple intermetallic compounds, and the Drude model is not valid to describe interband transition effects. Despite the complexity, the results show interesting trends. Upon annealing, the crystallization and compound formation leads to a reduced Re(ε) in the low energy regime as observed in all samples. For the x = 0.41, 0.56, and 0.72 compositions, annealing also leads to an increase in Im(ε) indicating a higher loss in these

compounds. Interestingly, for x = 0.16 and x = 0.26, the Im(ε) in the visible range is largely reduced upon annealing, which may be suitable for plasmonic applications with low damping. For x = 0.26 (primarily $AuAl_2$), the measured Im(ε) in the UV region is comparable to pure Al and lower than pure Au, while for x = 0.16, Im(ε) is generally higher than that of the x = 0.26 sample, which may be due to the coexistence of multiple phases. Furthermore, for x = 0.16 and 0.26, where $AuAl_2$ is one of the dominant phases, a peak around 2.7 eV due to the interband transition becomes prominent in the annealed sample, which is consistent with previous studies of $AuAl_2$ [127,128]. The stronger interband transition peak in annealed samples is associated with an enhanced crystallinity as observed in GIXRD result, and a likely decrease in the vacancy concentration upon annealing [128]. In as-deposited films, crystal defects, phase boundaries, and vacancies introduce additional energy states around the Fermi level and induce a more complex band structure. Transitions between defect states can shift interband transitions and modify ε_2 compared to annealed films. Therefore, a decrease of these defect states may appear as a well-defined stronger interband transition peak in annealed alloy films. However more correlated experiments and alloy band structure calculations will be performed in our future studies to further understand the underlying mechanisms. As also suggested in earlier studies, the point in which the Re(ε) crosses zero for x = 0.16 and x = 0.26 samples is at ~2 eV, which indicates a bulk plasmon located in the visible region mediated by interband transitions in the $AuAl_2$ phase [127].

2.2.4.2. Solid Solution of Al in Au (0.90 < x < 1.00)

The solid solution region where x > 0.90 was investigated in more detail by co-sputtering a gold rich sample. Specifically, the compositions that are investigated include: x = 0.90, 0.93, 0.96, and 0.99. The GIXRD patterns for this region are shown in **Figure 2.4** and the dielectric functions are presented in **Figure 2.5**. For each composition for $x \geq 0.90$, the primary phase is the Au_xAl_{1-x} solid solution in the as deposited sample. In the x = 0.90 and x = 0.93 compositions, the $AuAl_4$ phase precipitates during the anneal as observed in the XRD pattern (see **Figure A.2.1**). As x increases towards pure Au, the Au reflection positions shift to higher 2θ, approaching that of pure Au, as noted in the inset of **Figure 2.4**.

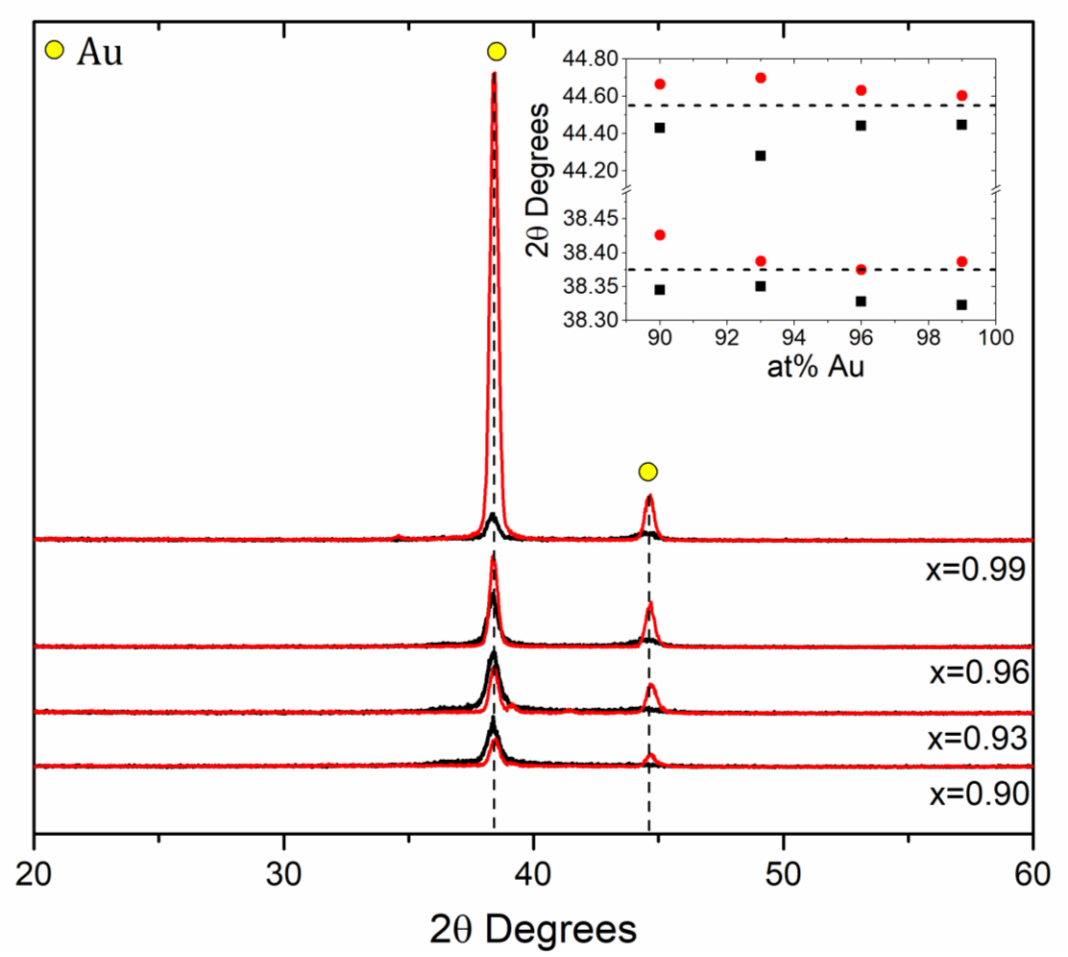

Figure 2.4. GIXRD results for the solid solution of Al in Au. As deposited samples shown in black and annealed samples are shown in red. Inset shows change in peak position (2θ) as a function of %Au with pure Au peak centers shown by dashed black line.

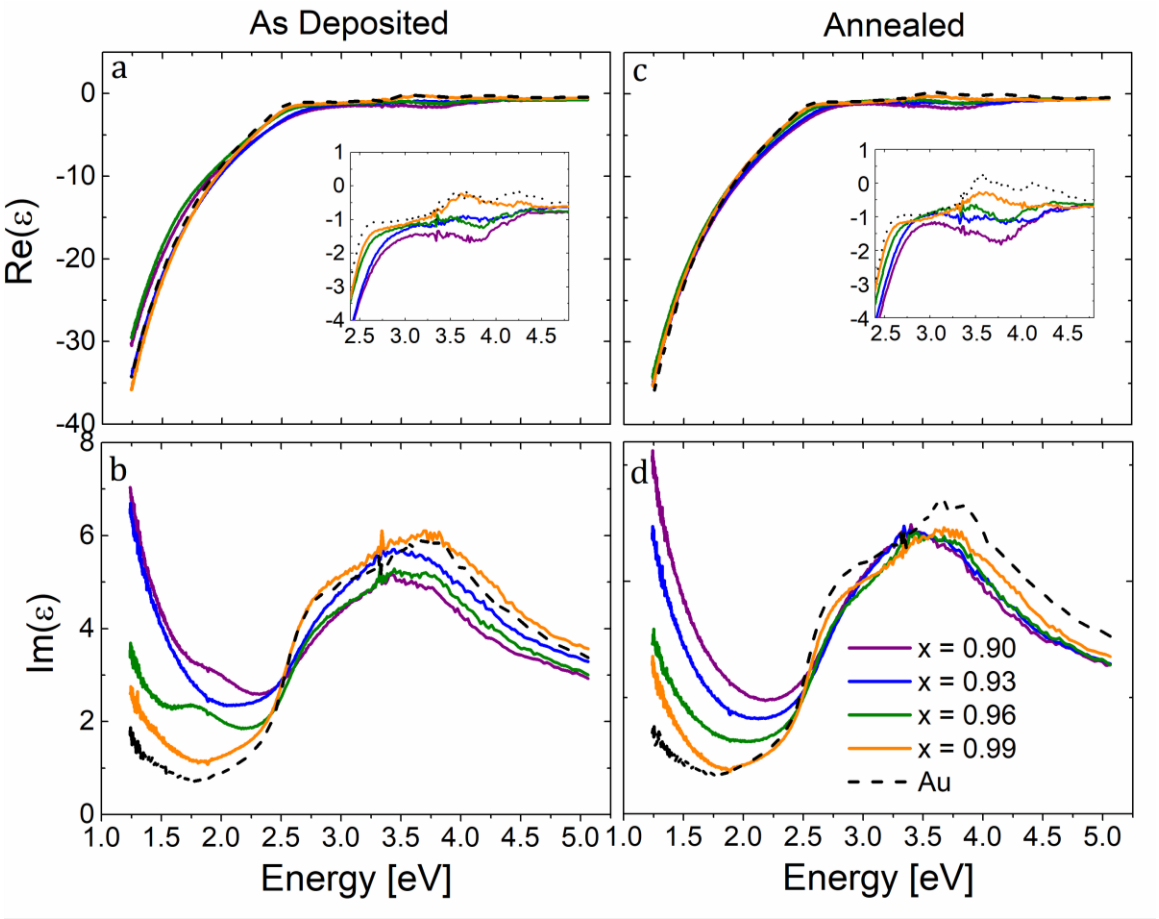

Figure 2.5. Dielectric function for solid solution of Al in Au. Real (a) and imaginary (b) components of the dielectric function of the as deposited sample in the first column and the real (c) and imaginary (d) components for the annealed sample in the second column (note the inset in the real dielectric constant is a magnified view of the region for 2.4 - 4.8 eV).

Additionally, we observe a shift in peak position to larger 2θ for the annealed samples, which may be attributed to a reduction in compressive film stress. As expected, these solid solutions show an onset of the interband transition at almost the same energy as observed in pure Au. Furthermore, the imaginary dielectric function increases as the amount of Al increases, which may be attributed to defects induced by the substitutional Al atoms. These results agree well with a previous study of this region of the Au_xAl_{1-x} phase diagram [119].

2.2.4.3. Al – $AuAl_2$ Mixed Phase (x < 0.20)

In this region of the phase diagram, a mixture of Al and $AuAl_2$ is expected. The GIXRD data for this region are presented in **Figure 2.6** and the dielectric functions in **Figure 2.7**. The compositions investigated were x= 0.01, 0.05, 0.08, 0.13, and 0.20, which correspond to approximate relative $AuAl_2$ phase amounts of 4%, 14%, 24%, 41%, and 60% $AuAl_2$. Reflections from both $AuAl_2$ and pure Al are observed in the GIXRD patterns. SEM images reveal a film texture in the annealed samples as shown in **Figure 2.8a**. EDS inspection in **Figure 2.8b**, suggests the texture is phase contrasted with brighter regions belonging to the $AuAl_2$ phase and darker regions to pure Al. SEM images of the associated as deposited films (see **Figure A.2.2**) do not have any contrast, suggestive of nanogranular morphology and likely supersaturated in each phase. This apparent phase contrast in the SEM is attributed to the grain growth/coalescence upon annealing the sample, which is also observed by the peak sharpening in the GIXRD patterns. At higher Au concentrations, there is an increase in the area of the lighter phase, consistent with an increase in the $AuAl_2$ phase.

Due to the coexistence of the Al and $AuAl_2$ phases upon annealing, the resultant dielectric functions show features from both phases. For x = 0.01 where almost pure Al exists, ε behaves very similar to pure Al. With the increase of the $AuAl_2$ phase, the Re(ε) peak shifts to a higher energy and the absolute value decreases until the values shift to positive at x = 0.20 as has been discussed above. In the Im(ε) part, one obvious observation is the red shift of the onset of the interband transition when the Al phase increases and may be due to an increased number of defect states in the $AuAl_2$ phase. Additionally, the onset of a second peak located at around 1.6 eV becomes obvious for the three compositions with more Al

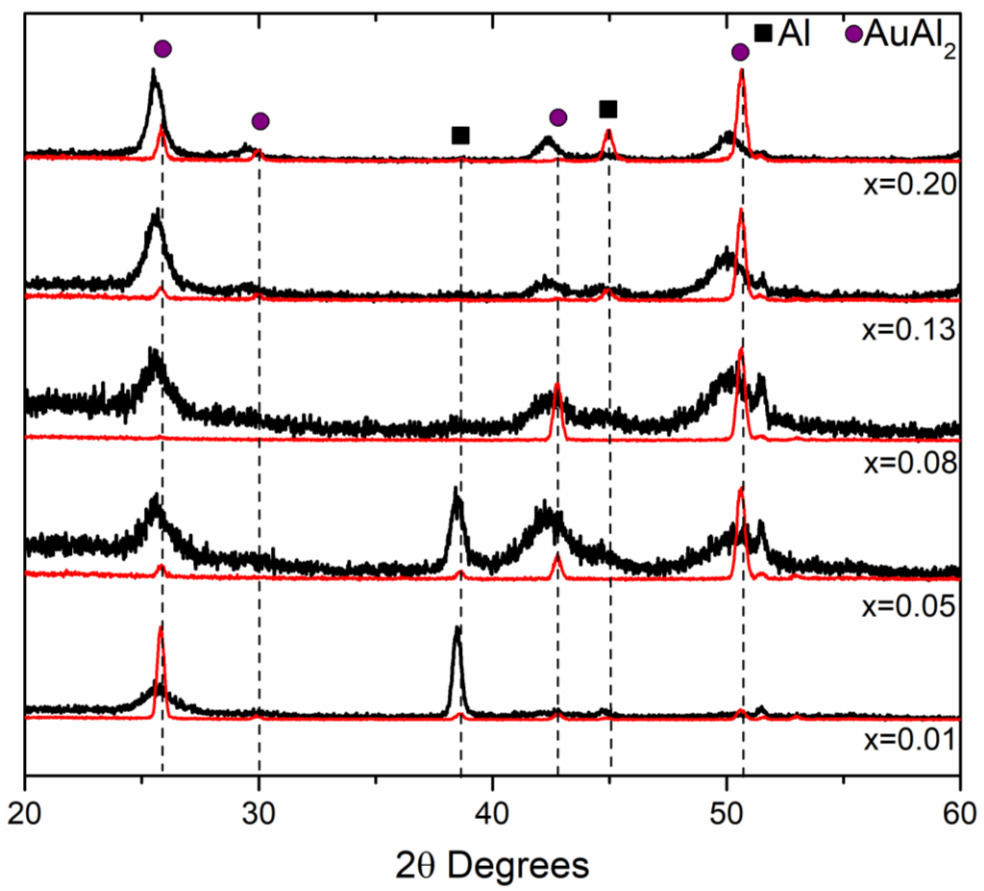

Figure 2.6. GIXRD data for mixed phase region Al-$AuAl_2$. As deposited samples shown in black while annealed samples are shown in red.

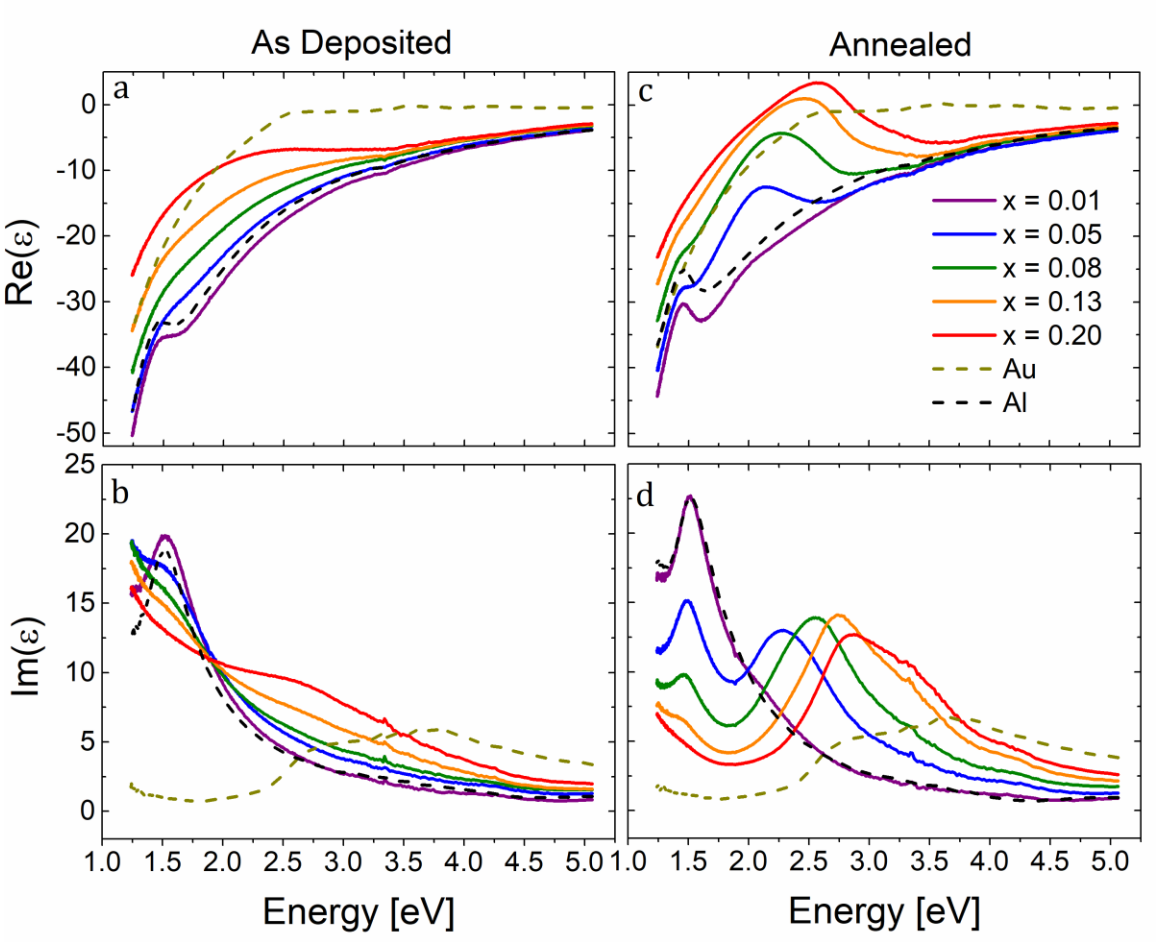

Figure 2.7. Dielectric function for the mixed phase region of Al-$AuAl_2$. Real (a) and imaginary (b) components of the dielectric function of the as deposited sample in the first column and the real (c) and imaginary (d) components for the annealed sample in the second column.

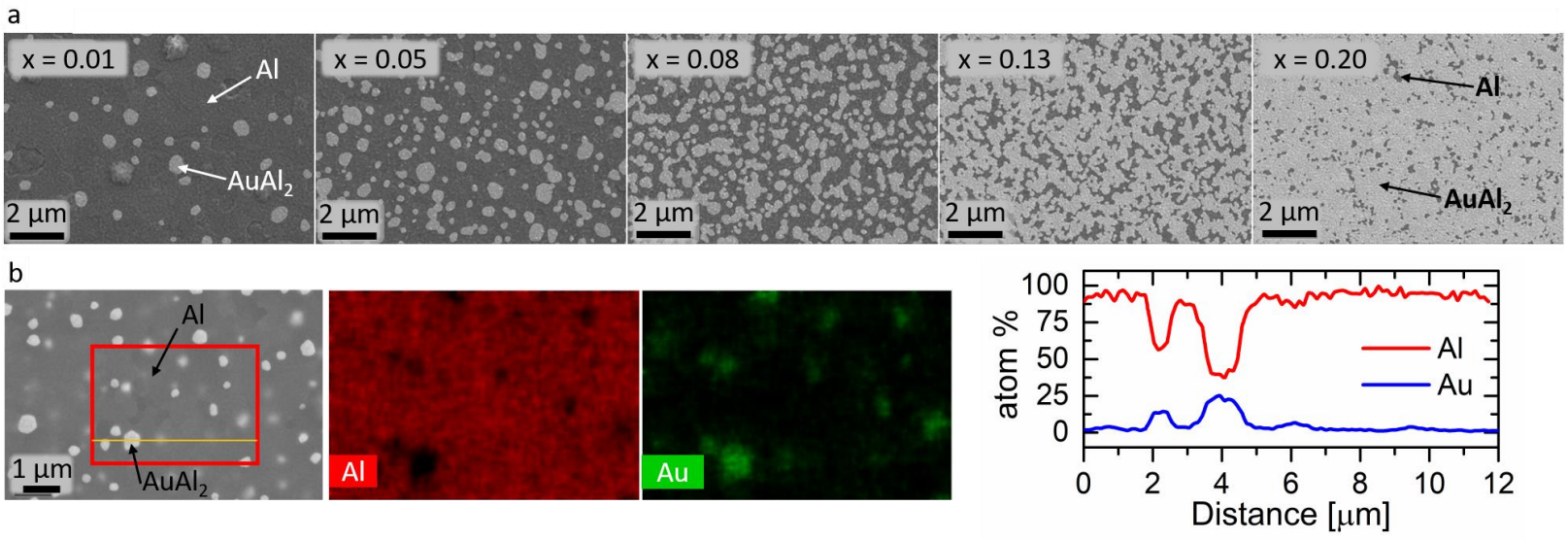

Figure 2.8. (a) SEM images for each composition studied all taken at same magnification with scale bars corresponding to 2 µm. (b) SEM image and EDS mapping of a region where x=0.01. Indicates phase contrast: bright spots are $AuAl_2$ and dark gray regions are Al (for example, labeled with arrows in x = 0.01 and 0.20). Red box corresponds to mapped area and orange line corresponds to the line scan.

($x < 0.13$). This feature is in good agreement with the reported interband transition in Al [129]. The appearance of two interband transition features in both the real and imaginary part of the dielectric constant again reveals the coexistence of both phases.

The $Au_{0.26}Al_{0.74}$ composition was further investigated by sputtering a 20 nm film on a SiO_2 TEM membrane. The bulk plasmon peak in the EELS spectra can be used to distinguish between the $AuAl_2$ phase and the Al phase. $AuAl_2$ has a bulk plasmon at ~2 eV [127] and Al at ~15 eV [46]. The as-deposited bright field TEM and high angle annular dark field (HAADF) images are shown in **Figure 2.9a** and **b**, respectively, and the film is polycrystalline as revealed by the selected area electron diffraction (SAED) pattern inset in the TEM image. As expected, the radially averaged and normalized SAED (**Figure 2.9d**) contains reflections from both Al and $AuAl_2$. The HAADF STEM image of the as deposited film which, similar to the SEM images of SI2, do not reveal much contrast. A representative EELS spectrum of this area is shown in **Figure 2.9h**, which features broad and low intensity peaks at 2 eV and 15 eV, confirming the presence of both phases with random distribution.

The sample was photothermally heated *in situ* with a 785 nm wavelength fiber coupled laser delivery system using 300 200-µs pulses at 67 mW. The laser delivery system is mounted on a 3-axis nanomanipulator system for easy focusing and convenient alignment to the electron/sample coincident point. Various laser powers (up to 200 mW), pulse widths (~ 2ns to continuous wave) and number of pulses as well as the Gaussian intensity profile (~ 5µm radius) can all be used to study various thermal heat treatments inside the TEM and is described in detail in Wu et al. [130]. **Figure 2.9e** and **f** are complementary bright field TEM (and SAED inset) and HAADF STEM images of the laser treated area just outside the laser center. **Figure 2.9g** are low loss EELS maps and **Figure 2.9h** are EELS spectra at various positions of the as-deposited and laser annealed film regions. At the edge of the laser spot zone, an Al rich region is formed, which is characterized by a sharp, intense low-loss EELS peak at 15 eV (**Figure 2.9h**) and illustrated in the 15 eV EELS map as bright yellow (**Figure 2.9g**). Further away from the laser center is an $AuAl_2$ rich region. The reflection corresponding to pure Al at 4.3 1/nm is greatly suppressed and

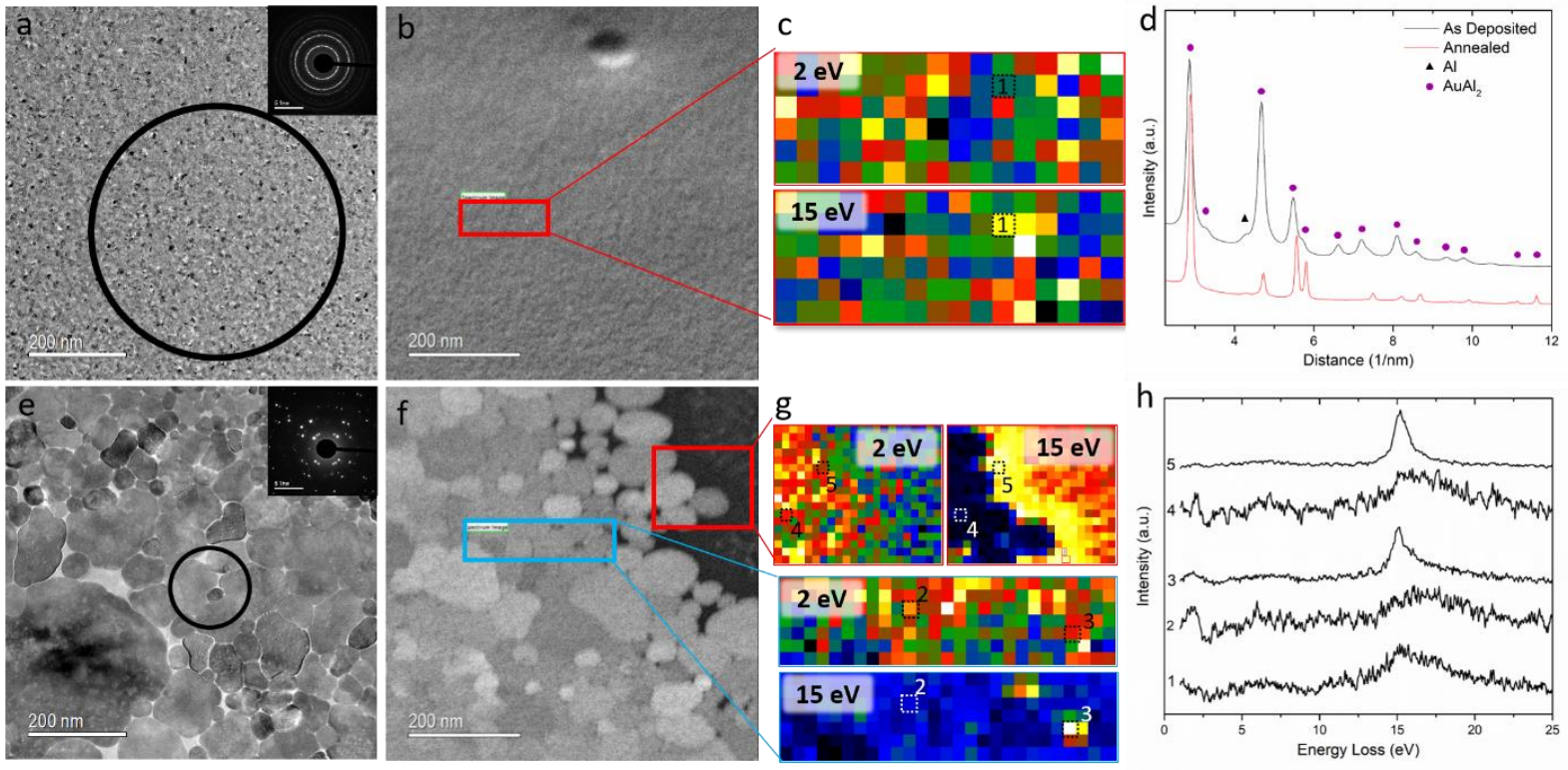

Figure 2.9. (a-b) As deposited TEM image and HAADF STEM image of the as deposited film with (c) corresponding EELS maps (2 and 15 eV). (d) Radially averaged and normalized selected area electron diffraction from (a) and (e) illustrating the presence of Al and $AuAl_2$ phases. (e-g) in-situ laser annealed TEM and HAADF STEM images, respectively and (g) corresponding EELS maps illustrating (2 and 15 eV). (h) Representative electron energy loss spectra of various positions noted in (c) and (g). The ~2 eV peak is attributed to $AuAl_2$ and the ~15 eV peak to Al.

the $AuAl_2$ reflections dominate. Enhanced crystallinity is also evidenced by sharper and fewer overall spots observed in the SAED pattern of **Figure 2.9e**. The EELS spectrum here features a peak at 2 eV and a broad, low intensity peak at 15 eV, which is consistent with the $AuAl_2$ phase.

2.2.4.4. Au-Al Alloys for SERS Substrates

Gold and aluminum structures have distinct localized surface plasmon resonances (LSPR) in the visible and UV regions [131–133], respectively, which have been taken advantage of for SERS substrates and analyses in recent years [134,135]. Additionally, there has been interest in designing gold alloys [136–140] and aluminum alloys [141,142] as SERS substrates. However, the efficacy of gold-aluminum alloys, which support LSPRs that differ from their pure metal characteristics, have not yet been studied. The SERS spectra in **Figure 2.10** were recorded using the co-sputtered Au_xAl_{1-x} alloys. Specifically, nanostrucutred Si surfaces with features in the micron size regime were coated with 200 nm Au_xAl_{1-x} (x = 0.76, 0.81, 0.88, 0.96) films, creating plasmonically active local sites. **Figure 2.10** shows SEM images of the coated silicon substrates in plane-view and tilted view, respectively. The efficacy of these plasmonic substrates for SERS based analyses was then tested through the use of the common SERS reporter molecule benezenethiol (BT). The SERS peaks at 999 cm^{-1}, 1022 cm^{-1}, 1068 cm^{-1}, 1570 cm^{-1} are in good agreement with previously reported spectra of BT [143], and remain distinguishable from the noise for all substrates with less than 30% Al. These data highlight the need for understanding how the SERS activity is influenced by LSPR shifts upon alloying and open a path for further analysis of how alloying affects molecular absorption on the SERS substrate, and how geometric features and Au_xAl_{1-x} film thickness affects SERS activity. Furthermore, our results can be used to extrapolate the enhancement factors expected for other commonly employed SERS substrates. A gold film over nanosphere (FON) substrate [144,145], for example, has an estimated 10^6-10^8 enhancement factor, suggesting that a FON substrate prepared from the alloys studied here could still yield enhancements of 10^5-10^7 for 30% Al composition based on the change in signal intensity shown in **Figure 2.10**.

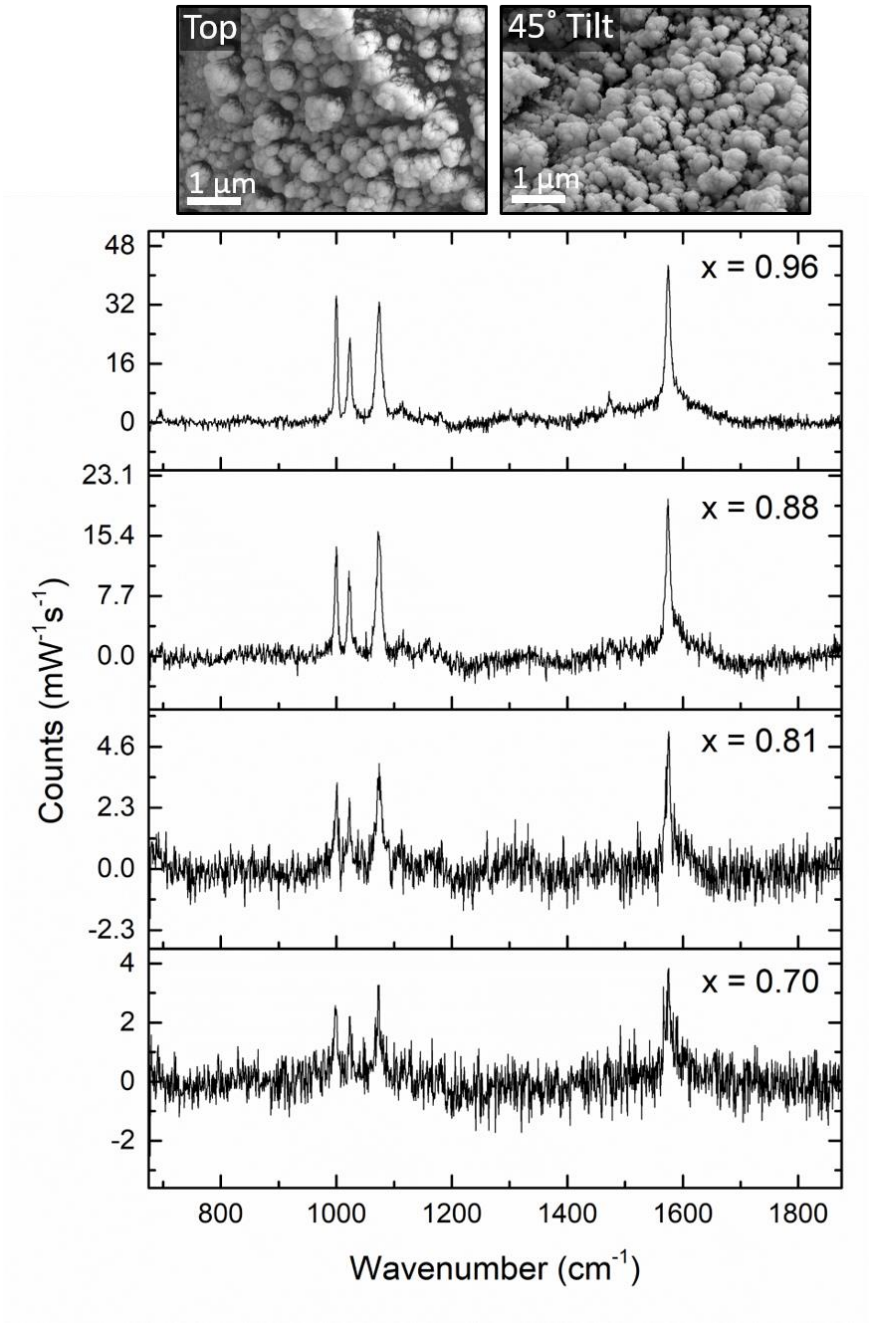

Figure 2.10. SERS signal for four Au-Al alloys on rough nanostructured Si surface. SEM images of nanostructured Si surface with 200 nm alloy film.

2.2.5. Conclusions

The structure and corresponding dielectric function for the Au_xAl_{1-x} system is studied in detail. Features in the dielectric function are correlated to phases observed in as deposited and annealed films. The phase evolution in the annealed films is also correlated to the measured optical properties. While in some compositions metastable phases were realized in the as deposited film, the annealed films all contained phases expected from the equilibrium phase diagram. The solid solution of Al in Au for $x > 0.9$ reveals an increase in the imaginary component of the dielectric function at low energy, but otherwise behaved similarly to pure Au. In the mixed phase region of Al and $AuAl_2$, the dielectric function can effectively be tuned by altering the relative amounts of Al and $AuAl_2$ in the sample. *In-situ* laser annealing of a 20 nm $Au_{0.26}Al_{0.74}$ film in the TEM revealed grain growth and coarsening of the initially nanogranular Al-AuAl2 film. The bulk plasmons of Al and $AuAl_2$ were observed with low-loss EELS as peaks at 15 eV and 2 eV respectively. The as deposited film has broad low-intensity low-loss EELS peaks relative to the larger grained annealed films. Finally, Au-Al alloys were explored as SERS substrates. In general, SERS substrates are affected by the morphology and dielectric environment [146,147], the latter of which was the focus of our work. By keeping the morphology the same for each substrate, we are able to observe the effect of changing dielectric properties due to alloying on the relative SERS signal. Good SERS intensity was observed up to 30% addition of Al to Au, from which we extrapolate an enhancement factor of 10^5-10^7 for FON substrates with these alloys. This is comparable to the 10^6-10^8 enhancement factor of gold FON substrates.

2.2.6. Appendix

2.2.6.1. Figures

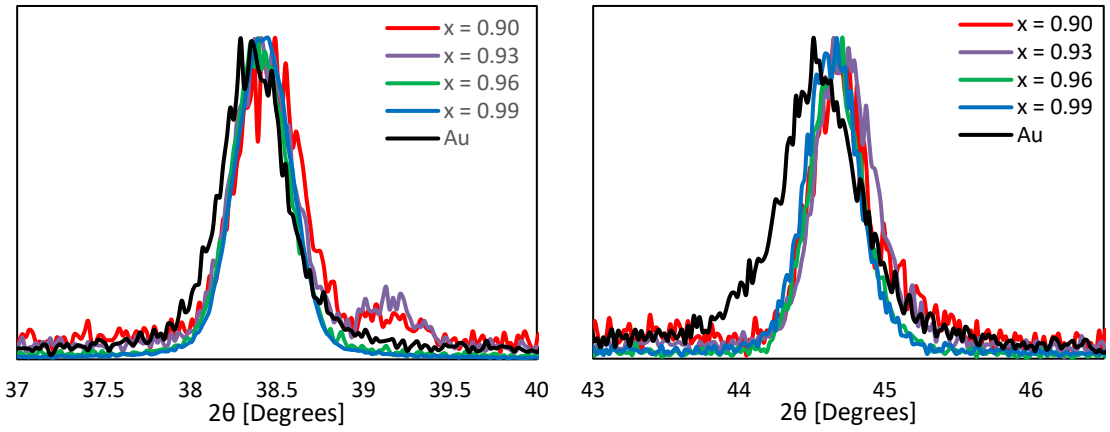

Figure A.2.1. Normalized GIXRD peaks for the annealed, Au rich sample discussed in section 2. Here we see a general trend of peaks shifting toward that of pure Au (lower 2θ) as the amount of Au in the sample increases.

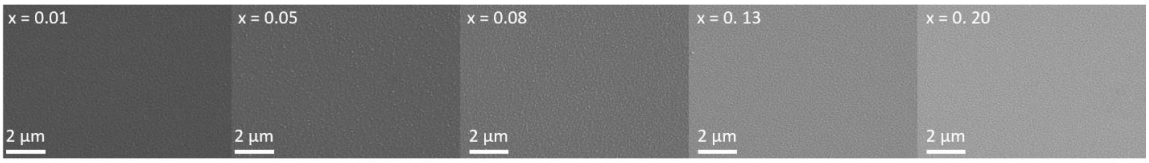

Figure A.2.2. As deposited Al-AuAl2 film. All images were taken at the same brightness and contrast values for sake of comparison. We see the color becomes lighter as the composition becomes more Au rich. There is slight texture in the images, but no phase contrast is observed.

Chapter 3

Correlating the Optical Property Evolution in the Au-Ni Binary Thin Films: From Metastable Solid Solution to Phase Separated Alloy

3.1. Preface

A version of this chapter was originally published by R. Collette et al.:

Collette, R.; Wu, Y.; Rack, P. D. Correlating the Optical Property Evolution in the Au-Ni Binary Thin Films: From Metastable Solid Solution to Phase Separated Alloy. *J. Alloy Compd.* **2019**, *793*, 695-704**.**

Robyn Collette conducted experiments and data analysis in this manuscript. Robyn developed the analytical dielectric function model in the manuscript. All co-authors discussed results.

3.2. Correlating the Optical Property Evolution in the Au-Ni Binary Thin Films: From Metastable Solid Solution to Phase Separated Alloy

3.2.1. Abstract

In this study, the optical properties of $Au_{1-x}Ni_x$ alloy thin films are investigated by employing a combinatorial sputtering approach. The dielectric function is measured using spectroscopic ellipsometry and is correlated to the composition, determined by energy dispersive spectroscopy, and phases present, determined via x-ray diffraction. As-deposited alloys form a metastable solid solution, however, annealed alloys exhibited phase separation into Au-rich and Ni-rich phases due to the large miscibility gap in the Au-Ni material system. The optical properties are then rationalized by modeling the dielectric function of the solid solution alloys with a Drude-Critical Point analytical model. Lastly, the efficacy of the model is demonstrated which shows that the dielectric function of the phase separated alloys can be approximated using a composition-weighted average of two solid solution dielectric functions.

3.2.2. Introduction

Metallic alloys provide a pathway to tune the plasmonic response of a material [114]. For instance, several Au alloys have been explored for plasmonic applications. Since Au is a noble metal, in some cases, alloying is explored to improve resistance to oxidation or corrosion while maintaining good plasmonic properties [118]. For example, Au-Cd alloys cause a shift in the in the imaginary dielectric constant to different energies than that of pure Au, which increases the losses in one energy range while decreasing losses at other energy regions [11]. Other applications explore alloying to add functionality. More specifically, creating alloys of noble-transition metal components may allow for combination of plasmonic properties from the noble metal and magnetic or catalytic properties from a transition metal [148]. Amendola et al. demonstrated the coexistence of both plasmonic and magnetic properties in $Au_{0.89}Fe_{0.11}$ alloys and suggested promise for applications in magnetic resonance imaging [149]. More recently, Amendola et al. studied Au-Fe nanoalloys with various compositions up to 13 at% Fe addition, demonstrating the surface plasmon resonance exists in this range of alloys albeit decreasing intensity with increasing Fe content [11]. Additionally, Cu-Co [150] and Ag-Co nanoparticles (plasmonic-magnetic, respectively) generated by a pulsed laser induced dewetting process have been studied where phase separated bi-metallic nanoparticles evolve from laser melted films; the resultant plasmonic [151] and so-called ferroplasmonic [152] properties have been studied via optical spectroscopy and electron energy loss spectroscopy. The coexistence of magnetic and plasmonic properties has also been shown in the $Au_{1-x}Ni_x$ alloy where $0.02 \leq x \leq 0.10$ [153].

Au and Ni both have a face-centered cubic (FCC) structure. However, Au has a larger lattice parameter (4.08 Å) [154] than Ni (3.52 Å) [155], which causes the alloy system to have limited solubility. The Au-Ni system contains a large miscibility gap in the solid phase region [156] where outside the miscibility gap, Au and Ni form a solid solution. At temperatures below the miscibility gap critical point, 816°C, Ni has higher solubility in Au while Au has very limited solubility in Ni. Within this miscibility gap, Au and Ni are expected to phase separate into compositions determined by the miscibility gap boundary.

For example, at 600°C the system is expected to phase separate into $Au_{0.78}Ni_{0.22}$ grains and $Au_{0.04}Ni_{0.96}$ grains. Consequently, dewetting of Au-Ni films has been studied where it has been demonstrated that alloying behavior plays a key role in the dewetting process [157].

Limited optical studies on the full Au-Ni alloy system have been conducted. Bassett et al. studied dilute $Au_{1-x}Ni_x$ alloys where $0.01 \leq x \leq 0.05$. They found that in general, increasing Ni impurities causes enhanced scattering in the energy region below the band edge and a reduced interband absorption above the band edge energy. This results in increased reflectance at lower energy (IR) and a decreased reflectance toward higher energy (UV) [158,159]. More recently, McPherson et al. demonstrated that the dielectric function of Au-Ni thin films can be tuned by changing the electronic configuration of the metastable solid solution, accomplished by varying the stoichiometry. They also demonstrated similar results by stacking Au and Ni films in varying layer numbers and thicknesses [159]. In these cases, only the Au-rich side of the Au-Ni alloy system has been investigated. However, to the best of our knowledge, no study of the dielectric function and annealing effects on the full Au-Ni system has been completed.

We systematically investigate the optical properties of thin film $Au_{1-x}Ni_x$ alloys across the entire phase diagram. The as-deposited material forms metastable solid solutions [159], which, depending on the composition, phase separate upon annealing consistent with the equilibrium phase diagram. The efficacy of the various alloy compositions as a plasmonic material is determined by measuring the dielectric function and calculating the corresponding LSPR quality factor ($-Re(\varepsilon)/Im(\varepsilon)$). Furthermore, the optical properties are correlated to the phases present as determined via x-ray diffraction (XRD). While the dielectric function logically changes in the $Au_{1-x}Ni_x$, the dielectric function of the solid solution behaves different than the phase-separated alloys. We rationalize these changes by implementing a Drude-critical point model with three critical points to model the dielectric function with changing composition. Finally, we demonstrate that the model can be applied to model the dielectric function of phase separated alloys by using a composition-weighted average.

There have been a several approaches to modeling the dielectric function of solid solution alloys, Au-Ag for instance [18,19], as it is well known that an effective medium approximation does not work for solid solutions that are mixed on the atomic scale [160]. For instance, a composition-weighted average model does not accurately predict the varying position of the extinction peak, which varies linearly with composition [161]. Others have tried to rationalize the changes by varying the threshold of interband transitions linearly but failed to take into account changes in the behavior of free electrons with varying composition [162]. The Drude-Lorentz model separates intra- and inter- band effects by using the Drude model to describe the free electron behavior and a certain number of Lorentzian functions to represent interband transitions. However, this model does not always reproduce the data well without adding an arbitrarily large number of Lorentzian terms [17]. A more recent approach that was introduced is the Drude-critical point model, where critical points in the band structure are represented with various functional forms. Etchegoin et al. replaced the Lorentzian terms with critical point terms, which accommodate asymmetric line shapes [17]. This model has realized success in representing the dielectric function of pure Au using only two critical point terms. Rioux et al used a Drude-critical point model, where the critical point contributions were based on modeling the joint density of states [18]. This model worked well due to the similarity of the Au and Ag band structures and the similar critical point types. Rodriguez compared modeling the dielectric function of Au-Ag alloys using the Drude-Lorentz model with five Lorentzian terms as well as the Drude-critical point model using two critical points [19]. By fitting the dielectric function of individual alloys, he showed that the parameters change with composition in a well-behaved manner. With a description of how the parameters change with composition, the model parameters can be calculated for any Au-Ag alloy composition and used to calculate the complex dielectric function.

It is necessary to have a model to describe the dielectric function behavior in order to accurately simulate, for example, the optical behavior of nanoparticles. For example, Messina et al. simulated the extinction spectra of nanoparticles using published dielectric function data for $Au_{0.85}Ni_{0.15}$ films and compared it to their experimental extinction spectra

of $Au_{0.9}Ni_{0.1}$ nanoparticles. They noted that the differences in the simulated and experimental data can be attributed to the difference in compositions [153]. Clearly, having a model to fully describe the system makes it possible to better represent the full composition space.

The Au-Ni system exhibits a dielectric function which changes smoothly with composition. However, a simple composition-weighted average of the pure metal dielectric functions does not reproduce the as-deposited alloy data. Similarly, the Drude-Lorentz model fails to reproduce our data with a reasonable number of Lorentz oscillators (1-5) since it does not accurately account for asymmetric line shapes which reflect more complex joint density of states. The critical point model used by Rioux does also not work well for the Au-Ni system because Au and Ni have dissimilar band structures where certain symmetry points exhibit different critical point characteristics where the transition from one to another is difficult to predict as a function of the $Au_{1-x}Ni_x$ composition. Etchegoin et al. used a Drude-critical point model with two critical points to model the dielectric function of pure Au. It had also been shown that the dielectric function of Ni was well represented using three interband terms [163]. We found this D-CP model, with an additional critical point, fits our data accurately. Thus we model the dielectric function of each solid solution using the Drude-critical point model to rationalize the optical property changes. We utilize three critical points and demonstrate a logical shift in parameters with composition, which effectively allows us to calculate the dielectric function of any Au-Ni solid solution. Using this model, it was then possible to approximate the dielectric function of the phase separated materials using a simple composition-weighted average based on volume fractions.

3.2.3. Experimental Procedures

3.2.3.1. Sample Preparation

$Au_{1-x}Ni_x$ films ~300 nm thick were deposited via RF magnetron sputtering onto three 20 mm × 100 mm substrates. The substrates were polished [100] silicon with 100 nm of thermally grown SiO_2. Alloys were formed by co-sputtering pure Au and Ni elemental targets, confocally directed towards the substrate [164]. The chamber was evacuated to below

1×10^{-6} Torr. Sputtering was carried out in an Ar atmosphere at 5 mTorr. Sputtering parameters are listed in **Table 3.1**. The sample was oriented to have one end above the Au target and the other above the Ni target, thus achieving a compositional gradient across the long axis of the sample with one end being Au-rich and the other being Ni-rich. One sample was analyzed in the as-deposited state, while two other samples were annealed under vacuum ($<1\times10^{-6}$ Torr) for one hour at 300ºC and 600ºC, respectively.

A second set of samples with a uniform composition of $Au_{0.35}Ni_{0.65}$ was-deposited onto seven 30 mm × 30 mm substrates. To achieve uniform composition, the substrate holder was rotated during deposition at 20 RPM. One sample measured in the as-deposited state while the remaining 6 were annealed at 150, 300, 450, 600, 725, and 775ºC, respectively. A third set of isocompositional $Au_{0.28}Ni_{0.72}$ samples was also prepared where one sample was left in the as-deposited state while the others were annealed at 300°C for 0.5, 1, 2, 3, 5, and 10 hours.

3.2.3.2. Composition Measurement and SEM Imaging

The film composition at each measurement location was determined using an energy dispersive spectrometer (Bruker) within a scanning electron microscope (Zeiss Merlin). Images were acquired using the in-lens detector at various magnifications. The accelerating voltage was set to 15 kV. Spectra were recorded in an approximately 5 µm x 5 µm area for 60 seconds. Quantification was performed using the Au Mα peak at 2.123 eV and the Ni Kα peak at 7.480 eV. It was determined that a roughly linear composition gradient of 0.0059 and 0.0077 Δx_{Ni} per mm was achieved (see **Figure 3.1** for details) for $x < 0.3$ and $0.3 < x < 0.9$ samples, respectively.

3.2.3.3. Phase Identification

X-ray diffraction and subsequently phase identification for the first set of samples was performed using grazing incidence x-ray diffraction within a 4 mm x 9 mm region, where the composition gradient is in the 4 mm axis and uniform in the 9 mm direction. Consequently, each measurement location has <0.0308 change in composition, x_{Ni}, within the measurement spot size. The incidence angle was set to 4º for these samples and the diffracted beam intensity was recorded from 35º to 55º, a range sufficient to observe the

Table 3.1. Au and Ni Sputter Deposition Parameters

Composition	Target Power (W)		Stage Rotation (RPM)	Deposition Time (hr:min)	Approximate Deposition Rate (nm/min)
	Au	Ni			
Pure Au	40	0	20	2:00	5.2
Pure Ni	0	110	20	2:00	2.8
$0 < x < 0.3$	40	70	0	0:58	7.7
$0.3 < x < 0.9$	20	110	0	1:30	5.0
$Au_{0.35}Ni_{0.65}$	20	100	20	1:15	5.0
$Au_{0.28}Ni_{0.72}$	20	100	20	1:15	5.0

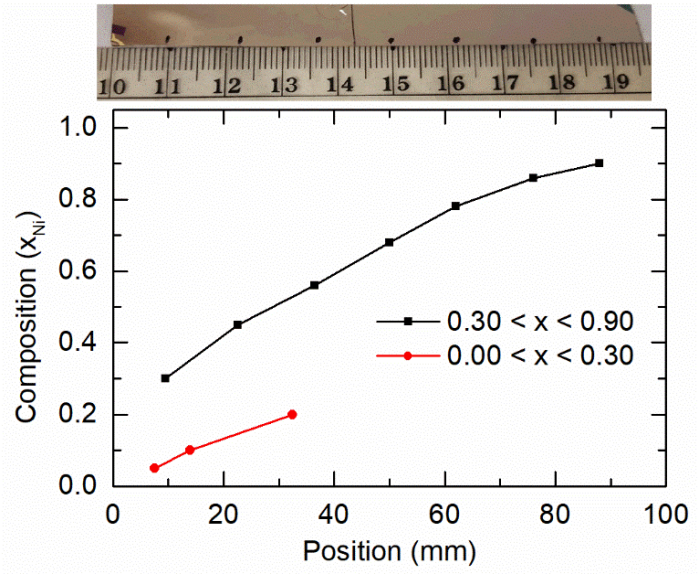

Figure 3.1. EDS measured composition versus position demonstrating composition gradient across sample.

(111) and (200) reflections for Au and Ni. In the second set of samples, the incidence angle was set to 21º to maximize the diffracted beam intensity collected. The data were collected again in the range of 35º to 55º.

3.2.3.4. Dielectric Function Measurement

The complex dielectric function was measured via a J.A. Woolam M-2000U variable-angle spectroscopic ellipsometer in the range of 1.24 to 5.06 eV. The angle was fixed at 65º and the spot size was 4 mm x 8 mm. Again, the change in composition over the 4mm spot size is less than 0.0308 x_{Ni}. The alloy films are optically thick and optically smooth, which enables the utilization of a point-by-point fitting of the experimental data to produce Re(ε) and Im(ε). Due to no dispersion model existing that was well suited for our films, no model was used to fit the results.

3.2.3.5. Dielectric Function Analytical Model

The Drude-critical point model desc ribed in Etchegoin et al. was used with three critical points (D-3CP):

$$\varepsilon(\omega) = \varepsilon_\infty - \frac{\omega_p^2}{\omega^2 + iG_p\omega} + \sum_{j=1}^{3} A_j \left[\frac{\mathrm{e}^{\mathrm{i}\phi_j}}{\omega_j - \omega - \mathrm{i}G_j} + \frac{e^{-i\phi_j}}{\omega_j + \omega + \mathrm{i}G_j}\right] \qquad (1)$$

Where the Drude contribution is described by ε_∞, the high-frequency limit dielectric constant, ω_p, the plasma frequency, and G_p, a damping term. The three critical point transitions are each described by an amplitude (A_j), phase (ϕ_j), gap energy (ω_j), and broadening term (G_j). The phase term has a cyclic behavior and repeats every 2π as demonstrated in **Figure A.3.1** In total, there are 15 parameters to describe each composition.

The objective function was selected to be the chi-squared distribution function [17] [165]:

$$f = \frac{1}{2N}\sum_{i=1}^{N}\left[\frac{\left(\mathrm{Re}_c(\omega_i) - \mathrm{Re}_e(\omega_i)\right)^2}{|\mathrm{Re}_e(\omega_i)|} + \frac{\left(\mathrm{Im}_c(\omega_i) - \mathrm{Im}_e(\omega_i)\right)^2}{|\mathrm{Im}_e(\omega_i)|}\right] \qquad (2)$$

Where N is the number of data points, $\mathrm{Re}_c(\omega)$ and $\mathrm{Im}_c(\omega)$ are the calculated dielectric function components, and $\mathrm{Re}_e(\omega)$ and $\mathrm{Im}_e(\omega)$ are the experimental dielectric function

components. For fitting, we employ the built-in *Matlab* algorithm, *GlobalSearch*, using the *fmincon* algorithm. In short, *GlobalSearch* is an efficient search tool to find the global error minimum of a problem by running the fmincon algorithm several times from various starting points within the boundary conditions. Similar to Rioux, we allow each of the 15 parameters to vary quadratically with composition [18]:

$$\omega_p^{x_{Ni}} = a + b(x_{Ni}) + c({x_{Ni}}^2) \quad (3)$$

Where x_{Ni} is the atomic Ni fraction, and a, b, and c are the constant, linear, and quadratic coefficients respectively. The optimization routine simultaneously fits all 12 experimental composition data sets and varies the coefficients to minimize the objective function. In total, there are 45 parameters (3 coefficients x 15 model parameters) needed to fully describe the system.

To model the annealed samples that exhibited phase separation, we utilized a simple composition-weighted average of dielectric functions based on the volume fractions of the Au- and Ni- rich phases. Vegard's Law and the Au-Rich (111) and Ni-Rich (111) peak position from the XRD data was used to determine the approximate phase composition of the two primary phases. The volume fraction of each phase is then determined using the lever rule with the compositions found above. Using our D-3CP model, we calculate the dielectric function of the Au- and Ni- rich phases. Lastly, we use a simple composition-weighted average of the two dielectric functions based on the volume fraction of the two phases to model the effective dielectric function of the annealed samples.

$$\varepsilon(\omega) = \varepsilon_{Au-rich}(1 - x_{Ni}) + \varepsilon_{Ni-Rich}(x_{Ni}) \quad (4)$$

3.2.4. Results and Discussion

3.2.4.1. Full Compositional Range Study

The as-deposited films form a metastable solid solution, and each exhibited 2 main reflections in GIXRD experiments that were characteristic of an FCC crystal structure. As the amount of Ni increased, reflections shift to higher 2θ consistent with the change in the lattice parameter as can be seen in **Figure 3.2**, the reflections shift from that of pure Au

toward that of Ni. The shift is approximately linear and follows Vegard's law **(Figure A.3.2.).** Between x = 0.45 and 0.96, the main (111) peak is broadened and, in some cases, appears to be a combination of two super saturated solid solution peaks.

The as-deposited films exhibited a fairly continuous shift in the dielectric constant as the concentration varied from pure gold to pure nickel. At energies above 2.5 eV, gold has a less negative Re(ε), whereas below this energy gold has a very large negative value which is consistent with its low energy plasmonic behavior. Starting from pure gold, small additions of nickel severely decreases the magnitude of the real part of the dielectric constant. The $Au_{0.14}Ni_{0.86}$ alloy data is in good agreement with that of $Au_{0.15}Ni_{0.85}$ that was previously reported [159]. While in general Im(ε) also shifts almost continuously from pure gold to pure nickel with increasing nickel concentration, in one composition region a discontinuity exists in the values near the 2 eV range, as will be discussed below. As a measure of the suitability of the alloys for plasmonic materials, the peak in the LSPR quality factor, Q-factor, around 1.8 eV is greatly damped compared to that of pure Au (~22). Interestingly, the peak maximum demonstrates a nearly linear shift to higher energy with increasing Ni fraction, but the intensity of the peak decreases exponentially as observed in the inset of **Figure 3.3g**.

In order to rationalize the changes in the dielectric function with composition, we model each composition's dielectric function with a Drude-three critical point (D-3CP) model and observe how the model parameters change with composition. The parameters and fit values for each composition are summarized in **Table A.3.1**. For example, the total fit and individual components of the fit are plotted for the real and imaginary components of the dielectric function for the $Au_{0.42}Ni_{0.58}$ alloy in **Figure 3.4a** and **Figure 3.4b**, respectively. The parameter trends for energy (ω) and broadening (G) are shown in **Figure 3.4c** and **Figure 3.4d**; the amplitude and phase parameters are shown in **Figure A.3.3.** The parameters all exhibit a quadratic behavior with composition. The coefficients governing the behavior are tabulated in **Table 3.2**. Some energy parameters were forced to be negative in order to produce a smooth trend. However, the solution is not unique: for instance, the sign of the energy can be positive by subtracting π from the value of ϕ and multiplying the

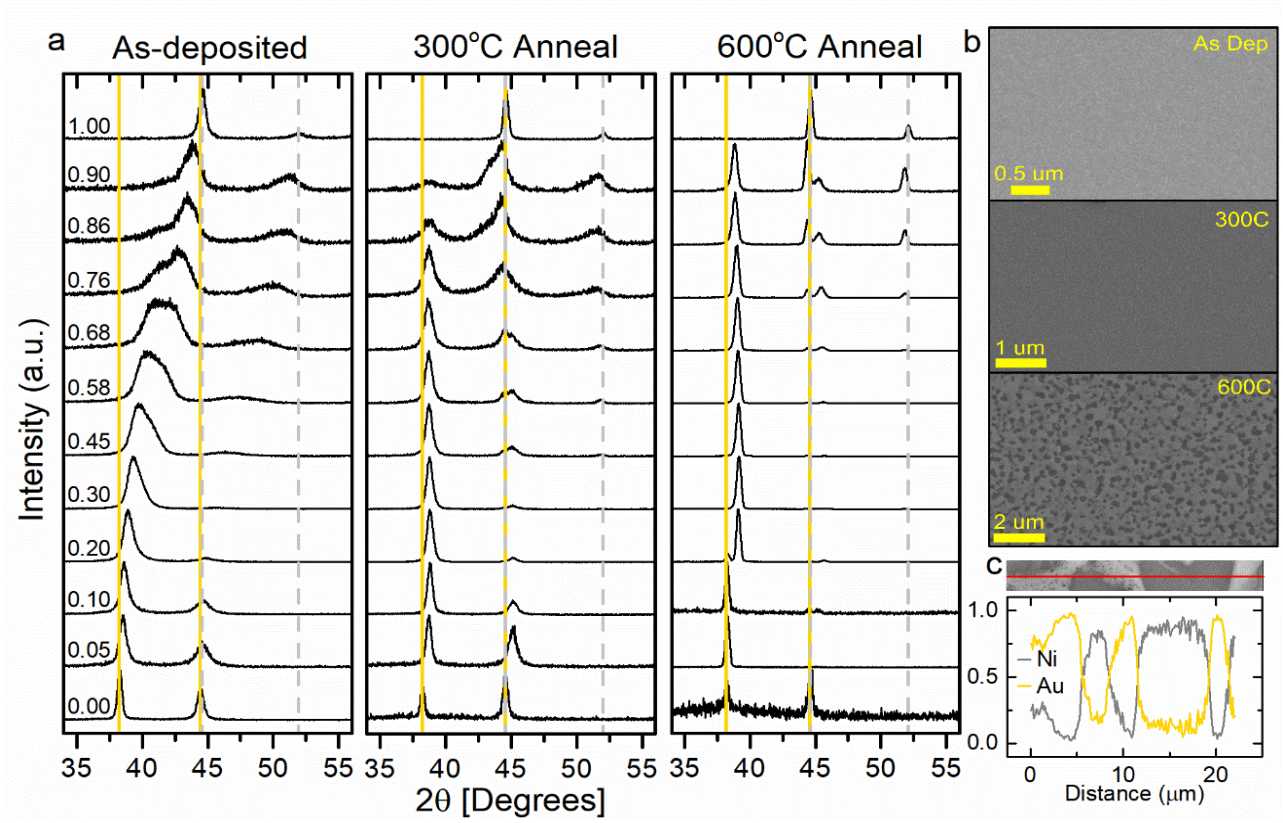

Figure 3.2.(a) GIXRD spectra for various $Au_{1-x}Ni_x$ alloy compositions and anneal treatments. Gold lines correspond to measured pure Au (111) and (200) reflections and Gray dashed lines correspond to measured Ni (111) and (200) reflections. (b) SEM images of $Au_{0.42}Ni_{0.58}$ alloy at each anneal condition. (c) EDS line scan with normalized counts demonstrating SEM images are phase contrasted with lighter regions corresponding to Au-rich composition and darker regions corresponding to Ni-rich composition.

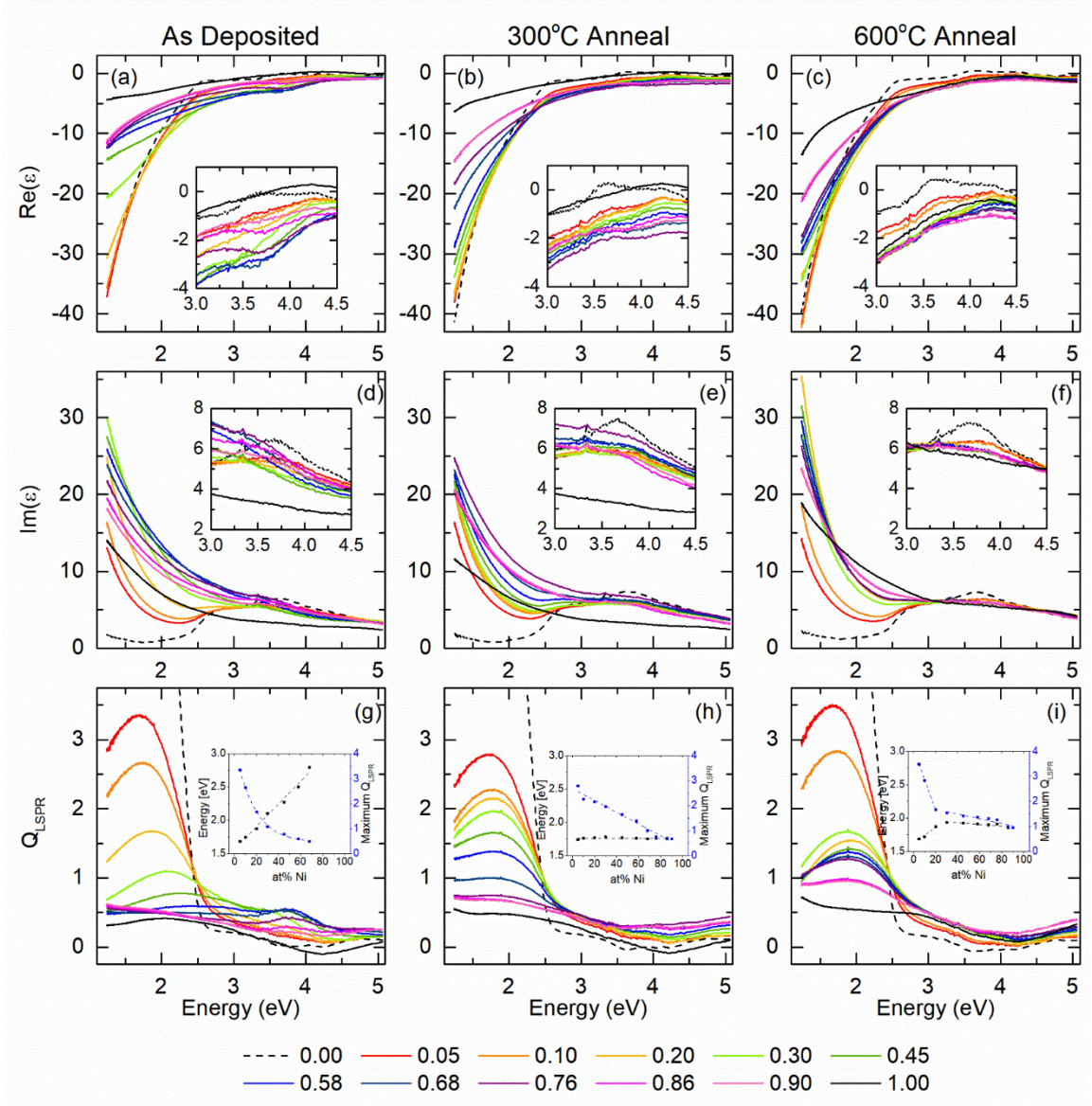

Figure 3.3. Real (a-c) and imaginary (d-f) components of the dielectric function and corresponding LSPR Q-factors (g-i) for various $Au_{1-x}Ni_x$ alloys with x indicated in the legend.

value by -1. We, however, allow these values to evolve as shown so that a smooth parameter trend is produced such that we may use the trend to predict the dielectric function of other alloys.

Subsequent to annealing at 300ºC, some phase separation into an Au-rich phase and a Ni-rich phase occurs as demonstrated in **Figure A.3.4.** . Based on the phase diagram, these phases should be approximately $Au_{0.98}Ni_{0.02}$ and $Au_{0.005}Ni_{0.995}$, respectively. GIXRD reveals 4 main reflections for each composition. The Au-rich (111) peak is located at slightly higher 2θ than pure Au (111) and is approximately constant for each alloy. A slight shift to lower 2θ in the Ni-rich reflections also occurs consistent with gold alloying. By applying Vegard's law, we can use the Au-rich (111) and Ni-rich (111) reflection positions to approximate the composition. Contrary to the equilibrium values, the XRD results suggest an Au-rich composition of $Au_{0.89}Ni_{0.11}$ and the Ni-rich composition of $Au_{0.012}Ni_{0.988}$.

Similar behavior to the as-deposited sample is observed in the real and imaginary parts of the dielectric function for the 300ºC annealed sample. However, the feature around 1.8 eV in the Q-factor does not shift with composition like it does in the as-deposited sample. The intensity decreases nearly linearly with increasing Ni content as demonstrated in **Figure 3.3h**. We attribute this to the fact that according to the equilibrium phase diagram, the sample phase separates into two phases; as most of the phases are inside the miscibility gap, the phases are the same as evidenced by constant reflections in the XRD patterns. Rather than the composition systematically changing in the as-deposited sample, the ratio of Au-rich phase to Ni-rich phase simply varies with the change in composition for the 300ºC anneal sample. The compositions with higher Au content contain a higher volume fraction of the Au-rich phase and thus have a higher Q-factor and vice versa.

In order to rationalize the changes in the dielectric function, we employ a simple composition-weighted average of an $Au_{0.89}Ni_{0.11}$ alloy (Au-rich phase) and $Au_{0.012}Ni_{0.988}$ (Ni-rich phase), which are determined using the parameter trends discussed above. The volume fractions are tabulated in **Table A.3.2**. **Figure 3.4e** demonstrates the fit for the $Au_{0.42}Ni_{0.58}$ alloy and the remaining compositions are shown in **Figure A.3.5.** . Our model

Table 3.2. Drude-3CP coefficients, a, b, and c, describing quadratic behavior of each parameter. To determine the parameter of a given coefficient, use $\boldsymbol{a + bx_{Ni} + cx_{Ni}^2}$.

	a	b	c
ε_∞	1.994	-0.318	-0.730
ωp	8.196	3.943	-7.218
Gp	0.110	4.863	-4.066
A1	7.529	-17.668	8.765
ϕ1	-1.246	-3.346	1.668
ω1	2.631	-1.733	3.634
G1	1.169	-1.359	1.384
A2	-6.688	42.094	-34.147
ϕ2	-1.591	-4.697	5.637
ω2	-0.057	-5.921	7.363
G2	-1.573	8.966	-6.917
A3	7.605	-38.201	56.981
ϕ3	-1.532	-2.816	1.312
ω3	0.842	-3.731	2.940
G3	-1.718	1.860	-0.170

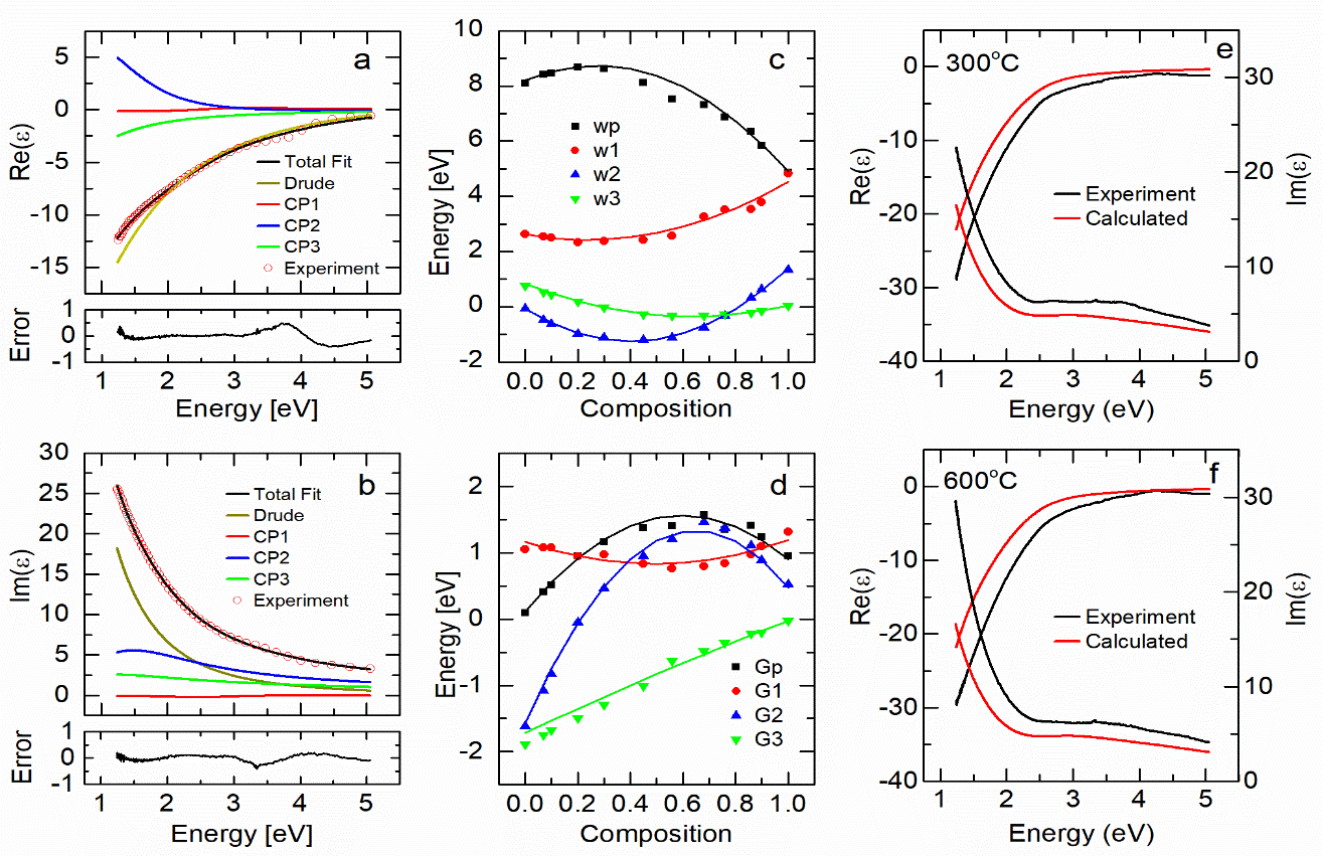

Figure 3.4. (Left) (a-b) Total fit using Drude-3CP model and four fit components which make up the total fit for the $Au_{0.42}Ni_{0.58}$ as-deposited alloy. Error plot shows fit-experiment versus energy. (Middle) Energy (c) and broadening (d) parameters versus composition, x, for $Au_{1-x}Ni_x$ alloys. (Right) Experimental (black) and calculated (red) complex dielectric function for an $Au_{0.42}Ni_{0.58}$ alloy after annealing at 300°C (e) and 600°C (f).

works fairly well for approximating the dielectric function of the alloyed films although the value is not accurate in all cases. We attribute the differences to grain size and surface roughness, which are not accounted for in our model [166].

At higher temperature, we have a larger solid solution range on the Au side of the phase diagram. At 600C, Ni has a higher solubility in Au and consequently we pick up a solid solution behavior in the $Au_{0.93}Ni_{0.07}$ and $Au_{0.90}Ni_{0.10}$ alloys. For compositions where $x > 0.30$, annealed at 600ºC, again the solid solution phase separates as evidenced by the Au-rich and Ni-rich peaks in the GIXRD pattern in **Figure 3.2**; notably the peaks are narrower indicative of larger grains as confirmed by the SEM images (**Figure A.3.4.**). At 600ºC, in the range of $0.3 \leq x \leq 0.9$, the phase diagram suggests the alloy separates into an $Au_{0.78}Ni_{0.22}$ Au-rich phase and an $Au_{0.04}Ni_{0.96}$ Ni-rich phase. Once again, we apply Vegard's law to the Au-rich and Ni-rich (111) reflections and determined that the Au-rich composition is approximately $Au_{0.88}Ni_{0.12}$ and the Ni-rich composition is approximately $Au_{0.002}Ni_{0.998}$, which are both higher than expected. We attribute this difference to the relatively slow cooling rate of our substrate heater (~16°C/minute). According to the phase diagram at 600ºC and below $x = 0.22$, the resultant microstructure should be a single-phase solid solution. Interestingly, the $Au_{0.2}Ni_{0.8}$ alloy measured at room temperature does have its main GIXRD peak at the approximate solid solution composition, however, there does appear to be an Au reflection thus some gold precipitation occurs during the cooling to room temperature. Annealing at 600ºC is very close to the boundary of the miscibility gap on the phase diagram at this composition.

Because of the extended solid solution, these materials require us to use the D-3CP modeled results in the solid solution region and then an effective medium approximation for compositions within the miscibility gap which exhibited phase separation. We rationalize the change in the dielectric function using the composition-weighted average this time with an $Au_{0.88}Ni_{0.12}$ alloy and an $Au_{0.002}Ni_{0.998}$ alloy. We only apply this to compositions where $x \leq 0.3$ as these compositions are in the miscibility gap and experience phase separation. The calculated and experimental dielectric function for the $Au_{0.42}Ni_{0.58}$ 600°C alloy is shown in **Figure 3.4f** and the remaining experimental compositions are

shown in **Figure A.3.6.** . In regard to the LSPR Q-factor, the peak shifts to higher energies for the first 3 compositions (x = 0.05, 0.1, and 0.2) consistent with the Au-Ni solid solution that exists in this region as confirmed by XRD. For the rest of the compositions annealed at 600ºC, the maximum in the Q-factor decreases in intensity nearly linearly (but less steep than the 300°C samples) and the peak maximum remains approximately constant but shifted to higher energy relative to the 300ºC sample. This trend is expected due to the Au-rich phase in the 600ºC annealed samples having more Ni than that of the 300ºC samples.

3.2.4.2. $Au_{0.35}Ni_{0.65}$ Anneal Temperature Dependence Study

To study how temperature affects the phase evolution and grain size we performed an annealing study on the $Au_{0.35}Ni_{0.65}$ composition, a composition near the maximum in the miscibility gap. The annealing temperature should dictate the phase compositions and subsequent phase fractions. For example, at lower annealing temperature, we expect the alloy to phase separate into nearly pure Au and pure Ni because of the limited solubility; whereas at a higher temperature the phases will contain higher solute concentrations in both the Au- and Ni-rich phases.

XRD patterns for samples annealed at various temperatures (all 1 hour) are shown in **Figure 3.5a**. The as-deposited film is again a solid solution as discussed above. The film annealed at 150ºC is also a solid solution and thus we infer the annealing time at this temperature was not sufficient to induce the phase separation in the film. This is evidenced by no shift in the XRD peaks, a very similar dielectric function to the as-deposited film, and no noticeable contrast or grain growth in the SEM image. The remaining samples exhibited a gradual shift in the Au-rich (111) peak to higher 2θ, indicating increased Ni content in the Au-rich phase as anneal temperature increased. Concurrently, the Ni-rich (111) peak exhibited a decrease in 2θ with increasing anneal temperature, indicative of increasing Au content. Here, we see there is a larger total shift in the Au peaks than the Ni peaks, which results from the fact that Ni is more soluble in Au than Au is in Ni.

The complex dielectric function and LSPR Q-factor are shown in **Figure 3.5c-e**. Re(ε) behaves similarly to pure Au at lower energies and pure Ni at higher energies. In general, Im(ε) behaves more closely to Ni for the whole spectrum. Again, we utilize the analytical

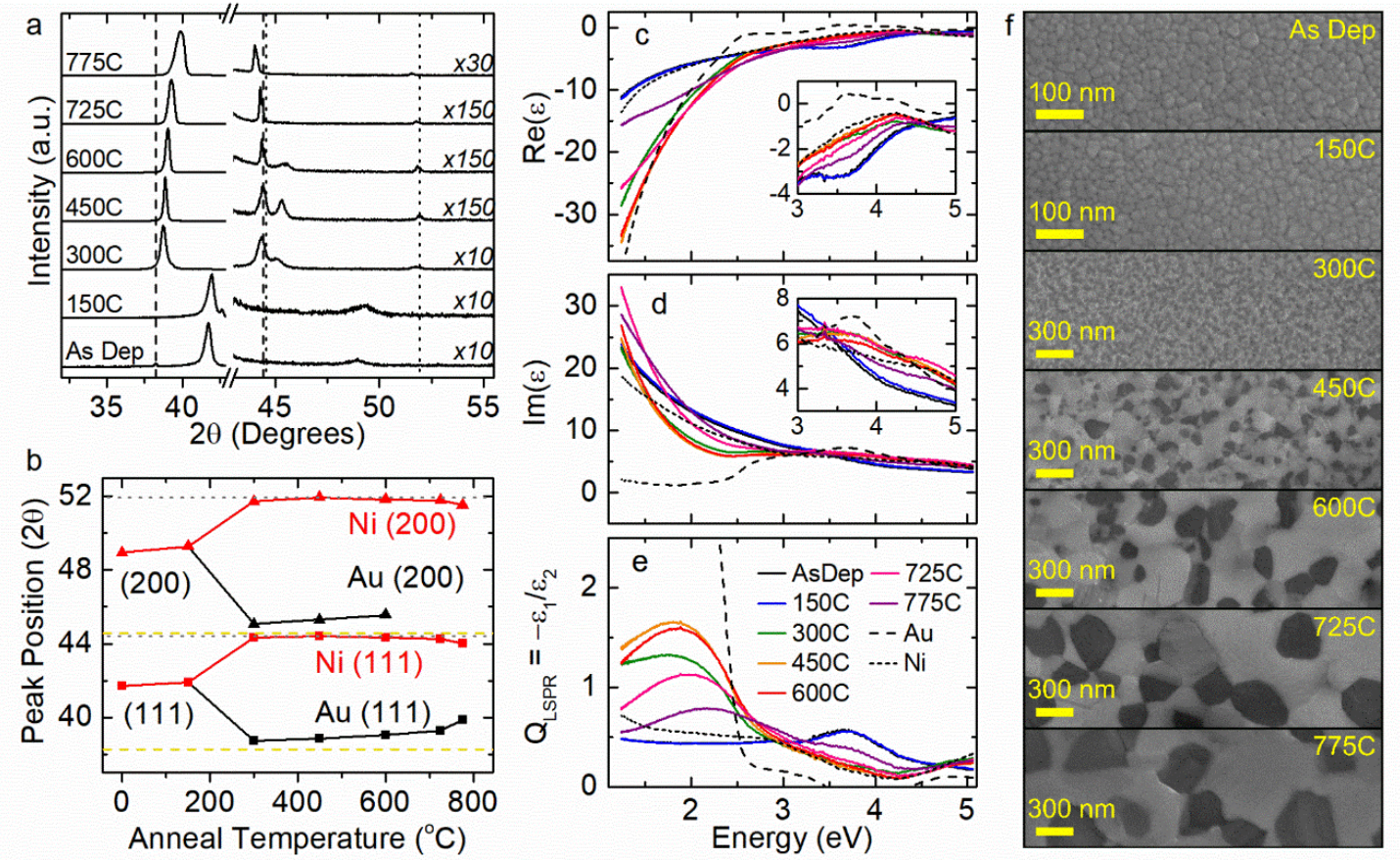

Figure 3.5. (a) XRD spectra of $Au_{0.35}Ni_{0.65}$ films for various anneal conditions and (b) corresponding peak positions as a function of temperature demonstrating the shift that occurs with annealing temperature. Real (c) and imaginary (d) components of the dielectric function and corresponding LSPR Q-factor (e). SEM images (f) of $Au_{0.35}Ni_{0.65}$ films for each anneal condition. Dark areas correspond to Ni-rich grains lighter areas are Au-rich grains.

model described above to rationalize the change in the dielectric function; the dielectric functions from each phase are determined by the as-deposited solid solutions and the effective medium approximation used based on the appropriate volume fractions of each phase. **Figure 3.6** demonstrates the calculated dielectric function for the 775°C annealed sample compared with the experimental data. Results for other temperatures are shown in **Figure A.3.7.** . Additionally, the compositions and volume fractions for each temperature are tabulated from the XRD data and summarized in **Table A.3.3**. The main feature in the Q-factor (~1.8 eV) is similar to that of pure Au but is significantly damped. There are logical shifts in the Q-factor peaks, consistent with the estimated composition of the Au-rich phase; namely the peak shifts gradually to higher energy as the equilibrium composition of the Au-rich phase is enriched in Ni as observed above. The highest Q-factor in the alloy samples comes from the films annealed at 450ºC and 600ºC. Evidently, there is a tradeoff between the Au-rich phase composition and the volume fraction. Higher annealing temperatures promote higher solubilities in the Au-and Ni-rich phases, however the purity and volume fraction of, for instance, the Au-rich phase decreases. Additionally, higher annealing temperatures produced larger grain sizes, as demonstrated in the SEM images of **Figure 3.5f**, which enhance the LSPR due to decreased scattering at grain boundaries.

The phase separation was also observed for 20 nm $Au_{0.50}Ni_{0.50}$ film using a monochromated Carl Zeiss LIBRA 200MC (S)TEM at an operating voltage of 200 kV equipped with a laser delivery system. Images were collected at 8kX. Selected area electron diffraction patterns were collected using a 5 μm aperture and subsequently radially averaged and normalized. The system is described in detail in literature [130]. The as-deposited film was a solid solution as evidenced by selected area electron diffraction (SAED) and is shown in **Figure 3.7a**. The film was then photothermally heated *in situ* using a 785 nm wavelength fiber coupled laser delivery system using a series of 200-us pulses at 13.3 mW. SAED patterns and TEM images were collected after 3, 4, 5, and 6 pulses to observe changes with heating and are shown in **Figure 3.7b-e**. The radially averaged and normalized electron diffraction patterns

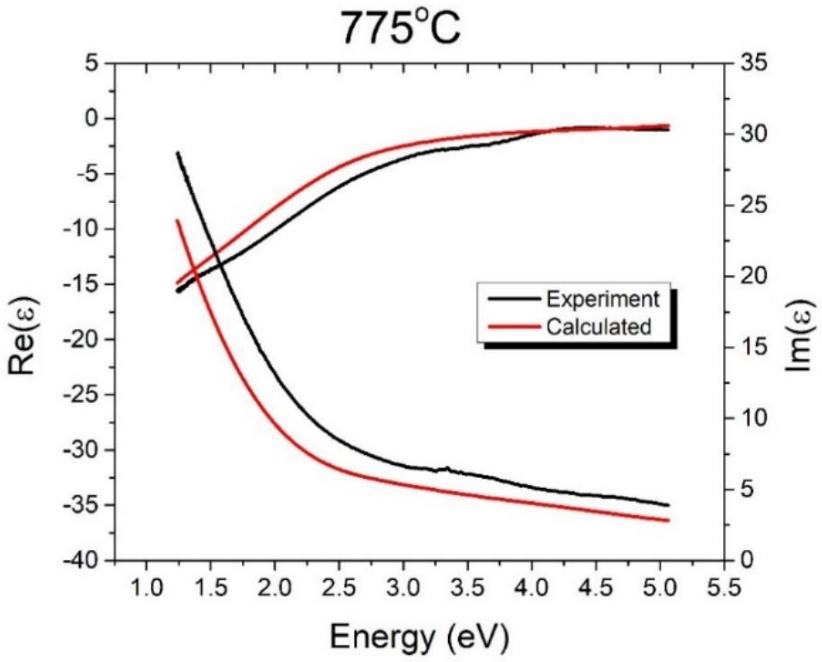

Figure 3.6. Experimental (black) and calculated (red) complex dielectric function for an $Au_{0.35}Ni_{0.65}$ alloy after annealing at 775°C.

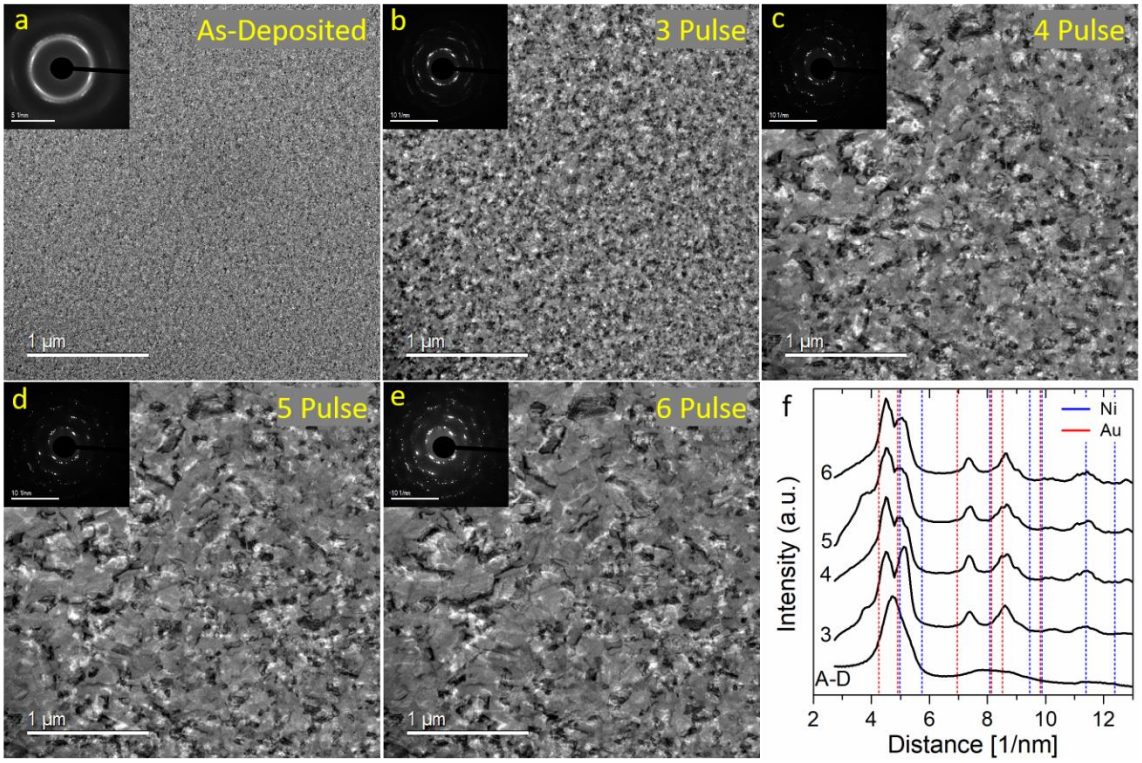

Figure 3.7. TEM images and corresponding selected area diffraction patterns (inset) of an $Au_{0.5}Ni_{0.5}$ film in the as-deposited form (a) and after a series of laser pulses (b-e). Radially averaged and normalized SAED patterns for each of the films (a-e), demonstrating that the film is a solid solution in the as-deposited form and phase separation occurs upon annealing.

are shown in **Figure 3.7f** which clearly demonstrates that phase separation occurs after just 3 pulses. See appendix 3 for further information.

3.2.4.3. $Au_{0.28}Ni_{0.72}$ Anneal Time Dependence Study

We were also interested in investigating how annealing time (at 300°C) affects the dielectric function. Annealing at lower temperatures produces films, which exhibit phase separation into Au-rich and Ni-rich phases with less solubility. Unfortunately, at these temperatures, diffusion is limited and thus phase separation and grain growth occur much more slowly. Additionally, SEM images reveal limited grain coarsening in this time scale (**Figure A.3.8**). By further increasing the annealing time, we expect the Q-factor to increase due to the presence of fewer defects in the film and the increased purity of Au-rich grains. Annealing times range from 0.5 to 10 hours.

XRD patterns in **Figure 3.8a** reveal the as-deposited film displays two reflections, intermediate to that of pure Au and pure Ni. After the 0.5 hour anneal, we already observe phase separation as evidenced by the four peaks that emerge in the XRD, with similar 2θ values to pure Au and pure Ni. However, evidence of the solid solution still remains, although the intensity of the solid solution reflection is greatly reduced. The solid solution (111) reflection is observed in all films except for the film annealed for 10 hours. Interestingly, the center of the solid solution reflection generally shifts to higher 2θ values with increasing time, which is characteristic of preferential Au out-diffusion.

The dielectric function, shown in **Figure 3.8b-d**, of the as-deposited film behaves similar to pure Ni in the real component, however, exhibits increased losses in the imaginary component. Annealed samples exhibit very similar dielectric functions. However, upon looking at the Q-factor, we see that an increase in anneal time causes an increase in the Q-factor below 2.5 eV.

3.2.5. Conclusions

The dielectric function of $Au_{1-x}Ni_x$ thin film alloys was correlated with the composition and phases present for as-deposited and annealed films. As-deposited films exhibited a supersaturated solid solution across the entire composition range and had a smooth transition in the dielectric function with increasing Ni fraction. The solid solution dielectric

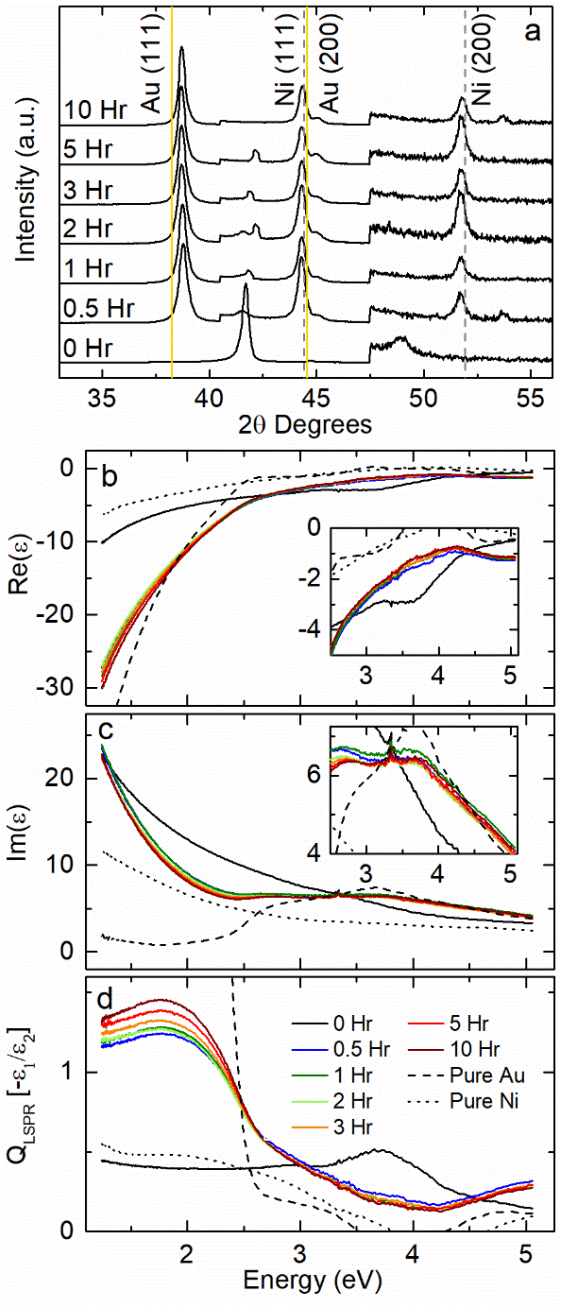

Figure 3.8. (a) Grazing x-ray diffraction spectra for $Au_{0.28}Ni_{0.72}$ alloys annealed at various temperatures. The spectra were initially normalized to the largest peak. In the range of 40.5 to 47.5 2θ, normalized spectra of annealed films are multiplied by a factor of 5. Above 47.5 2θ, normalized spectra are multiplied by a factor of 100. (b-d) Complex dielectric function for annealed $Au_{0.28}Ni_{0.72}$ films and calculated LSPR Q-factor for each annealed film.

functions were modeled using the Drude-critical point model with three critical points. The model parameters were well behaved, and each had a quadratic behavior with composition, allowing us to fit the parameter trends and use them to estimate the dielectric function of intermediate alloys not explicitly measured. Annealed films phase separated into Au- and Ni- rich grains whose compositions depended on the anneal temperature. We demonstrated that the dielectric function of phase separated alloys can be estimated using a composition-weighted average of the Au- and Ni- rich dielectric functions, which were determined using the Drude-3CP model. Additionally, we investigated the temperature and time annealing effects on a fixed alloy composition. With increasing temperature, we observed increased grain growth and decreased purity of the Au-rich and Ni-rich grains. The Q-factor was the largest for 450°C and 600°C annealed samples, suggesting there is a trade-off between grain size and composition. By annealing at a low temperature for increasing times, we found that the Q-factor increased. However, longer time scales are needed to fully phase separate the alloy and increase grain size to further enhance the Q-factor.

3.2.6. Appendix

3.2.6.1. Supporting Information

To approximate the temperature of the film during *in situ* TEM annealing, a COMSOL simulation was employed. SAED patterns were collected approximately 5 μm from the laser spot center, and thus the temperature was modeled for the center of the laser spot as well as 5 μm from the center. Thermal conductivity is a function of composition, thickness, and grain size, and thus will change during the annealing process. As demonstrated in **Figure A.3.9**, the temperature at which the film reaches during a single 200 μs pulse varies greatly with the thermal conductivity. Albeit not knowing the precise anneal temperature, phase separation as evidenced by SAED is indicative of being in the immiscible region of the phase diagram. Although, the center of the laser spot is likely much hotter as evidenced by material evaporation (see **Figure A.3.9** inset).

3.2.6.2. Figures

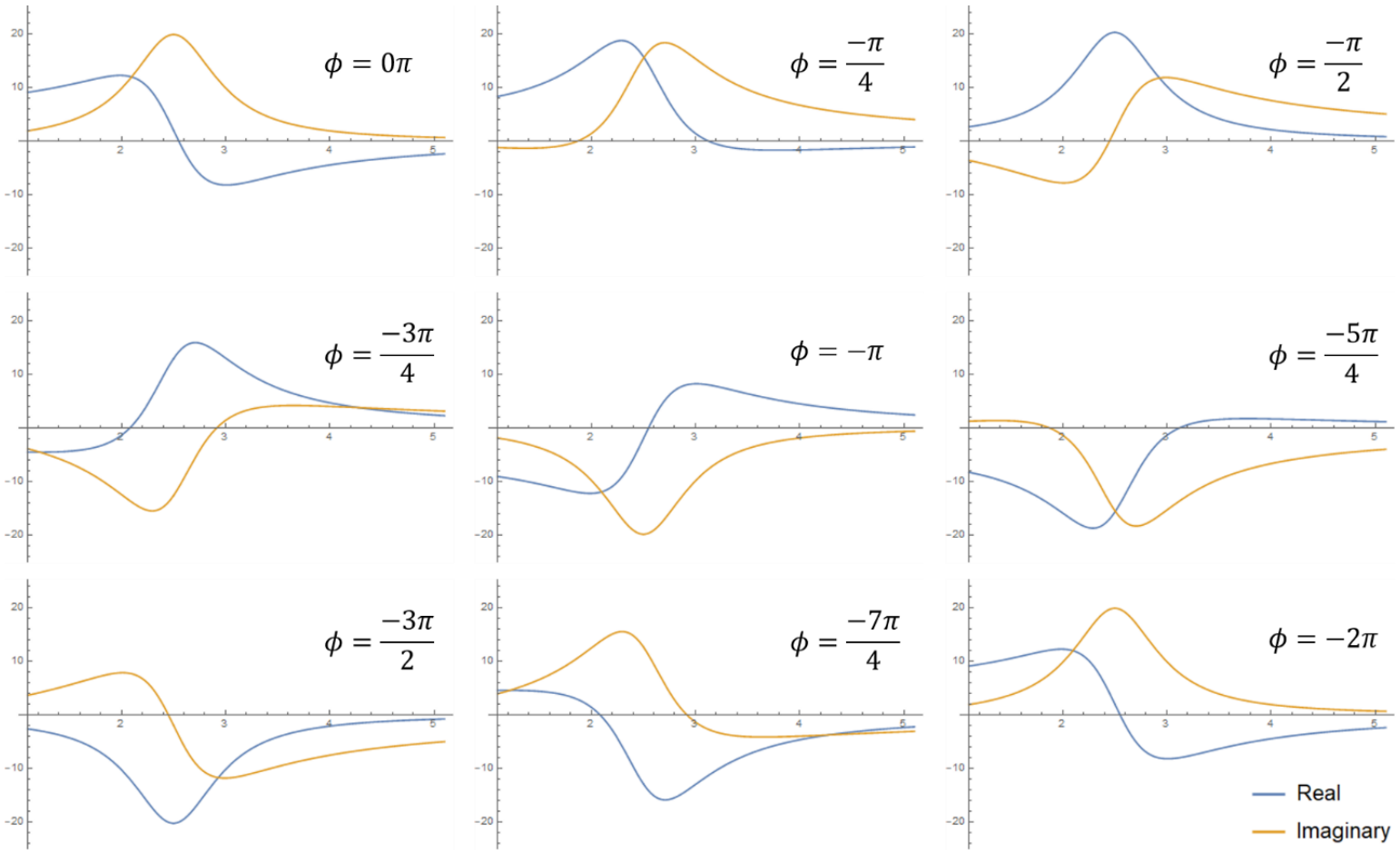

Figure A.3.1. D-CP3 model phi parameter functionality demonstrating cyclic behavior over the domain [0, 2π].

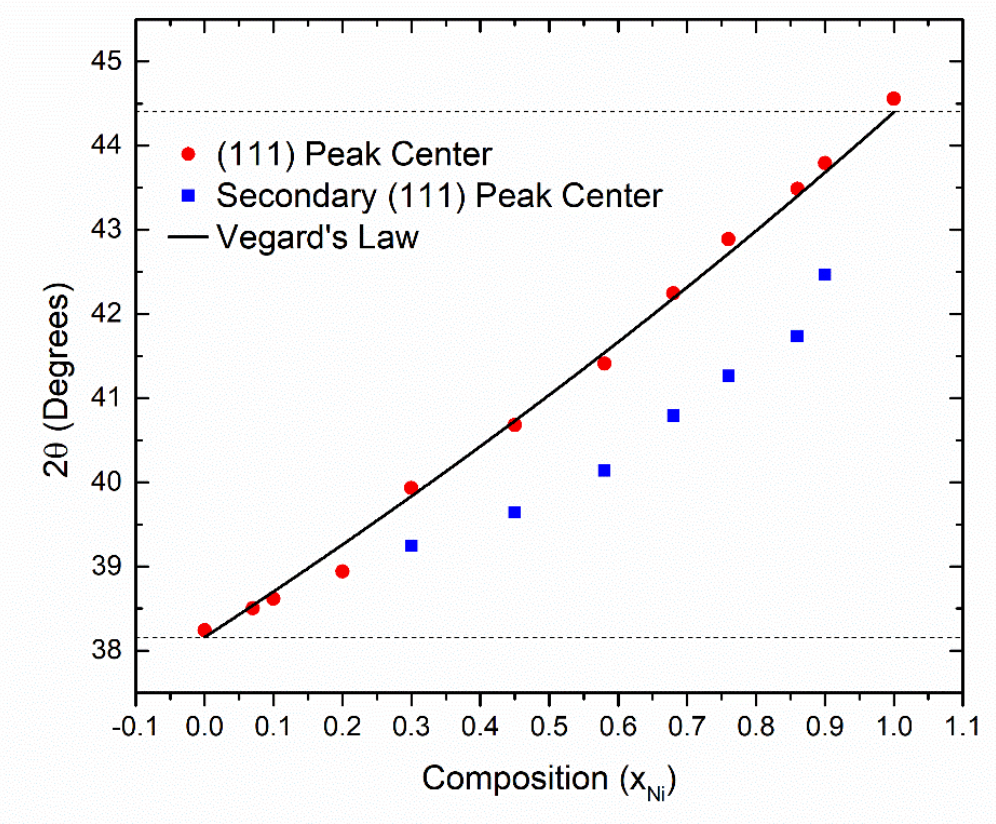

Figure A.3.2. Peak center of as deposited solid solution (111) peak. Some peaks fit with two gaussians and secondary gaussian center is shown in blue. Demonstrates how peak shift with composition follows Vegard's law. Dashed lines correspond to pure Au reflection (bottom) and pure Ni reflection (top).

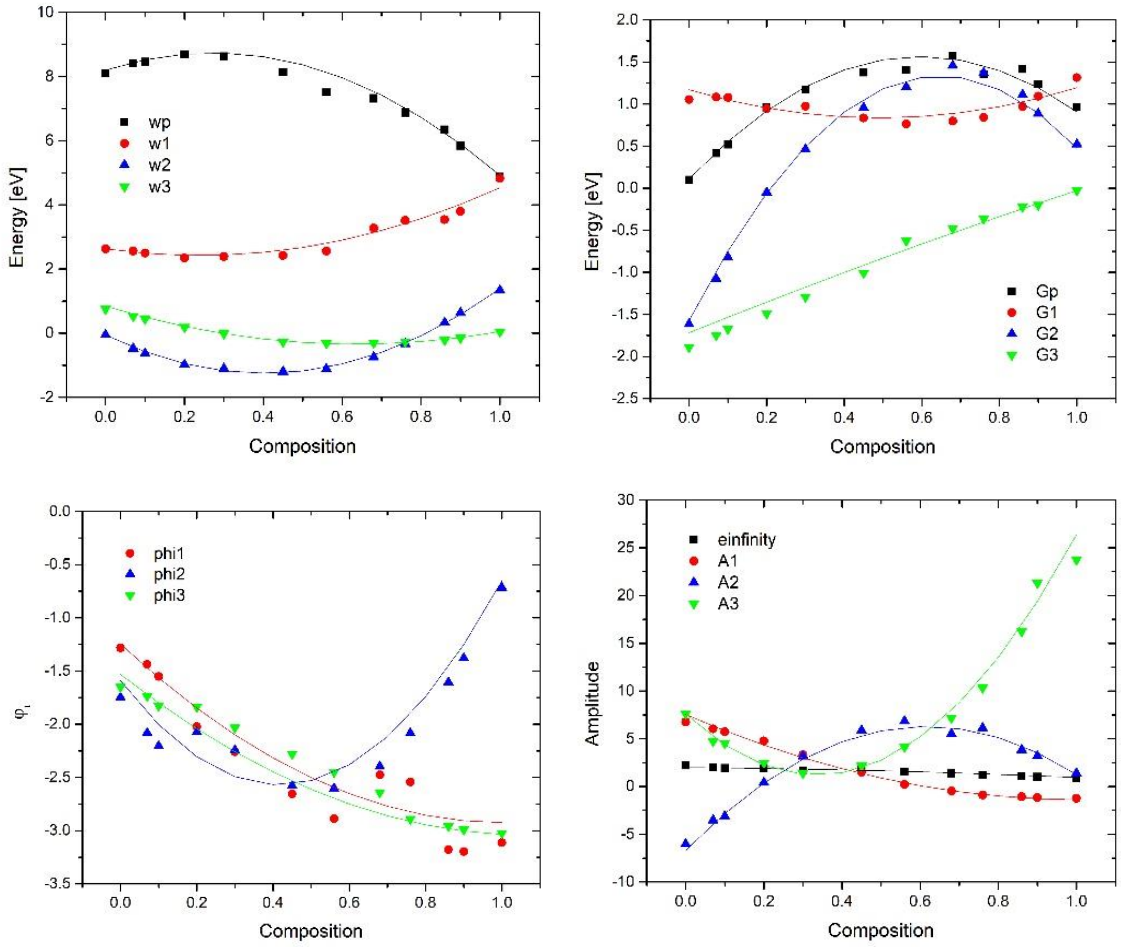

Figure A.3.3. Fit parameters from plotted as a function of Ni fraction to demonstrate smooth behavior.

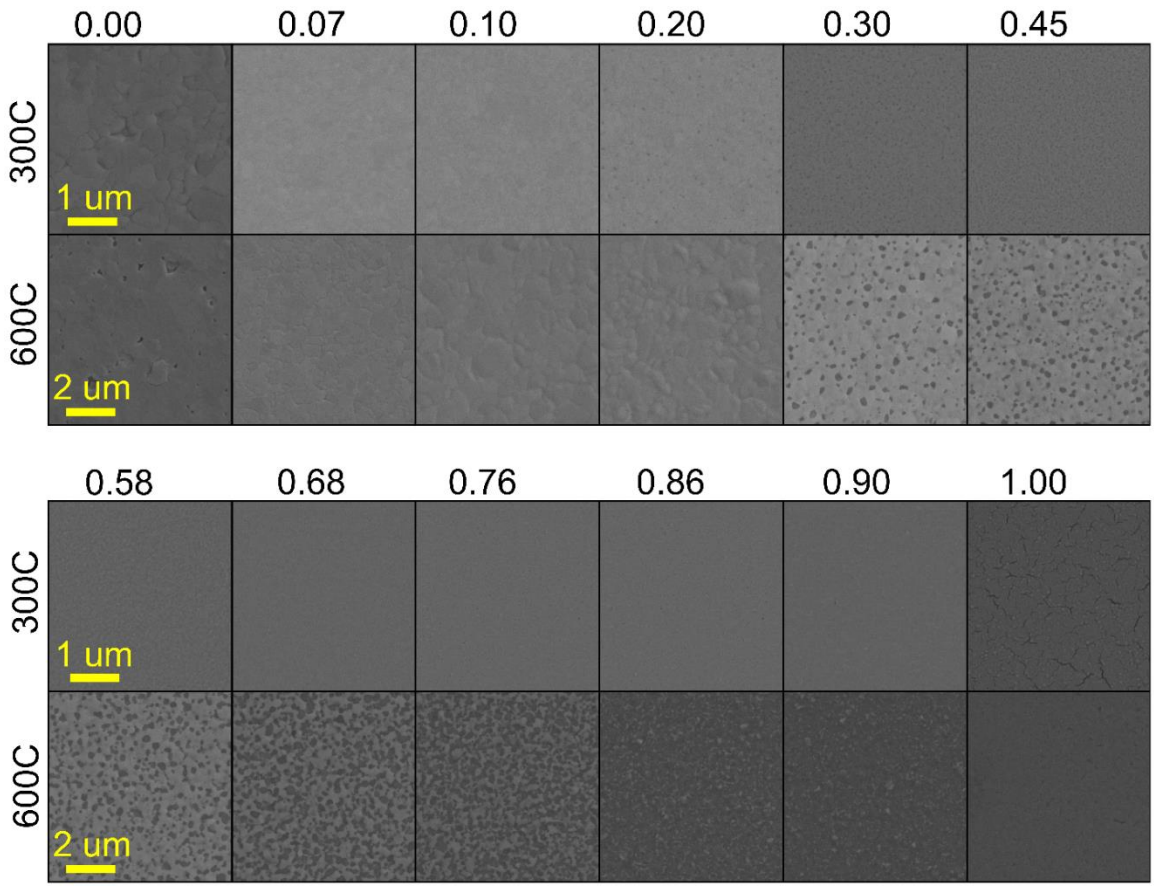

Figure A.3.4. SEM images of 300°C and 600°C annealed samples for each composition.

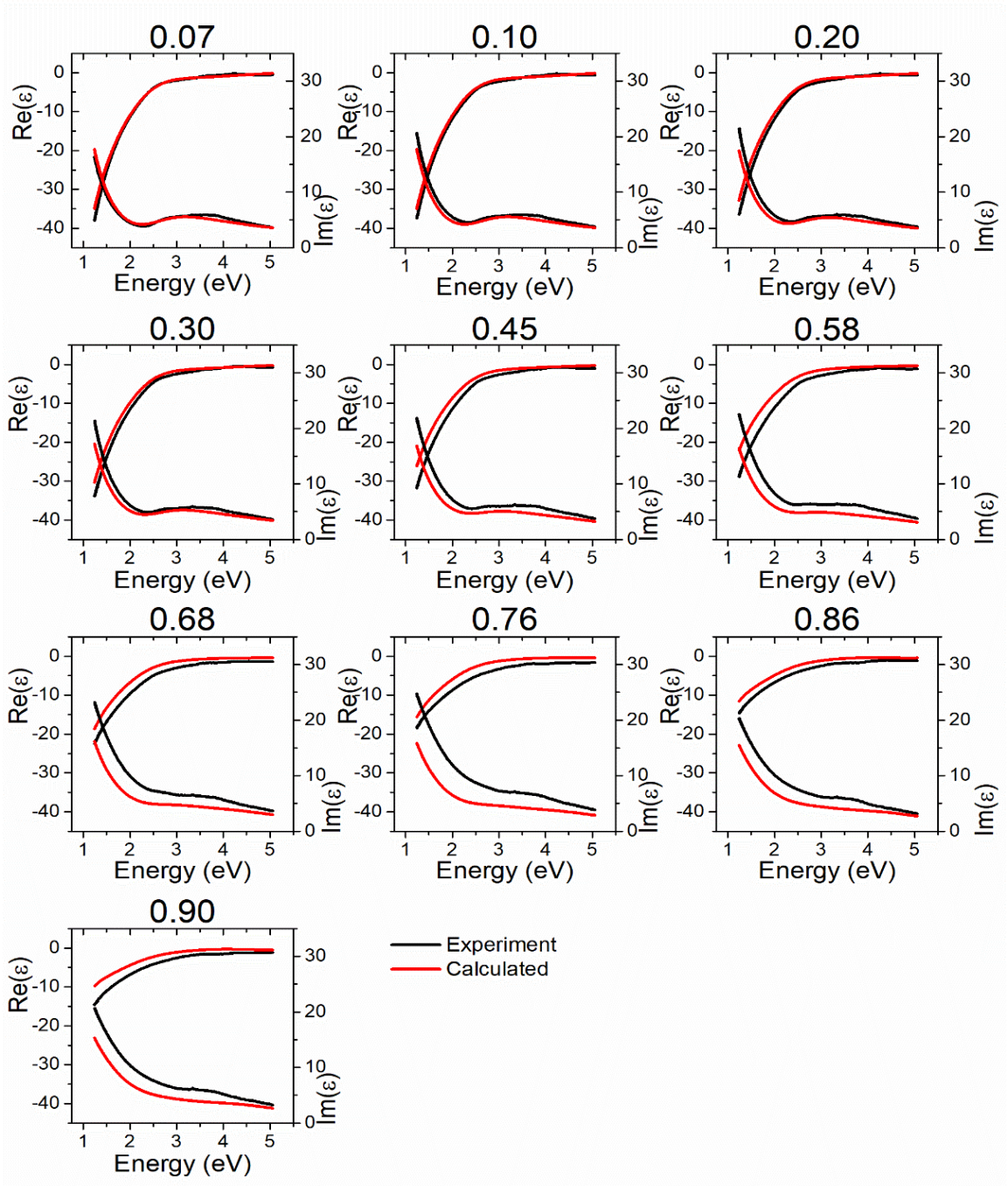

Figure A.3.5. Experimental data for the complex dielectric function compared with the calculated complex dielectric function using the composition-weighted average model for 300°C annealed samples.

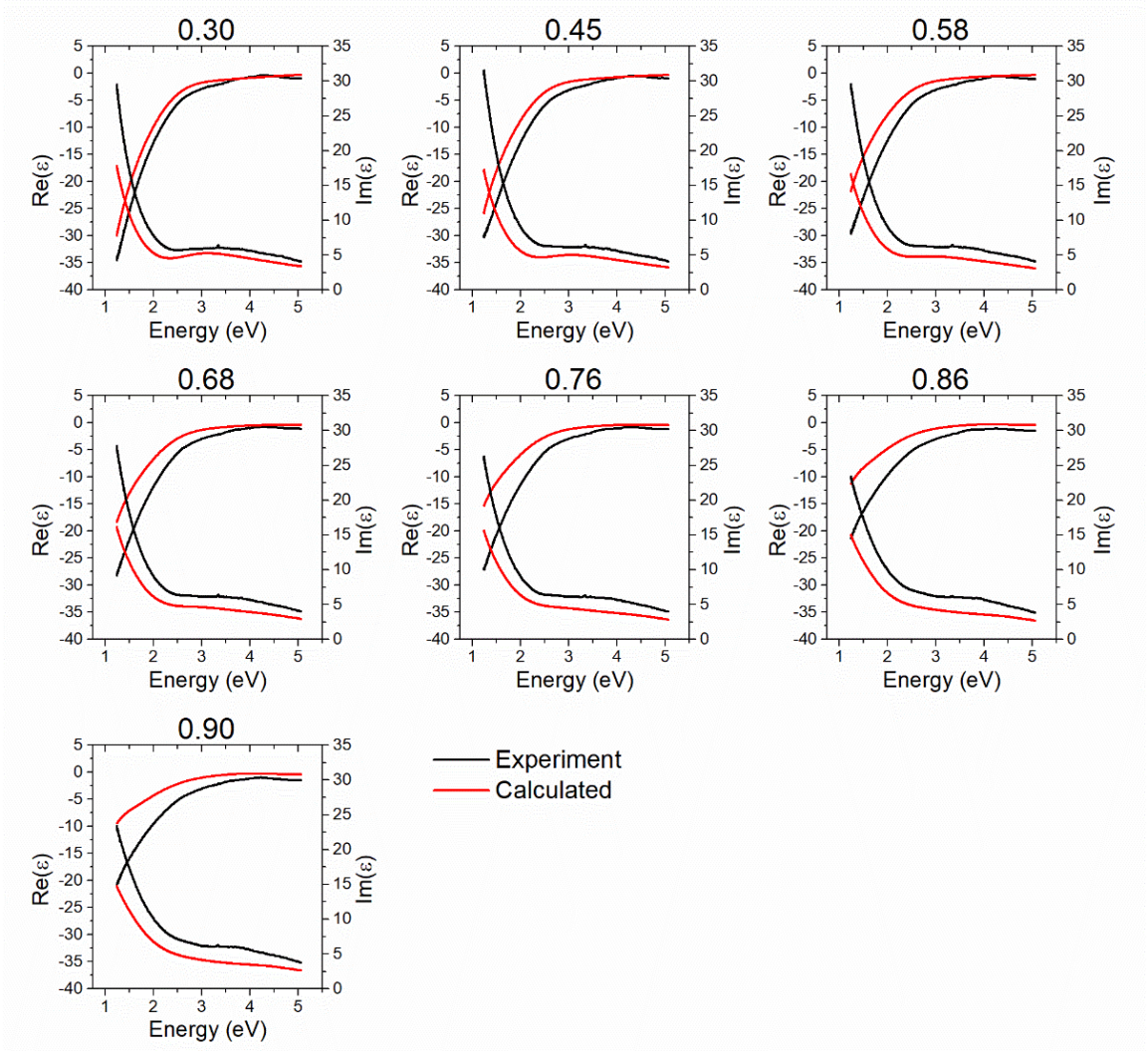

Figure A.3.6. Experimental data for the complex dielectric function compared with the calculated complex dielectric function using the composition-weighted average model for 600°C annealed samples.

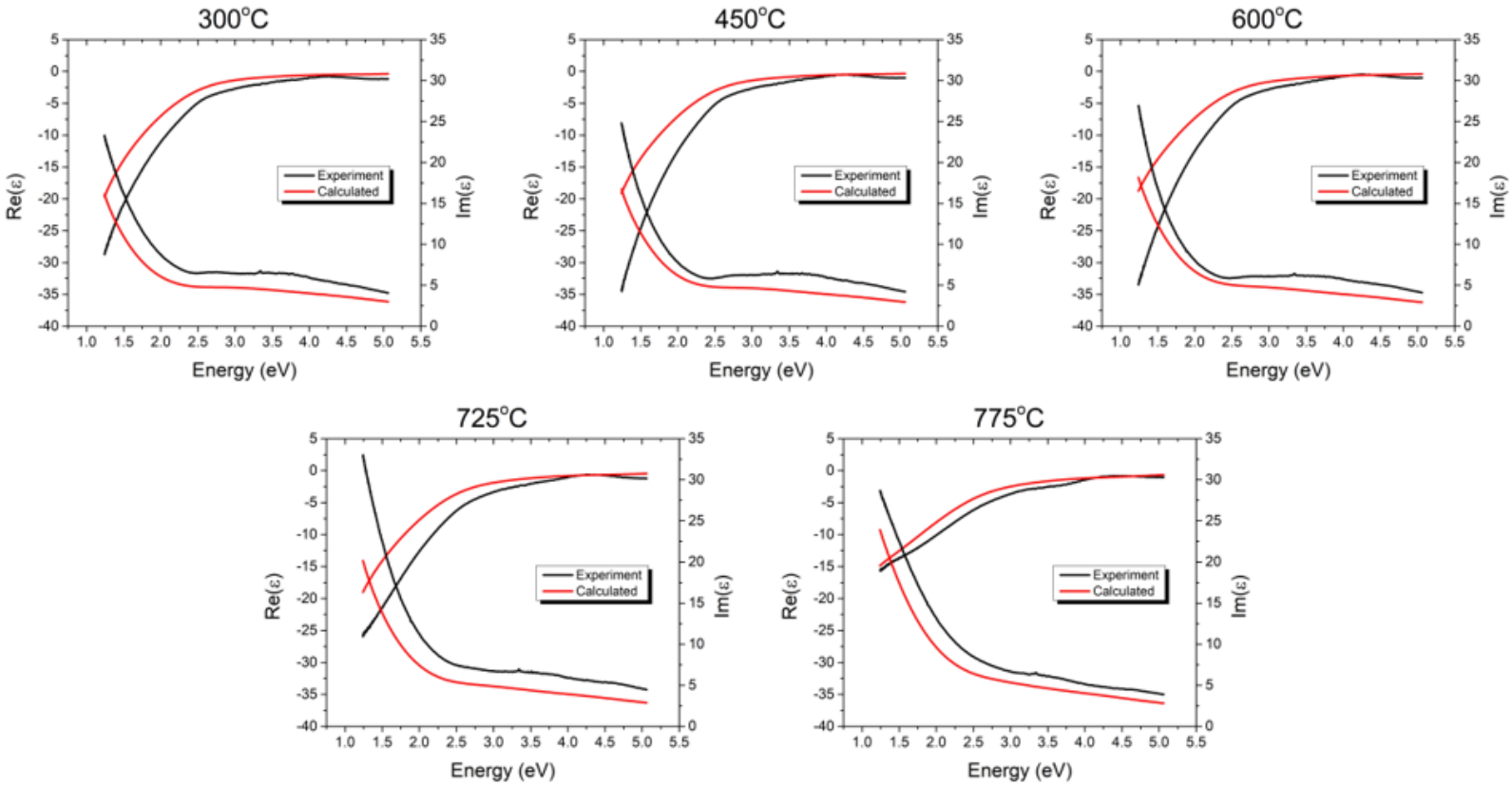

Figure A.3.7. Experimental data for the complex dielectric function compared with the calculated complex dielectric function using the composition-weighted average model for $Au_{0.35}Ni_{0.65}$ alloys annealed at various temperatures.

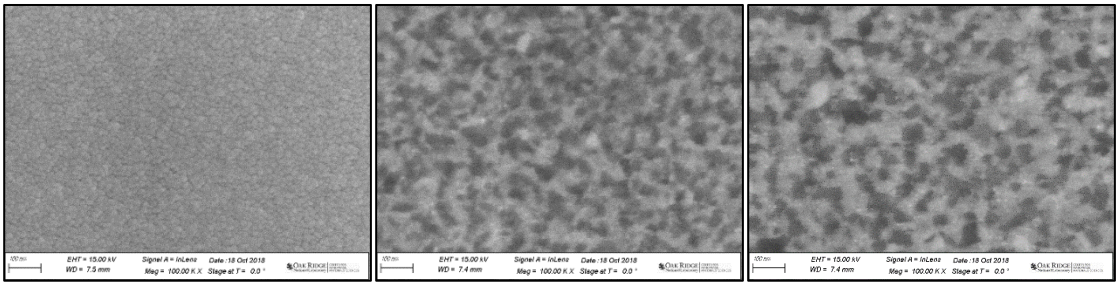

Figure A.3.8. SEM images of $Au_{0.28}Ni_{0.72}$ films comparing the as-deposited film (left) with the 0.5 hour annealed (middle) and 10 hours annealed (right) demonstrating minimal grain coarsening even after 10 hours.

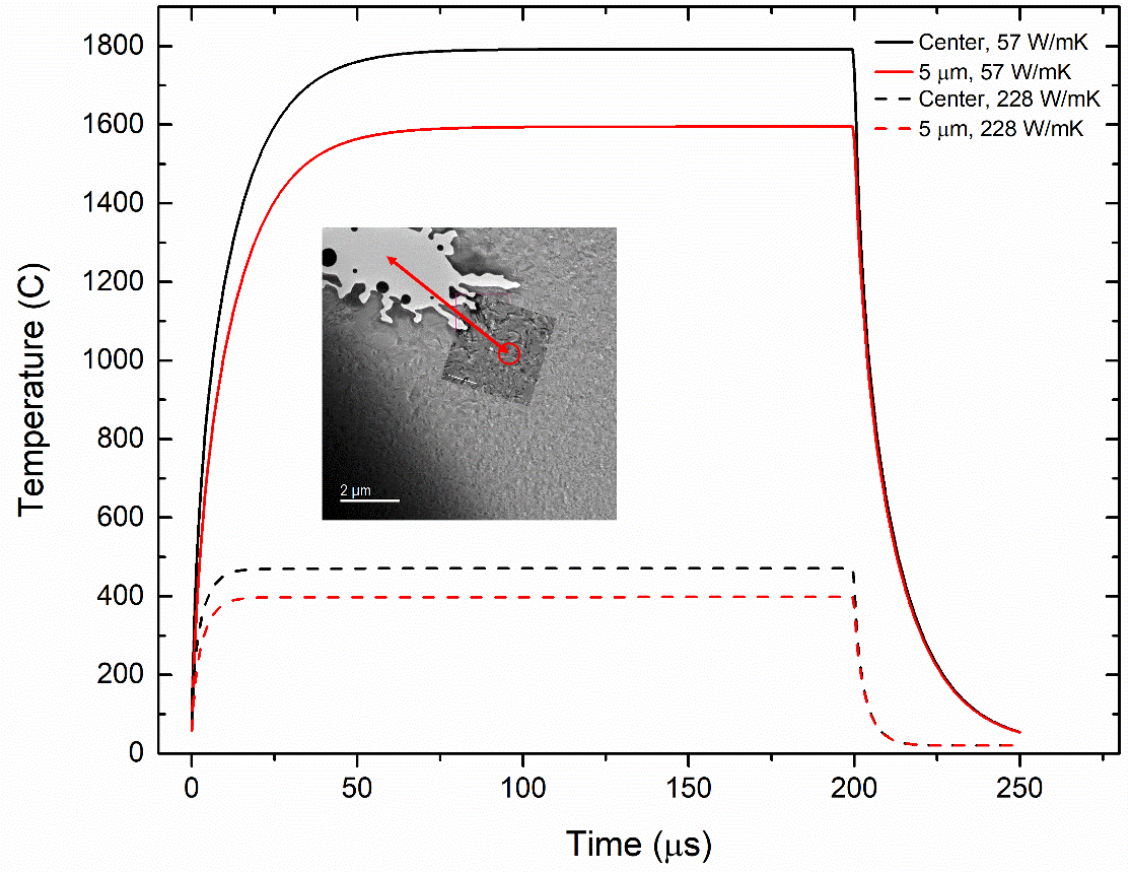

Figure A.3.9 Temperature as a function over time for one 200 us laser pulse at the center of the laser spot and 5 μm from the center for two different thermal conductivities.

3.2.6.3. Tables

Table A.3.1. Drude-3CP model parameters for each composition. Ni fraction of the alloy is listed in the first row of each column.

Parameter		0.00	0.07	0.10	0.20	0.30	0.45	0.56	0.68	0.76	0.86	0.90	1.00
Drude	einfinity	2.19	1.99	1.94	1.89	1.69	1.75	1.55	1.38	1.20	1.07	1.01	0.85
	wp	8.10	8.41	8.46	8.68	8.63	8.12	7.52	7.32	6.88	6.35	5.84	4.87
	Gp	0.10	0.41	0.52	0.96	1.17	1.37	1.41	1.57	1.35	1.41	1.24	0.96
CP1	A1	6.78	6.04	5.73	4.78	3.32	1.49	0.21	-0.48	-0.89	-1.06	-1.15	-1.24
	phi1	-1.28	-1.44	-1.55	-2.02	-2.26	-2.66	-2.89	-2.47	-2.54	-3.18	-3.20	-3.11
	w1	2.63	2.55	2.50	2.34	2.39	2.43	2.56	3.27	3.52	3.54	3.79	4.83
	G1	1.05	1.08	1.08	0.95	0.97	0.83	0.76	0.80	0.84	0.97	1.09	1.31
CP2	A2	-6.02	-3.52	-3.10	0.40	3.15	5.87	6.86	5.53	6.14	3.83	3.18	1.38
	phi2	-1.75	-2.08	-2.21	-2.07	-2.24	-2.58	-2.60	-2.40	-2.08	-1.61	-1.38	-0.72
	w2	-0.05	-0.48	-0.63	-0.98	-1.10	-1.20	-1.12	-0.75	-0.33	0.33	0.64	1.33
	G2	-1.61	-1.08	-0.82	-0.05	0.46	0.95	1.20	1.46	1.37	1.11	0.89	0.52
CP3	A3	7.61	4.74	4.51	2.47	1.40	2.15	4.15	7.18	10.3	16.2	21.3	23.7
	phi3	-1.65	-1.74	-1.83	-1.84	-2.03	-2.28	-2.45	-2.64	-2.89	-2.96	-2.99	-3.02
	w3	0.76	0.54	0.45	0.19	-0.01	-0.27	-0.31	-0.30	-0.27	-0.21	-0.15	0.05
	G3	-1.89	-1.75	-1.67	-1.49	-1.29	-1.01	-0.63	-0.48	-0.36	-0.22	-0.20	-0.03
	f	1.421	0.016	0.014	0.012	0.021	0.011	0.007	0.006	0.003	0.004	0.005	0.029

Table A.3.2. Volume fractions used in the composition-weighted average calculation for 300°C and 600°C annealed samples for each composition. No volume fractions are listed when the phase is a solid solution due to the composition-weighted average not being applicable.

Composition (x_{Ni})	**0.07**	**0.10**	**0.20**	**0.30**	**0.45**	**0.58**	**0.68**	**0.76**	**0.86**	**0.90**
300C Ni-Rich Volume Fraction (vol% Ni-Rich)	0	0	7.2	15.7	29.9	43.8	55.6	65.8	79.8	85.9
600C Ni-Rich Volume Fraction (vol% Ni-Rich)	--	--	--	14.8	28.9	42.6	54.3	64.5	78.4	84.3

Table A.3.3. Au- and Ni- rich phase estimated compositions based off of XRD reflection centers and resulting volume fraction for $Au_{0.35}Ni_{0.65}$ alloys annealed at various temperatures.

Anneal Temperature (°C)	**Au-Rich Composition (x_{Ni})**	**Ni-Rich Composition (x_{Ni})**	**Ni-Rich Volume Fraction (vol% Ni-Rich)**
300	0.108	0.991	51.7
450	0.13	1.00	50.1
600	0.161	0.993	49.5
725	0.202	0.983	48.6
775	0.307	0.949	46.1

Chapter 4

Stimulated Electron Energy Gain Spectroscopy of Plasmonic Nanostructures

4.1. Preface

A version of this chapter was originally published by R. Collette et al.:

Collette, R.; Garfinkel, D. A.; Hu, Z.; Masiello, D. J.; Rack, P. D. Near Field Excited State Imaging via Stimulated Electron Energy Gain Spectroscopy of Localized Surface Plasmon Resonances in Plasmonic Nanorod Antennas. *Sci. Rep.* (accepted Jul 6, 2020)

Robyn Collette and David A. Garfinkel prepared the samples and performed the scanning transmission electron microscope and electron energy loss/gain experiments. Zhongwei Hu and David J. Masiello performed DDA and eDDA simulation. Robyn Collette and Philip D. Rack wrote the manuscript and prepared figures. All authors discussed results and reviewed manuscript.

4.2. Near Field Excited State Imaging via Stimulated Electron Energy Gain Spectroscopy of Localized Surface Plasmon Resonances in Plasmonic Nanorod Antennas

4.2.1. Abstract

Continuous wave (cw) photon stimulated electron energy loss and gain spectroscopy (sEELS and sEEGS) is used to image the near field of optically stimulated localized surface plasmon resonance (LSPR) modes in nanorod antennas. An optical delivery system equipped with a nanomanipulator and a fiber-coupled laser diode is used to simultaneously irradiate plasmonic nanostructures in a (scanning) transmission electron microscope. The nanorod length is varied such that the m = 1, 2, and 3 LSPR modes are resonant with the laser energy and the optically stimulated near field spectra and images of these modes are measured. Various nanorod orientations are also investigated to explore retardation effects. Optical and electron beam simulations are used to rationalize the observed patterns. As expected, the odd modes are optically bright and result in observed sEEG responses. The m = 2 dark mode does not produce a sEEG response, however, when tilted such that retardation effects are operative, the sEEG signal emerges. Thus, we demonstrate that cw

sEEGS is an effective tool in imaging the near field of the full set of nanorod plasmon modes of either parity.

4.2.2. Introduction

The localized surface plasmon resonances (LSPR) sustained in noble metal nanostructures have inspired many new concepts in fields such as photovoltaics[167–169], photocatalysis[25,170,171], biosensing[172–174], readout strategies for quantum computing[175,176], and terahertz optical[177–179] and magnetic meta atoms/materials[180–183]. While standard far field optical scattering techniques are used to probe the resonance conditions of individual nanostructures as well as nanostructure ensembles, probing the resultant near field is often more challenging. Several techniques such as scanning near field optical microscopy (SNOM)[184–188], photoemission electron microscopy (PEEM)[189,190], and electron energy loss spectroscopy (EELS)[62,63,191,192] have been used to probe the near field distribution of LSPRs.

Of the near field techniques, EELS is unique in that the swift electron acts like a white (spectrally broad) evanescent field and thus can excite the full plasmonic spectrum of both bright and dark modes with atomic scale resolution. To this end, EELS has been utilized to characterize individual nanoparticle LSPRs as well as surface plasmon polaritons (SPP) and in particular the LSPR modes in nanorods[193–204].

Beyond standard EELS, photoinduced near field electron microscopy (PINEM) is used to image the near field of optically excited nanostructures[67–70,205]. In PINEM, a pulsed laser photo-ejects electron beamlets or single electrons from the cathode, which are accelerated and arrive at the specimen synchronously to a second laser pulse that interacts with the sample. Thus PINEM enables the study of photoinduced near field phenomena at the nanoscale and the intense sample laser pulse (~ $1x10^{15}$ W/m^2) induces photon stimulated electron energy loss (sEEL) and gain (sEEG) peaks. In addition to experimental demonstrations, several theoretical papers have described the sEEG and sEEL processes[65,71–73]. Additionally, by adjusting the timing of the cathode and sample laser pulse, temporal or so-called 4-dimensonal (x,y,z,t) information can be gleaned, which has

been termed 4-dimensional (x,y,z,t) ultrafast electron microscopy/spectroscopy[74–78]. While interrogating temporal aspects reveals interesting physics, the PINEM instrument is quite complex and thus only a few instruments exist worldwide.

Recently, Das et al. demonstrated that by appropriately gating the EEL spectrometer, a high frequency nanosecond pulsed laser can be used to generate characteristic sEEL and sEEG with a continuous current electron source[79]. Furthermore, by coupling to a plasmonic nanostructure with a resonance at the laser frequency they demonstrated so-called resonant sEEL and sEEG. To further extend photoinduced electron microscopy and spectroscopy, we recently developed a laser system that can be installed on any (S)TEM system. Pulsed and continuous wave (cw) photothermal heating and excitation can both be achieved. In particular, we have studied the recrystallization, grain growth, phase separation, and dewetting of an $Ag_{0.5}Ni_{0.5}$ film[130], and resonant cw sEEG and sEEL in nanostructures resulting from a dewet silver film[66].

Here we explore the cw photoexcited LSPR resonances of lithographically patterned gold nanorods with progressively longer lengths such that the m = 1, 2, and 3 longitudinal mode orders are resonant with the laser excitation energy (1.58 eV). As mentioned above, both even and odd parity LSPR modes are excited by the electron and revealed in EELS. Resonant sEEGS, however, requires far field coupling of the photons to the LSPR, thus it should be sensitive to the selection rules and retardation effects. The system (**Figure 4.1**) is oriented such that the photon propagation and the electron beam propagation directions are perpendicular and oriented 60˚ and 30˚, respectively, relative to the sample normal. Importantly the light is not polarized so all orientations can be excited as the electric field components aligned parallel to the longitudinal axis of the rods are selected by the rod antenna geometry. The nanorods are patterned such that the long axis is oriented with a component perpendicular (horizontal, **Figure 4.1a**) and parallel (vertical, **Figure 4.1b**) to the wave vector, thus we can control the s- and p-polarization of the light by tilting the sample and judiciously orienting the nanorods. Specifically, the electric field of the unpolarized light that couples to horizontally oriented rods are s-polarized, whereas the electric field of light that couples to vertical rods have a mixed s- and p-polarized

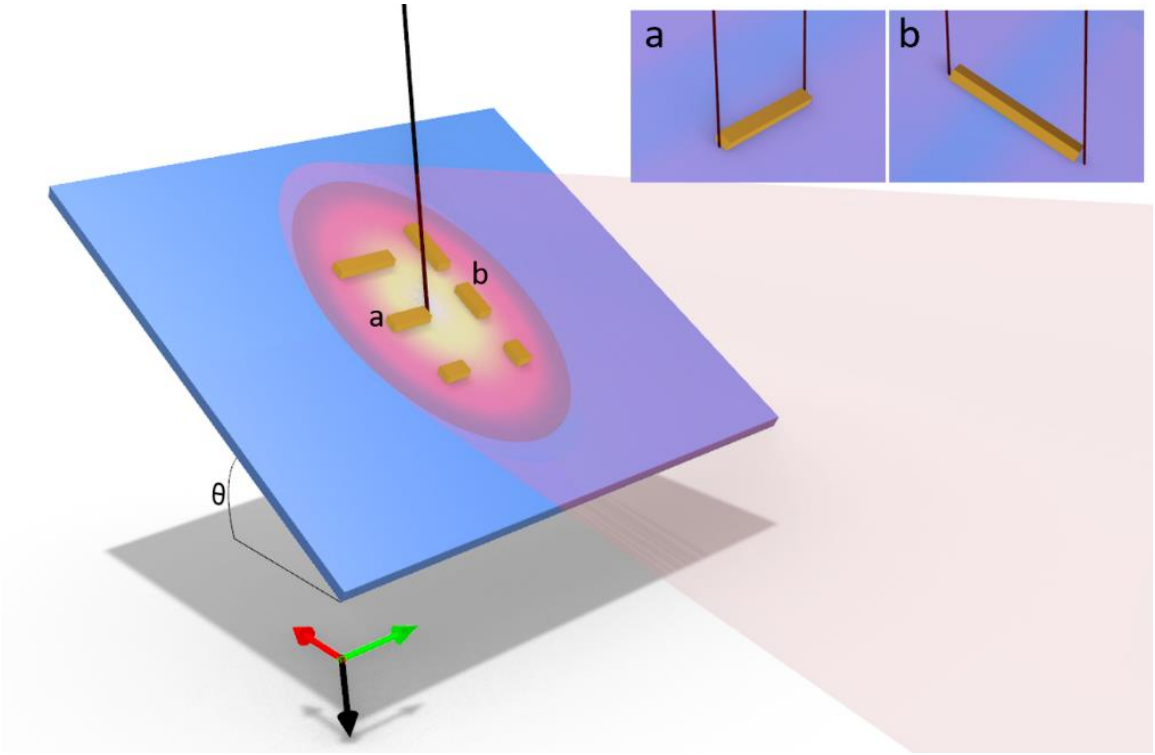

Figure 4.1. Experimental set up schematically illustrating the orientations of lithographically patterned gold nanorods aligned perpendicular and with a component parallel to the wave vector. Unpolarized light is directed toward the sample tilted at 30° (θ), thus the sample normal is oriented 30° to the electron beam trajectory and 60° to the photon wave vector. Inset shows magnified views of the nanorods illustrating the aloof positions for (a) horizontal nanorods (b) vertical nanorods and the electric field polarization component that couples to the LSPR modes.

Table 4.1. Map collection data, point spectra collection data, nanorod dimensions, and corresponding relevant mode resonance for m = 1, 2, and 3 nanorods. Subscript indicates orientation (horizontal or vertical) and laser condition (on or off).

	Map Pixel Time (s)	**Map Pixel Size (nm)**	**Spectra Frames**	**Spectra Exposure (s)**	**Nanorod Length (nm)**	**Nanorod Width (nm)**	**Peak (eV)**
$m = 1_{H, On}$	0.05	10 × 11.55	10	0.05	180	71	1.62
$m = 1_{H, Off}$	0.05	11 ×12.70	5	0.05			
$m = 1_{V, On}$	0.065	7.9 × 9.12	10	0.06	150	63	1.53
$m = 1_{V, Off}$	0.065	7.5 × 8.66	5	0.065			
$m = 2_{H, On}$	0.05	9.1 × 10.51	10	0.05	330	71	1.66
$m = 2_{H, Off}$	0.05	9.1 × 10.51	5	0.05			
$m = 2_{V, On}$	0.065	10 × 11.55	6	0.065	310	52	1.54
$m = 2_{V, Off}$	0.065	9.4 × 10.85	5	0.06			
$m = 3_{H, On}$	0.05	15 × 17.32	10	0.05	670	82	1.49
$m = 3_{H, Off}$	0.05	16 × 18.48	5	0.05			
$m = 3_{V, On}$	0.05	18 x 20.78	5	0.05	660	83	1.46
$m = 3_{V, Off}$	0.05	18 x 20.78	5	0.05			

component; thus, the vertical rods conveniently enables us to compare retardation effects in sEEGS.

4.2.3. Experimental Procedures

4.2.3.1. Sample Fabrication

Au nanorods with various dimensions and orientations (see **Table 4.1**) and 60 nm thickness were patterned on a 30 nm thick Si_3N_4 TEM membrane using electron beam lithography. Nanorod lengths were chosen such that the plasmon modes (m = 1, 2 and 3) are resonant near the 1.58 eV laser photon energy.

4.2.3.2. EEL and EEG measurements

A Zeiss Libra TEM was operated at an accelerating voltage of 200 kV in (S)TEM. The camera length is set to 378 mm. The collection semiangle (β) is 100 mrad and convergence semiangle (α) was 0 mrad. A monochromator slit of 0.5 um is used for spectrum acquisition with the dispersion set as 30 meV per channel. EELS map acquisition details are summarized in **Table 4.1**. Maps are generated using the Gatan Digital Micrograph spectra by plotting spectra intensity for specific energy slices from the 3D spectrum image data cube. Low-loss point spectrum acquisition details are summarized in **Table 4.1**. Low-loss point spectra are post processed by aligning the zero-loss peak to 0 eV, followed by normalizing to the integrated number of counts and dividing by the channel resolution. The sample is irradiated with a fiber-coupled 1.58 eV laser diode with tunable optical power up to 215 mW focused to ~ 5 μm diameter. The sample is tilted at 30° and the unpolarized Gaussian laser spot is aligned and focused to the coincident (S)TEM electron point (see [130] for system details). The laser is operated in cw mode at 1.01×10^9 W/m^2 for all laser-on results presented here. Maps and individual point spectra were acquired with the laser off and with the laser on to observe the resonant sEEL and sEEG peaks.

4.2.4. Results

First, we probe the optically bright m = 1 or dipolar LSPR mode. **Figure 4.2a** displays the EEL/G point spectra of a ~180 nm horizontal nanorod collected at the aloof position at one of the long axis ends with and without concurrent laser irradiation (see **Figure 4.2b** for nanorod image and position). The nanorod long axis is perpendicular to the photon

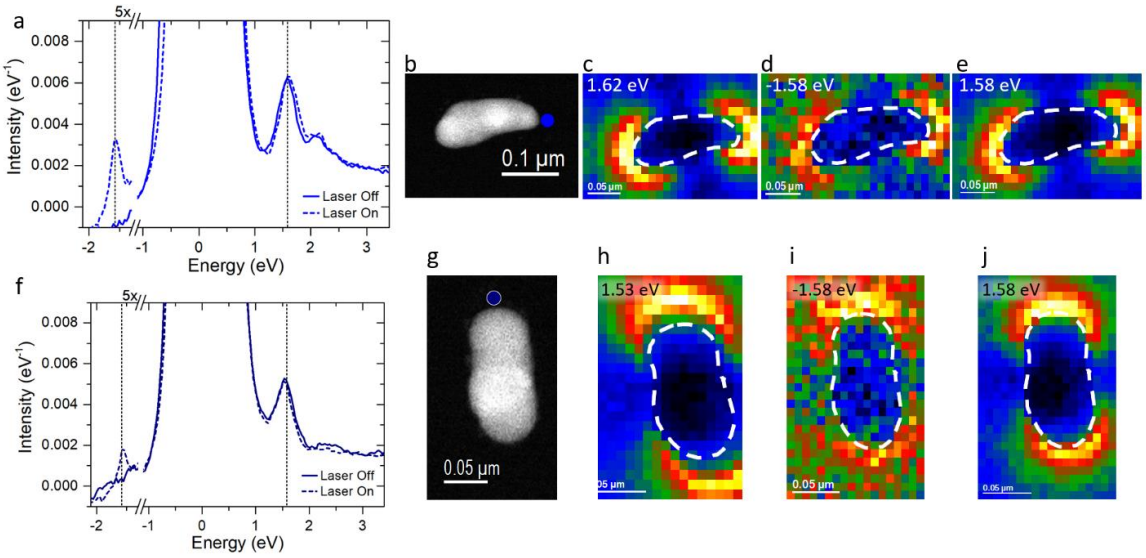

Figure 4.2. (a) Horizontal nanorod aloof 6-pixel map spectra average with laser off and on. Dashed lines in a and f correspond to the laser energy at ±1.58 eV (b) HAADF image of horizontal nanorod with aloof position indicated by blue circle. (c-e) Horizontal nanorod maps of EEL, sEEG, and sEEL peak intensities, respectively. (f) Vertical nanorod aloof 6-pixel map spectra average with laser off and on. (g) HAADF image of vertical nanorod with aloof position indicated by blue circle. (h-j) Vertical nanorod maps of EEL, sEEG, and sEEL peak intensities, respectively.

propagation direction and thus only s-polarized light couples with the nanorod. The laser-off spectrum is taken for reference and is excited by the high energy electron beam, which conveniently couples to both bright and dark plasmons and reveals the full plasmonic spectrum. The laser-off spectrum has a dipole resonance at 1.62 eV and a peak at 2.25 eV, which is attributed to the higher order LSPR modes. The laser-off 1.62 eV EELS map is shown in **Figure 4.2c**, which has the expected intensity peaks at the nanorod ends (see **Figure A.4.1.** for complementary map at 2.25 eV). The laser-on EEL point spectrum is similar to the laser-off spectrum except a small sEEL peak and sEEG peak emerges at ±1.58 eV, respectively. The laser-on EELS map is shown in **Figure 4.2** for -1.58 (d) and +1.58 eV (e). Clearly, the sEEG and sEEL peaks have the signature dipolar characteristics and thus the photons are resonantly coupling to the dipole or $m = 1$ LSPR mode.

The 150 nm vertical nanorod is oriented such that the long axis has a component parallel to the photon propagation direction thus both s- and p-polarized light couples with the long axis dipole that that is resonant with the laser energy. The EEL point spectra for the laser-on and laser-off condition of the vertical nanorod are plotted in **Figure 4.2f** for the aloof position in **Figure 4.2g**. The dipole resonance of this nanorod is ~ 1.53 eV and the higher order modes at 2.43 eV. **Figure 4.2h** shows the 1.53 eV EELS map. For the laser-on spectrum, the photon-plasmon coupling is again evidenced via the emergence of the sEEL and sEEG peaks at ±1.58 eV. **Figure 4.2** shows the laser-on maps of the sEEL (i) and sEEG (j) peaks. As will be discussed below, the tilted orientation slightly decreases the spontaneous EELS intensity and the s-polarized component of the polarized light that is aligned with the long axis is reduced due to the orientation; thus the sEEL/sEEG intensity is reduced relative to the horizontal orientation[206].

The $m = 2$ mode is interrogated using longer nanorods of ~310 (vertical) and 330 nm (horizontal) in length. In contrast to optical techniques, an electron beam is capable of exciting all plasmonic modes, thus we expect to observe an EEL signature related to the $m = 2$ mode. However, the sEEG and sEEL signatures are produced by synergistic electron and optical coupling and because this mode is optically dark, no sEEL and sEEG peaks should appear. However, as will be shown, appropriate orientations induce retardation

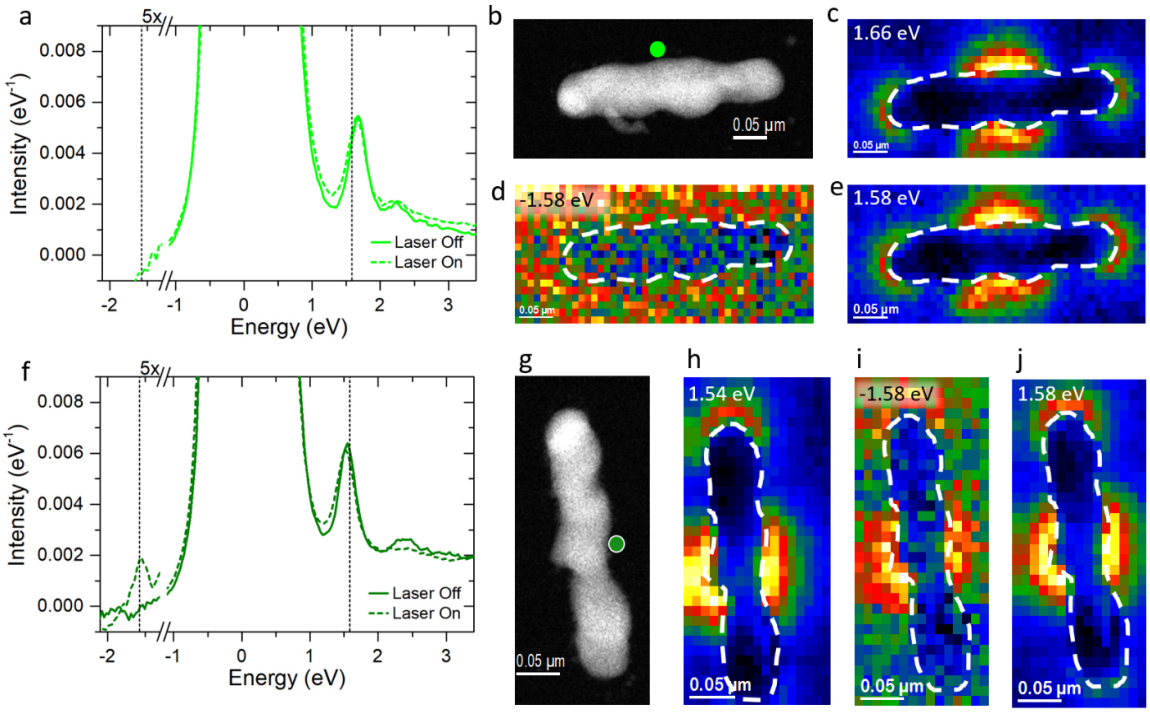

Figure 4.3. (a) Horizontal nanorod aloof 6-pixel map spectra average with laser off and on. Dashed lines in a and f correspond to the laser energy at ±1.58 eV (b) HAADF image of horizontal nanorod with aloof position indicated by green circle. (c-e) Horizontal nanorod maps of EEL, sEEG, and sEEL peak intensities, respectively. (f) Vertical nanorod aloof 6-pixel map spectra average with laser off and on. (g) HAADF image of vertical nanorod with aloof position indicated by green circle. (h-j) Vertical nanorod maps of EEL, sEEG, and sEEL peak intensities, respectively.

effects[198,207,208], which enhance the far field photon coupling and the emergence of resonant sEEL and sEEG peaks.

Figure 4.3a displays the EEL point spectra of the ~330 nm horizontal long nanorod collected at the long axis center aloof position with and without concurrent laser irradiation (**Figure 4.3b**). The laser-off spectrum has peaks at 1.66 eV and at 2.35 eV, which are attributed to the m = 2 mode and the higher order modes, respectively. The laser-off 1.66 eV EELS map is shown in **Figure 4.3c**, which reveals the expected peak intensity on each nanorod end and in the nanorod center, where the loss probability is the highest. Additionally, the ZLP appears narrower when taken at the nanorod center than the spectra collected at the nanorod ends because the low-energy dipole resonance broadens the ZLP (**Figure A.4.2**). The laser-on EEL point spectrum is very similar to the laser-off EELS spectrum. The ZLP is slightly broadened due to photothermal heating, however, no sEEL or sEEG peaks are observed at ±1.58 eV, respectively. **Figure 4.3d** shows the EELS map for -1.58 eV, which does not contain the signature of the m = 2 pattern. **Figure 4.3e** shows the EELS map for +1.58 eV, which demonstrates the m = 2 mode, however this is due to the spontaneous EEL and not sEEL. Thus, clearly there is no optical coupling observed.

The 310 nm m = 2 vertical nanorod EEL point spectra for the laser-off and laser-on conditions are plotted in **Figure 4.3f** for the center aloof position (**Figure 4.3g**). The m = 2 resonance for this nanorod occurs at 1.54 eV and the higher order modes are 2.46 eV. **Figure 4.3h** shows the 1.54 eV EELS map, where unexpectedly the mode signature is more intense at the top of the nanorod relative to the bottom. As expected, due to retardation effects, the laser-on spectrum clearly possesses the sEEG peak at -1.58 eV. **Figure 4.3i** and **j** show the sEEG and sEEL maps, which clearly exhibit the characteristic m = 2 intensity profile. The selection rules for optical coupling are relaxed due to the geometry of our experiment. It is known that optically dark modes can be excited by using an oblique angle of incidence of light, which introduces phase retardation across a structure[198,207,208]. When the long axis of the nanorod is oriented with a component parallel to the photon propagation axis (p-polarization), as it is for our vertical orientation, retardation effects are induced where the strength of the electric field is non-uniform along the nanorod long axis, thus

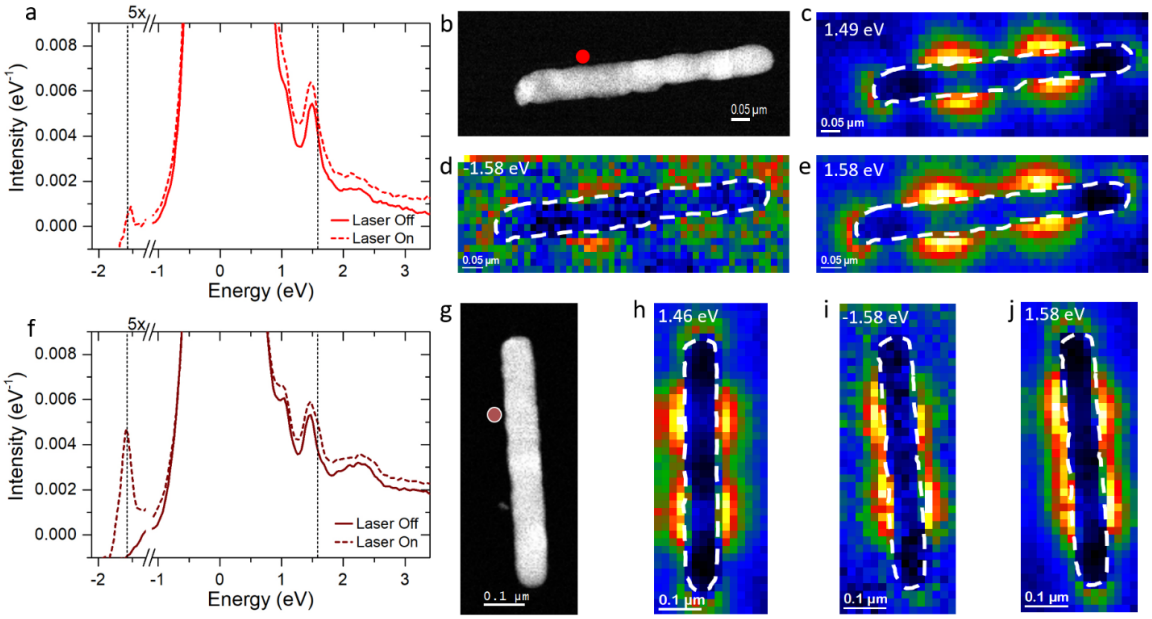

Figure 4.4. (a) Horizontal nanorod aloof 6-pixel map spectra average with laser off and on. Dashed lines in a and f correspond to the laser energy at ±1.58 eV. (b) HAADF image of horizontal nanorod with aloof position indicated by red circle. (c-e) Horizontal nanorod maps of EEL, sEEG, and sEEL peak intensities, respectively. (f) Vertical nanorod aloof 6-pixel map spectra average with laser on. (g) HAADF image of vertical nanorod with aloof position indicated by red circle. (h-j) Vertical nanorod maps of EEL, sEEG, and sEEL peak intensities, respectively.

allowing for optical excitation of the m = 2 mode[206]. In the case of the horizontal nanorod, the long axis is perpendicular to the light propagation, resulting in no phase retardation, and the m = 2 resonance sEEL and sEEG peaks are not observed.

The m = 3 mode is probed to investigate coupling to higher order bright modes. **Figure 4.4a** displays the EEL point spectra of the ~ 670 nm horizontal nanorod collected at an aloof position 1/3 the length of the nanorod (**Figure 4.4b**) where the m = 3 mode is expected to have the strongest resonance. The laser-off spectrum shows a resonance at 1.49 eV and the 1.49 eV EELS map is shown in **Figure 4.4c**, which clearly demonstrates the EELS intensity peaks at the 1/3 and 2/3 rod length positions associated with the m = 3 mode.

Additionally, the m = 2 mode is observed as a shoulder to the ZLP. The laser-on point spectrum shows the characteristic sEEL and sEEG peaks at ±1.58 eV. **Figure 4.4d** and **e** show the EELS maps for the sEEG and sEEL energies, which also clearly have the characteristic m = 3 nodal pattern, demonstrating resonant coupling to the m = 3 mode.

The 660 nm vertical nanorod point EEL spectra are shown in **Figure 4.4f** for the aloof position indicated in **Figure 4.4g**. Here, we see a peak at 1.46 eV which is attributed to the m = 3 mode as evidenced by the EELS map in **Figure 4.4h**. The laser-on point spectrum shows the characteristic sEEL and sEEG peaks at ±1.58 eV. The EELS maps for the sEEG and sEEL energies are shown in **Figure 4.4i** and **j**, which demonstrate the m = 3 pattern.

4.2.5. Discussion

Several approaches have been developed to model photon stimulated EEL and EEG phenomena[65,66,71–73,79]. As has been demonstrated previously[66], sEELS and sEEGS is proportional to the product of the optical extinction cross section (σ) and the spontaneous EELS intensity (Γ_{EELS}). Thus it is instructive to compare the resultant EEL and extinction spectra for the geometries studied. We performed discrete-dipole approximation (DDA)[209,210] and electron-driven DDA (e-DDA)[211,212] simulations of the different nanorod lengths. **Figure 4.5** shows DDA electric field maps (**c, e, g, i, k**) and EELS maps (**d, f, h, j, l, m**) for the m = 1 (**c-f**), m = 2 (**g, h, m**) and m = 3 (**i-l**) of the two nanorod orientations. **Figure 4.5a** and **b** are the simulated extinction and EEL spectra, taken at a 9 nm impact

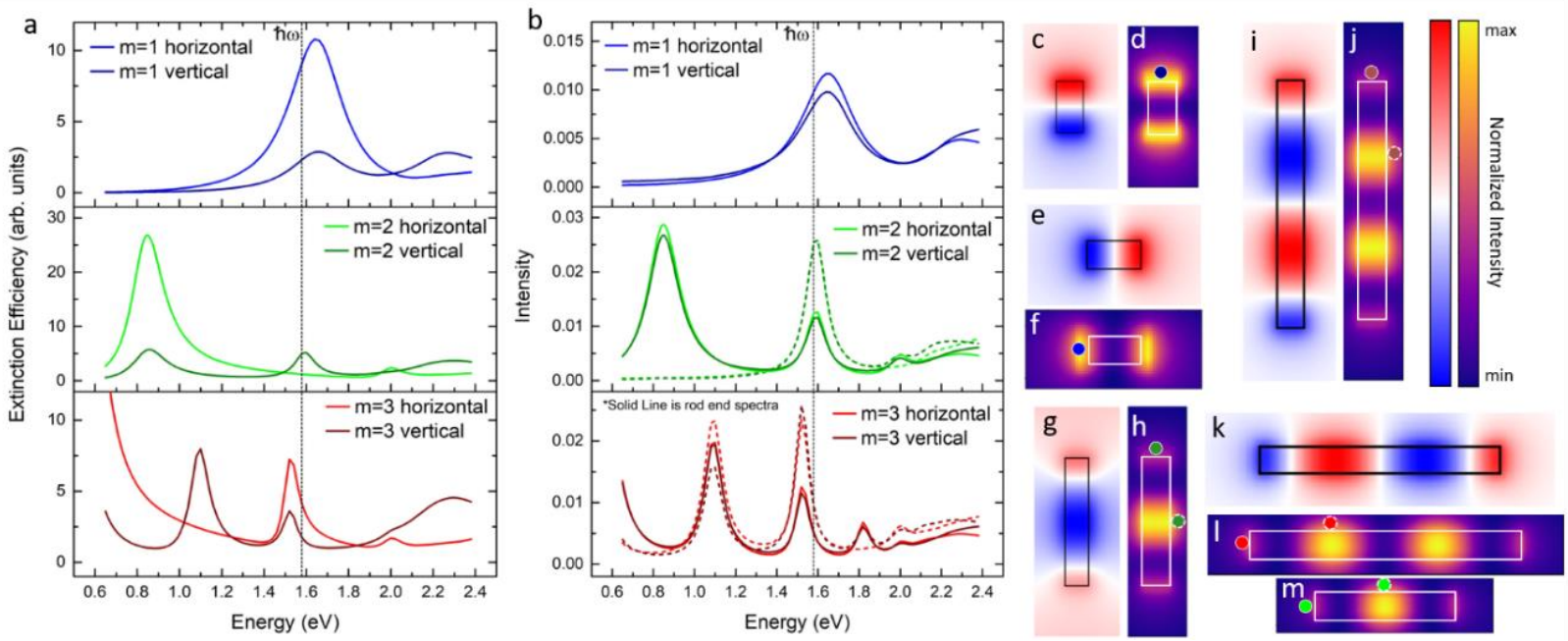

Figure 4.5. Simulated DDA (a) and e-DDA (b) spectra for horizontal and vertical rod orientations where the EELS are taken at a common 9 nm impact position relative to the nanorod end. Positions indicated in e-DDA maps by color coded circles with solid white boarder for spectra taken at the end of the nanorod and with a dashed white boarder for spectra taken at the EELS intensity maximum for m=2, 3. Normalized DDA (c, e, g, i, k, m) and e-DDA (d, f, h, j, l) electric field maps for the m = 1 (c-f), m = 2 (g, h ,m), and m = 3 (i-l) modes of the two nanorod orientations for the experimental geometries.

parameter at the intensity maximum in the EELS map for each rod (see simulated EELS maps for spectral positions). As illustrated in **Figure 4.1**, the electron beam trajectory is 30° and the photon wave vector is 60° relative to the nanorod normal.

Before overviewing the sEEGS results, it is worth noting a few general observations of the EEL and extinction spectra for the two orientations (**Figure A.4.3.**). First, regarding the EEL spectra, note that the tilted substrate slightly decreases the Γ_{EELS} for the end position in the vertical orientation, whereas it has a negligible effect on the horizontal orientation. Additionally, when the long nanorod axis is in the vertical orientation, the component of the electric field polarization that couples with the long axis is decreased due to the tilt by $\sin^2(30^\circ)$ or 25%; the horizontal orientation, however, is constant. With these generalizations, we expect that for the odd bright modes (m = 1 and 3), the sEEG of the horizontal orientations should be more intense as both the electric field and Γ_{EELS} are higher. Interestingly, for the m = 3 mode the Γ_{EELS} is ~ 2x higher than the m = 1 mode, but the optical extinction is ~ 2x lower so the sEEG intensity should be comparable.

As noted previously[73] and confirmed in our previous work[66], the sEELS and sEEGS peaks have nearly the same amplitude and thus while the sEEL peaks are convolved with the LSPR peaks, we can unambiguously fit the sEEG peaks and thus de-convolve the sEEL and LSPR peaks (**4.2.7.1 Supporting Information**). Furthermore, Das et al.[79] showed that the light-driven population of the plasmon mode (M_x^{max}) can be estimated by $M_x^{max} = \left[\left(\frac{\Gamma_{EEL}+\Gamma_{sEEL}}{\Gamma_{sEEG}}\right) - 1\right]^{-1}$; where Γ_{EEL}, Γ_{sEEL}, and Γ_{sEEG}, are the integrated peak intensities of spontaneous EELS and the associated sEEL and sEEG peaks of the SPP mode of interest. **Table 4.2** summarizes the M_x^{max} numbers estimated from the peak fits of the spectra taken at the spontaneous EELS intensity maximum positions for each mode. Note that while higher light-driven plasmon populations are realized in high-irradiance pulsed experiments[79], the values realized here are consistent with previous low irradiance cw experiments[66].

Table 4.2. Light driven plasmon populations (M_x^{max}).

	Horizontal	**Vertical**
***m* = 1**	6.1×10^{-2}	1.7×10^{-2}
***m* = 2**	-	6.3×10^{-2}
***m* = 3**	7.3×10^{-2}	1.63×10^{-1}

Empirically, the light-driven population is proportional to the laser irradiance and the extinction coefficient at the laser energy. Assuming the laser irradiance is constant, one can compare the experimental M_x^{max} values to the calculated extinction coefficients of the different modes and orientations. As expected, the horizontal m = 1 plasmon occupation stimulated by the laser is 3.6x the vertical nanorod in excellent agreement with the 4x reduction expected from the reduced electric field for the vertical orientation. Interestingly, light-driven plasmon population for the horizontal m = 3 is slightly higher than the m = 1, though one expects that the optical coupling to the m = 1 mode would be ~ 2x that of the m = 3 value. Even more surprisingly, the vertical m = 3 light driven plasmon population has the highest value, which is > 2x greater than the m = 1 horizontal dipole, which has a simulated extinction cross section 5x smaller. Small variations in the alignment of the Gaussian laser profile, variations in the impact parameters, and perhaps geometric asymmetries present in the nanorod could be contributing factors to some of the quantitative inconsistencies. We note that the m = 3 rods are the most regular patterns and have much less roughness, which could enhance the dephasing time relative to the m = 1,2 modes.

For the m = 2 dark mode in the horizontal orientation, the extinction cross section is near zero and thus no optical coupling or sEEG is observed. For the vertical orientation, however, the mixed s- and p-polarization induces retardation effects, which increases the extinction cross section and thus the sEEG peak emerges. While the simulated extinction cross section ratio m=2(vertical)/m=1(horizontal) is ~ 0.5, the experimental light driven

plasmon population ratio is ~ 1. Similarly, the simulated extinction cross section *m*=2(vertical)/*m*=1(vertical) is ~ 2.1 and the experimental light driven plasmon population ratio is 3.7. Interestingly, there is a competition in the extinction cross section for the *m* = 2 mode as a function of the sample tilt angle; starting at $\theta=90^{o}$ and as $\theta \rightarrow 0$, retardation enhances the extinction cross section, however the electric field decreases. The result is that the extinction efficiency for this mode is a maximum at 45°. Thus, a judicious use of laser orientation and/or substrate tilt can be used to promote sEEGS as a unique tool to observe the near field of optically excited materials.

4.2.6. Conclusions

We have shown that continuous wave (cw) photon stimulated electron energy loss and gain spectroscopy can be used to image the near field of optically stimulated LSPR modes in nanorod antennas. The sEEL and sEEG peaks are generated by an optical delivery system mounted on a (S)TEM microscope. The LSPR *m* = 1, 2, and 3 modes are tuned to the laser energy by varying the nanorod length. The optically stimulated near field spectra and images of these modes are measured at various nanorod orientations to explore how the electric field and retardation affect the resonant sEEG. By fitting the spectra and obtaining the integrated peak intensities of spontaneous EEL and the associated sEEL and sEEG peaks, we estimated the light-driven population of the plasmon mode for each nanorod. DDA and e-DDA simulations of the extinction coefficients and EEL probabilities, respectively, are used to rationalize the observed data. As expected, the odd modes are optically bright and thus sEEG peaks are observed. The *m* = 2 dark mode promotes sEEG only when oriented vertically and tilted such that mixed s- and p-polarization induced retardation effects are operative and thus increase the extinction coefficient of this mode. Thus, we demonstrate cw sEEGS as an effective tool in imaging the near field of optically driven plasmon modes.

4.2.7. Appendix

4.2.7.1. Supporting Information

In order to quantify the number of plasmons, we fit the unprocessed experimental spectra. An example of the fitting for the *m*=1 horizontal rod is shown in **Figure A.4.4**. We employ the built-in *Matlab* algorithm, *fmincon*, using the chi-squared distribution function as the objective function to find the best fit. Prior to fitting, the origin was determined by fitting zero-loss peak to a Gaussian function and shifted the peak to zero eV to ensure the exact positions of peaks in the spectrum. The intensity of each spectrum was normalized by the integrated sum. The zero-loss peak was fit with a gaussian and two exponential tails, one on the positive and one on the negative energy side of the zero-loss peak. Upon subtraction of the zero-loss peak, four Gaussian peaks were used to model the Si_3N_4 substrate, and the remaining peaks were fit using Lorentzian peaks. The whole spectrum was fit using the minimum number of peaks required for a good fit.

Fitting parameters for the substrate and five rods are shown in **Table A.4.3-Table A.4.8**. A spectrum acquired far from any resonant structures was used to first fit the substrate signal. The large broad peak around 22 eV is from the bulk plasmon of the Si_3N_4 substrate, which was best represented by four Gaussian peaks (**Table A.4.2.**). The parameters found for these four peaks were allowed to change by 10% for subsequent fitting of spectra acquired for resonant structures. Extra peaks are seen around the zero-loss as was previously reported[66]. The laser off spectrum was first fit using the minimum number of peaks. To fit the laser on spectrum, two identical peaks were added for the sEEG (-1.58 eV) and sEEL (1.58 eV). The sEEG/sEEL peaks were set to have the same half-width-at-half-maximum (HWHM) as the zero-loss peak and the amplitude was unrestricted. The plasmon peak (*m*=1,2,3) amplitudes were restricted to be within 10% of the laser off spectrum since the addition of the sEEL peak allows for multiple representations of this area of the spectrum. The additional peaks from the laser off spectrum were used as initial conditions where the position and HWHM were allowed to vary by 10% and the amplitude was unrestricted. The resultant peak fitting parameters are listed in the tables below.

4.2.7.2. Figures

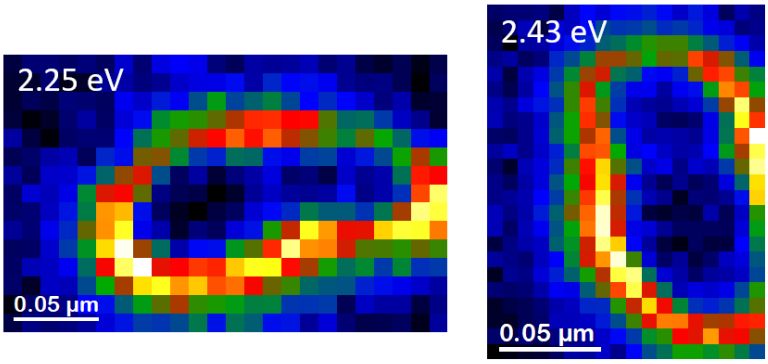

Figure A.4.1. Maps of the higher order modes for horizontal and vertical rods from m=1 length rods.

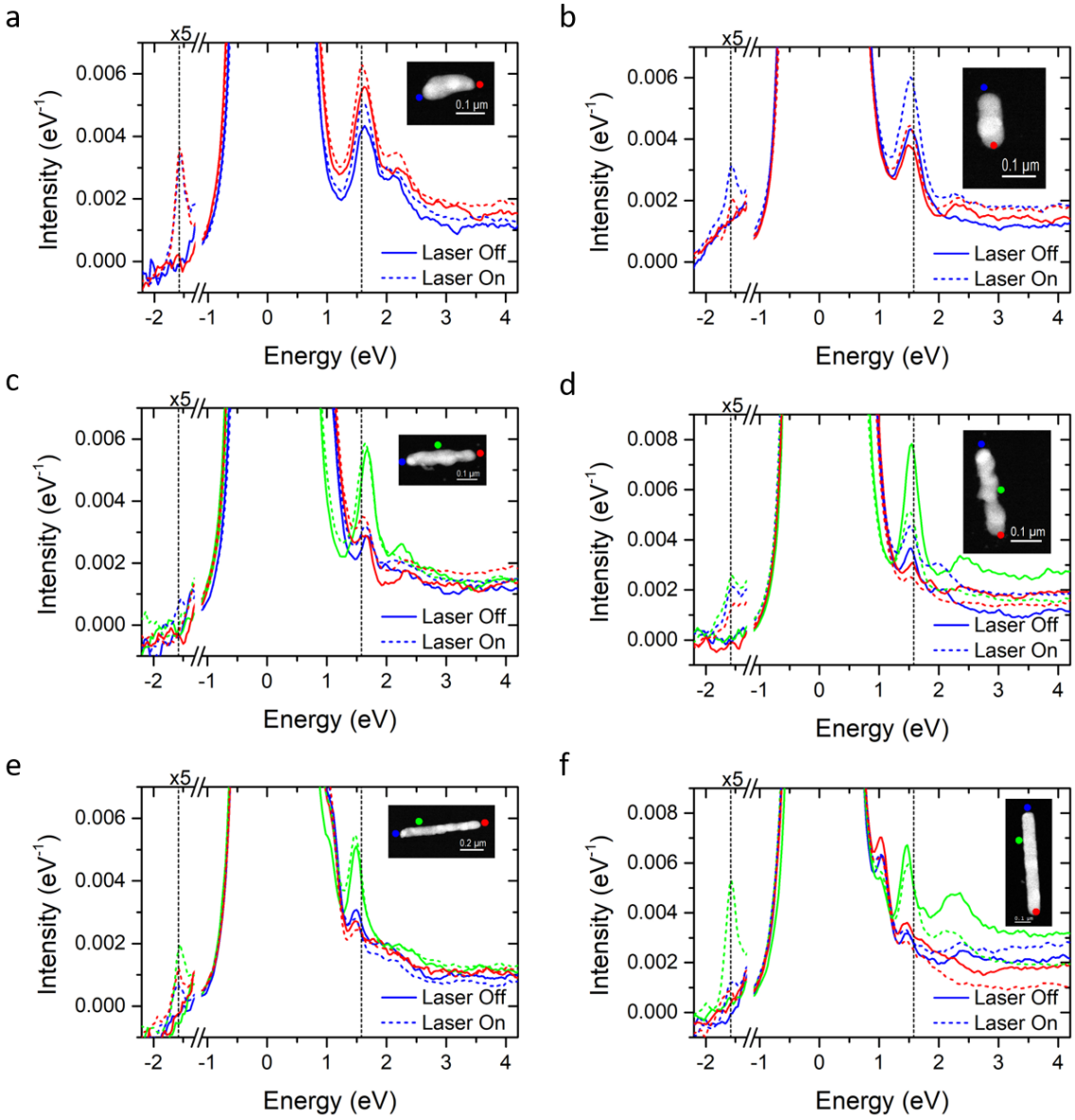

Figure A.4.2. Point spectra for laser off and laser on conditions for (a) horizontal m=1 mode rods, (b) vertical m=1 rods, (c) horizontal m=2 rods, (d) vertical m=2 rods, (e) horizontal m=3 rods, (f) vertical m=3 rods with HAADF images and aloof positions show in the inset.

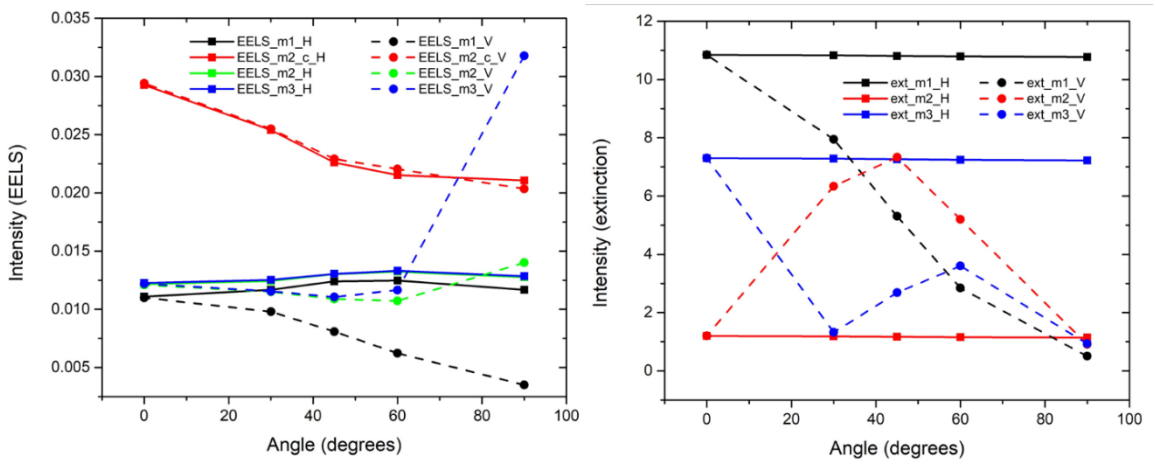

Figure A.4.3. a) e-DDA spectra for different electron/substrate angles and b) DDA spectra for different wave-vector/substrate angles. Summary of the simulated peak intensities versus angle for the c) e-DDA and d) DDA.

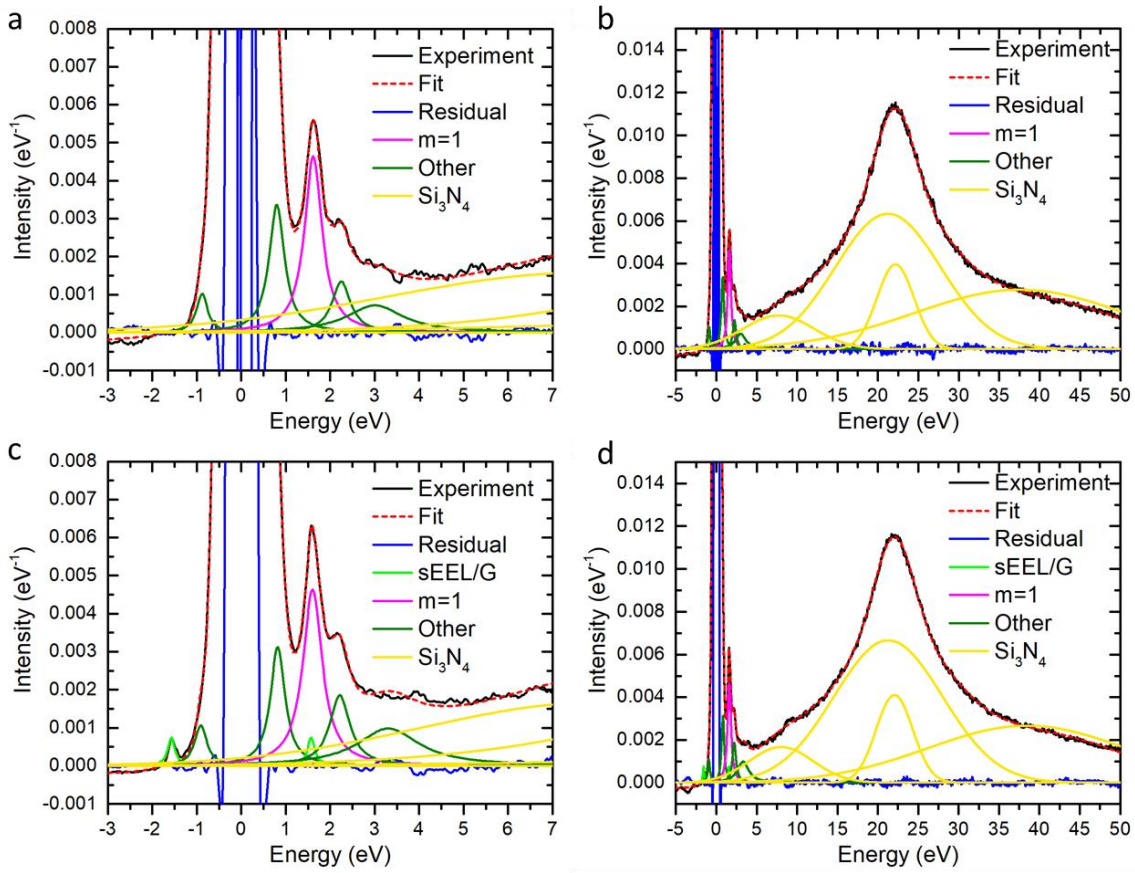

Figure A.4.4. Representative fits for horizontal m=1 rod for laser off (a-b) and laser on (c-d) spectra.

4.2.7.3. Tables

Table A.4.1 Point spectra collection parameters.

	Left/Top		Center		Right/Bottom	
	Frames	**Exposure**	**Frames**	**Exposure**	**Frames**	**Exposure**
M1 $_{H, On}$	10	0.05	-	-	10	0.05
M1 $_{H, Off}$	5	0.05	-	-	5	0.05
M1 $_{V, On}$	5	0.06	-	-	10	0.06
M1 $_{V, Off}$	5	0.065	-	-	5	0.065
M2 $_{H, On}$	10	0.05	10	0.05	10	0.05
M2 $_{H, Off}$	5	0.05	5	0.05	5	0.05
M2 $_{V, On}$	10	0.065	6	0.065	10	0.065
M2 $_{V, Off}$	6	0.06	5	0.06	7	0.06
M3 $_{H, On}$	10	0.05	10	0.05	10	0.05
M3 $_{H, Off}$	5	0.05	5	0.05	5	0.05
M3 $_{V, On}$	5	0.06	5	0.06	5	0.06
M3 $_{V, Off}$	5	0.06	5	0.06	5	0.06

Table A.4.2. Fitting parameters for Si_3N_4 substrate.

	Laser Off		
	Amplitude (eV^{-1})	**Center (eV)**	**HWHM (eV)**
Substrate	0.00564	21.436	7.520
Substrate	0.00423	22.035	2.821
Substrate	0.00276	36.305	17.201
Substrate	0.00110	9.616	4.804

Table A.4.3. Fitting parameters for horizontal m=1 rod for laser off and laser on spectra.

	Laser Off			Laser On		
	Amplitude (eV^{-1})	**Center (eV)**	**HWHM (eV)**	**Amplitude (eV^{-1})**	**Center (eV)**	**HWHM (eV)**
sEEG	-	-	-	0.00075	-1.572	0.099
Thermal	0.00102	-0.880	0.151	0.00106	-0.910	0.165
Thermal	0.00337	0.805	0.212	0.00313	0.821	0.198
sEEL	-	-	-	0.00075	1.573	0.099
m=1	0.00464	1.623	0.242	0.00464	1.605	0.264
Higher Order	0.00135	2.254	0.255	0.00186	2.217	0.275
	0.00072	3.011	0.770	0.00098	3.311	0.847
Substrate	0.00634	21.227	7.650	0.00666	21.283	7.905
Substrate	0.00396	22.158	2.688	0.00410	22.062	2.680
Substrate	0.00278	37.548	15.397	0.00266	38.447	14.407
Substrate	0.00158	7.707	5.156	0.00167	8.029	4.644

Table A.4.4. Fitting parameters for vertical m=1 rod for laser off and laser on spectra.

	Laser Off			Laser On		
	Amplitude (eV^{-1})	**Center (eV)**	**HWHM (eV)**	**Amplitude (eV^{-1})**	**Center (eV)**	**HWHM (eV)**
sEEG	-	-	-	0.00019	-1.572	0.093
Thermal	0.00050	-1.018	0.168	0.00092	-0.918	0.176
Thermal	0.00254	0.850	0.253	0.00249	0.844	0.225
sEEL	-	-	-	0.00019	1.588	0.093
m=1	0.00334	1.532	0.234	0.00464	1.512	0.214
Higher Order	0.00037	2.433	0.781	0.00073	2.603	0.826
Substrate	0.00647	21.316	7.548	0.00687	21.051	8.022
Substrate	0.00390	22.048	2.675	0.00397	21.994	2.763
Substrate	0.00255	37.576	14.591	0.00246	38.473	13.499
Substrate	0.00136	8.045	5.080	0.00157	7.367	4.572

Table A.4.5. Fitting parameters for horizontal m=2 rod for laser off and laser on spectra.

	Laser Off			Laser On		
	Amplitude (eV^{-1})	**Center (eV)**	**HWHM (eV)**	**Amplitude (eV^{-1})**	**Center (eV)**	**HWHM (eV)**
sEEG	-	-	-	-	-	-
Thermal	0.00130	-0.904	0.159	0.00108	-0.893	0.175
Thermal	0.00279	0.853	0.214	0.00260	0.858	0.235
sEEL	-	-	-	-	-	-
m=2	0.00464	1.660	0.177	0.00491	1.651	0.194
Higher Order	0.00145	2.349	0.416	0.00097	2.376	0.445
	0.00025	4.217	1.078	0.00035	3.795	0.970
Substrate	0.00713	21.200	8.495	0.00681	21.259	8.515
Substrate	0.00445	22.208	2.767	0.00439	22.075	2.757
Substrate	0.00304	39.864	14.238	0.00259	39.702	13.818
Substrate	0.00121	6.600	4.248	0.00118	7.260	4.367

Table A.4.6. Fitting parameters for vertical m=2 rod for laser off and laser on spectra.

	Laser Off			Laser On		
	Amplitude (eV^{-1})	**Center (eV)**	**HWHM (eV)**	**Amplitude (eV^{-1})**	**Center (eV)**	**HWHM (eV)**
sEEG	-	-	-	0.00037	-1.572	0.115
Thermal	0.00072	-0.830	0.103	0.00101	-0.906	0.110
Thermal	0.00130	0.882	0.232	0.00319	0.837	0.253
sEEL	-	-	-	0.00037	1.588	0.115
m=2	0.00665	1.540	0.165	0.00387	1.501	0.176
Higher Order	0.00191	2.464	0.382	0.00105	2.315	0.418
	0.00097	4.212	1.155	0.00046	3.789	1.041
Substrate	0.00726	20.702	8.420	0.00660	21.052	8.178
Substrate	0.00391	22.169	2.624	0.00408	21.992	2.812
Substrate	0.00283	38.622	13.930	0.00237	38.811	13.327
Substrate	0.00193	6.945	3.880	0.00137	7.645	4.268

Table A.4.7. Fitting parameters for horizontal m=3 rod for laser off and laser on spectra.

	Laser Off			Laser On		
	Amplitude (eV^{-1})	**Center (eV)**	**HWHM (eV)**	**Amplitude (eV^{-1})**	**Center (eV)**	**HWHM (eV)**
sEEG	-	-	-	0.00044	-1.572	0.112
Thermal	0.00139	-0.773	0.193	0.00145	-0.758	0.202
Thermal	0.00145	1.108	0.107	0.00273	1.090	0.107
sEEL	-	-	-	0.00044	1.572	0.112
m=3	0.00400	1.493	0.153	0.00408	1.472	0.165
Higher Order	0.00145	2.170	0.574	0.00132	2.243	0.615
	0.00036	4.291	1.270	0.00052	3.942	1.143
Substrate	0.00669	21.386	7.663	0.00642	21.370	7.957
Substrate	0.00397	22.099	2.669	0.00415	21.999	2.768
Substrate	0.00273	38.352	14.151	0.00256	38.581	14.311
Substrate	0.00142	8.332	4.861	0.00139	8.562	4.469

Table A.4.8. Fitting parameters for vertical m=3 rod for laser off and laser on spectra.

	Laser Off			Laser On		
	Amplitude (eV^{-1})	**Center (eV)**	**HWHM (eV)**	**Amplitude (eV^{-1})**	**Center (eV)**	**HWHM (eV)**
sEEG	-	-	-	0.00091	-1.572	0.078
Thermal	0.00199	-0.693	0.160	0.00262	-0.702	0.176
Thermal	0.00651	0.616	0.147	0.00519	0.610	0.159
m=2	0.00288	1.031	0.191	0.00359	1.001	0.210
m=3	0.00429	1.457	0.115	0.00343	1.460	0.126
sEEL	-	-	-	0.00091	1.572	0.078
m=4	0.00091	1.723	0.181	0.00084	1.681	0.199
Higher Order	0.00337	2.322	0.533	0.00220	2.244	0.492
	0.00166	4.358	1.198	0.00085	3.986	1.083
SiN	0.00189	7.789	3.916	0.00138	7.958	4.148
SiN	0.00849	21.047	8.227	0.00674	21.557	8.264
SiN	0.00378	22.476	2.676	0.00411	22.370	2.901
SiN	0.00350	39.559	14.665	0.00262	39.786	14.249

Chapter 5

Conclusions

In this dissertation, the study of two binary metallic systems is presented with the goal of realizing novel plasmonic material through correlating the atomic composition and crystallographic phases with the dielectric function. Additionally, progress is made using a new tool to image the optically stimulated near field of lithographically patterned nanostructures.

In Chapter 2, we have studied the Au-Al bimetallic system. The efficacy of this material system is inhibited by the formation of intermetallic compounds through much of the compositional space. Two interesting regions of the phase diagram included the mixed Al-$AuAl_2$ region and the solid solution of Al in Au. The solid solution of Al in Au occurred with an atomic composition of >90% Au. Optically, the solid solution alloy presented an increase in the imaginary component of the dielectric function with increasing Al content. Otherwise, the alloy behaved similarly to pure Au. The mixed Au-$AuAl_2$ region dielectric function demonstrated tunability by varying the relative amounts of Al and $AuAl_2$ in the sample.

In Chapter 3, we studied the Au-Ni bimetallic system. This material system exhibits a large miscibility gap which spans the entire compositional space. As deposited films exhibited a supersaturated solid solution across the entire compositional range and consequently, the dielectric function displayed a smooth transition between pure Au and pure Ni. We developed an analytical model the to describe the changes in the dielectric function which may be used to approximate the dielectric function of other Au-Ni alloys not explicitly measured. Annealed films exhibited phase separation into Au-rich and Ni-rich grains. The composition of the individual grains and the dielectric function depended on the annealing temperature. The analytical model was then used to calculate the dielectric function of the individual Au-rich and Ni-rich grains. The dielectric function of the phase separated film was approximated using a compositional weighted average of the calculated Au-rich and Ni-rich dielectric functions. The calculations agreed well with experimental results. The

effect of annealing temperature on the dielectric function was studied for a single composition and it was found that there was a tradeoff between grain size and composition. In Chapter 4, we demonstrated the capability of a (S)TEM equipped with an optical laser delivery system to image the plasmon near field of optically stimulated nanostructures. By varying the length of the Au nanorods, we tuned the plasmonic response such that the m = 1, 2, and 3 modes occurred near the laser energy. Retardation effects were operative in vertically oriented rods which relaxed the selection rules which usually made even parity modes optically dark. By fitting the spectra to obtain sEEL and sEEG peak intensities, we estimated the light-driven population of the plasmon mode for each nanorod. Simulations of the EEL probabilities and extinction coefficients were used to rationalize the data, particularly why the even parity mode was able to be optically stimulated.

While there will never be a single material perfectly suitable for all plasmonic applications, it is important to add to the existing library of materials, carefully noting the strengths and weaknesses of a material. While materials alternative to Ag and Au will not have the same low loss characteristic, it is possible that they will have alternative interesting properties such as high temperature stability, low cost, phase-changing capabilities, and so on. Alternative materials such as refractory metals, nitrides, and oxides have been of recent interest, however more work is needed to contribute to the ever-growing library of unusual plasmonic materials. In the area of imaging the nearfield of optically stimulated nanostructures, we have made progress demonstrating the capability of the tool to do this using a continuous current electron beam and a continuous wave laser. More work is needed in this area to fully understand asymmetries in the optically stimulated nearfield as well as the coupling strength for higher order plasmonic modes.

LIST OF REFERENCES

(1) Maier, S. A.; Brongersma, M. L.; Kik, P. G.; Meltzer, S.; Requicha, A. A. G.; Atwater, H. A. Plasmonics—A Route to Nanoscale Optical Devices. *Adv. Mater.* **2001**, *13* (19), 1501–1505.

(2) Vincenzo, A.; Roberto, P.; Marco, F.; Onofrio, M. M.; Maria Antonia, I. Surface plasmon resonance in gold nanoparticles: a review. *J. Phys. Condens. Matter* **2017**, *29* (20), 203002.

(3) Göeken, K. L.; Subramaniam, V.; Gill, R. Enhancing spectral shifts of plasmon-coupled noble metal nanoparticles for sensing applications. *Phys. Chem. Chem. Phys.* **2015**, *17* (1), 422–427.

(4) Han, P.; Martens, W.; Waclawik, E. R.; Sarina, S.; Zhu, H. Metal Nanoparticle Photocatalysts: Synthesis, Characterization, and Application. 2018, bl n/a-n/a.

(5) Atwater, H. A.; Polman, A. Plasmonics for improved photovoltaic devices. *Nat. Mater.* **2010**, *9* (3), 205–213.

(6) Abadeer, N. S.; Murphy, C. J. Recent Progress in Cancer Thermal Therapy Using Gold Nanoparticles. *J. Phys. Chem. C* **2016**, *120* (9), 4691–4716.

(7) Haffner, C.; Chelladurai, D.; Fedoryshyn, Y.; Josten, A.; Baeuerle, B.; Heni, W.; Watanabe, T.; Cui, T.; Cheng, B.; Saha, S.; et al. Low-loss plasmon-assisted electro-optic modulator. *Nature* **2018**, *556* (7702), 483–486.

(8) Maier, S. A. *Plasmonics: Fundamentals and Applications*; Springer US: New York, NY: New York, NY, 2007.

(9) Barnes, W. L. Particle plasmons: Why shape matters. *Am. J. Phys.* **2016**, *84* (8), 593–601.

(10) Zayats, A. V; Smolyaninov, I. I. Near-field photonics: surface plasmon polaritons and localized surface plasmons. *J. Opt. A Pure Appl. Opt.* **2003**, *5* (4), S16–S50.

(11) West, P. R.; Ishii, S.; Naik, G. V; Emani, N. K.; Shalaev, V. M.; Boltasseva, A. Searching for better plasmonic materials. *Laser Photon. Rev.* **2010**, *4* (6), 795–808.

(12) Koh, A. L.; Fernández-Domínguez, A. I.; McComb, D. W.; Maier, S. A.; Yang, J. K. W. High-Resolution Mapping of Electron-Beam-Excited Plasmon Modes in Lithographically Defined Gold Nanostructures. *Nano Lett.* **2011**, *11* (3), 1323–1330.

(13) Gong, C.; Leite, M. S. Noble Metal Alloys for Plasmonics. *ACS Photonics* **2016**, *3* (4), 507–513.

(14) Polyanskiy, M. N. Refractive index database https://refractiveindex.info.

(15) Oates, T. W. H.; Wormeester, H.; Arwin, H. Characterization of plasmonic effects in thin films and metamaterials using spectroscopic ellipsometry. *Prog. Surf. Sci.* **2011**, *86* (11), 328–376.

(16) Doiron, B.; Mota, M.; Wells, M. P.; Bower, R.; Mihai, A.; Li, Y.; Cohen, L. F.; Alford, N. M.; Petrov, P. K.; Oulton, R. F.; et al. Quantifying Figures of Merit for Localized Surface Plasmon Resonance Applications: A Materials Survey. *ACS Photonics* **2019**, *6* (2), 240–259.

(17) Etchegoin, P. G.; Le Ru, E. C.; Meyer, M. An analytic model for the optical properties of gold. *J. Chem. Phys.* **2006**, *125* (16), 164705.

(18) Rioux, D.; Vallières, S.; Besner, S.; Muñoz, P.; Mazur, E.; Meunier, M. An Analytic Model for the Dielectric Function of Au, Ag, and their Alloys. *Adv. Opt. Mater.* **2014**, *2* (2), 176–182.

(19) Peña-Rodríguez, O. Modelling the dielectric function of Au-Ag alloys. *J. Alloys Compd.* **2017**, *694*, 857–863.

(20) Fan, X.; Zheng, W.; Singh, D. J. Light scattering and surface plasmons on small spherical particles. *Light Sci. &Amp; Appl.* **2014**, *3*, e179.

(21) Toudert, J.; Serna, R. Interband transitions in semi-metals, semiconductors, and topological insulators: a new driving force for plasmonics and nanophotonics [Invited]. *Opt. Mater. Express* **2017**, *7* (7), 2299–2325.

(22) Yao, G.-Y.; Liu, Q.-L.; Zhao, Z.-Y. Studied Localized Surface Plasmon Resonance Effects of Au Nanoparticles on TiO2 by FDTD Simulations. *Catalysts* . 2018.

(23) Kelly, K. L.; Coronado, E.; Zhao, L. L.; Schatz, G. C. The Optical Properties of Metal Nanoparticles: The Influence of Size, Shape, and Dielectric Environment. *J. Phys. Chem. B* **2003**, *107* (3), 668–677.

(24) Johnson, P. B.; Christy, R. W. Optical Constants of the Noble Metals. *Phys. Rev. B* **1972**, *6* (12), 4370–4379.

(25) Linic, S.; Christopher, P.; Ingram, D. B. Plasmonic-metal nanostructures for efficient conversion of solar to chemical energy. *Nat. Mater.* **2011**, *10*, 911.

(26) Ma, W. Y.; Yang, H.; Hilton, J. P.; Lin, Q.; Liu, J. Y.; Huang, L. X.; Yao, J. A numerical investigation of the effect of vertex geometry on localized surface plasmon resonance of nanostructures. *Opt. Express* **2010**, *18* (2), 843–853.

(27) Gonzalez, A. L.; Noguez, C. Influence of Morphology on the Optical Properties of Metal Nanoparticles. **2006**.

(28) Noguez, C. Surface Plasmons on Metal Nanoparticles: The Influence of Shape and Physical Environment. *J. Phys. Chem. C* **2007**, *111* (10), 3806–3819.

(29) Tao, A.; Sinsermsuksakul, P.; Yang, P. Polyhedral Silver Nanocrystals with Distinct Scattering Signatures. *Angew. Chemie Int. Ed.* **2006**, *45* (28), 4597–4601.

(30) Ringe, E.; Zhang, J.; Langille, M. R.; Sohn, K.; Cobley, C.; Au, L.; Xia, Y.; Mirkin, C. A.; Huang, J.; Marks, L. D.; et al. Effect of Size, Shape, Composition, and Support Film on Localized Surface Plasmon Resonance Frequency: A Single Particle Approach Applied to Silver Bipyramids and Gold and Silver Nanocubes. *MRS Proc.* **2011**, *1208*, 1202–1208.

(31) Scholl, J. A.; Koh, A. L.; Dionne, J. A. Quantum plasmon resonances of individual metallic nanoparticles. *Nature* **2012**, *483*, 421.

(32) Chan, G. H.; Zhao, J.; Hicks, E. M.; Schatz, G. C.; Van Duyne, R. P. Plasmonic Properties of Copper Nanoparticles Fabricated by Nanosphere Lithography. *Nano Lett.* **2007**, *7* (7), 1947–1952.

(33) McPeak, K. M.; Jayanti, S. V; Kress, S. J. P.; Meyer, S.; Iotti, S.; Rossinelli, A.; Norris, D. J. Plasmonic Films Can Easily Be Better: Rules and Recipes. *ACS Photonics* **2015**, *2* (3), 326.

(34) Wang, X.; Santschi, C.; Martin, O. J. F. Strong Improvement of Long-Term Chemical and Thermal Stability of Plasmonic Silver Nanoantennas and Films. *Small* **2017**, *13* (28), 1700044.

(35) Jain, P. K.; Huang, X.; El-Sayed, I. H.; El-Sayed, M. A. Noble Metals on the Nanoscale: Optical and Photothermal Properties and Some Applications in Imaging, Sensing, Biology, and Medicine. *Acc. Chem. Res.* **2008**, *41* (12), 1578–1586.

(36) Mock, J. J.; Barbic, M.; Smith, D. R.; Schultz, D. A.; Schultz, S. Shape effects in plasmon resonance of individual colloidal silver nanoparticles. *J. Chem. Phys.* **2002**, *116* (15), 6755–6759.

(37) Han, Y.; Lupitskyy, R.; Chou, T.-M.; Stafford, C. M.; Du, H.; Sukhishvili, S. Effect of Oxidation on Surface-Enhanced Raman Scattering Activity of Silver Nanoparticles: A Quantitative Correlation. *Anal. Chem.* **2011**, *83* (15), 5873–5880.

(38) Wei, L.; Lu, J.; Xu, H.; Patel, A.; Chen, Z.-S.; Chen, G. Silver nanoparticles: synthesis, properties, and therapeutic applications. *Drug Discov. Today* **2015**, *20* (5), 595–601.

(39) Commercializing plasmonics. *Nat. Photonics* **2015**, *9*, 477.

(40) Santbergen, R.; Temple, T. L.; Liang, R.; Smets, A. H. M.; Swaaij, R. A. C. M. M. van; Zeman, M. Application of plasmonic silver island films in thin-film silicon solar cells. *J. Opt.* **2012**, *14* (2), 24010.

(41) Saha, K.; Agasti, S. S.; Kim, C.; Li, X.; Rotello, V. M. Gold Nanoparticles in Chemical and Biological Sensing. *Chem. Rev.* **2012**, *112* (5), 2739–2779.

(42) Hu, M.; Chen, J.; Li, Z.-Y.; Au, L.; Hartland, G. V; Li, X.; Marquez, M.; Xia, Y. Gold nanostructures: engineering their plasmonic properties for biomedical applications. *Chem. Soc. Rev.* **2006**, *35* (11), 1084–1094.

(43) Whitney, I.; Steven, L.; Daniel, C.; Yiping, Z. Ag–Cu mixed phase plasmonic nanostructures fabricated by shadow nanosphere lithography and glancing angle co-deposition. *Nanotechnology* **2017**, *28* (1), 15301.

(44) Fedyanin, D. Y.; Yakubovsky, D. I.; Kirtaev, R. V; Volkov, V. S. Ultralow-Loss CMOS Copper Plasmonic Waveguides. *Nano Lett.* **2016**, *16* (1), 362–366.

(45) Parveen, F.; Sannakki, B.; Mandke, M. V; Pathan, H. M. Copper nanoparticles: Synthesis methods and its light harvesting performance. *Sol. Energy Mater. Sol. Cells* **2016**, *144*, 371–382.

(46) Egerton, R. F. *Electron Energy-Loss Spectroscopy in the Electron Microscope*; SpringerLink, Red; Boston, MA : Springer Science+Business Media, LLC: Boston, MA, 2011.

(47) Knight, M. W.; King, N. S.; Liu, L.; Everitt, H. O.; Nordlander, P.; Halas, N. J. Aluminum for Plasmonics. *ACS Nano* **2014**, *8* (1), 834–840.

(48) Lee, M.; Kim, J. U.; Lee, K. J.; Ahn, S.; Shin, Y.-B.; Shin, J.; Park, C. B. Aluminum Nanoarrays for Plasmon-Enhanced Light Harvesting. *ACS Nano* **2015**, *9* (6), 6206–6213.

(49) Ray, K.; Chowdhury, M. H.; Lakowicz, J. R. Aluminum Nanostructured Films as Substrates for Enhanced Fluorescence in the Ultraviolet-Blue Spectral Region. *Anal. Chem.* **2007**, *79* (17), 6480–6487.

(50) Naik, G. V; Shalaev, V. M.; Boltasseva, A. Alternative Plasmonic Materials: Beyond Gold and Silver. *Adv. Mater.* **2013**, *25* (24), 3264–3294.

(51) Khurgin, J. B. Replacing noble metals with alternative materials in plasmonics and metamaterials: how good an idea? *Philos. Trans. R. Soc. A Math. Physical Eng. Sci.* **2017**, *375* (2090).

(52) Gao, C.; Hu, Y.; Wang, M.; Chi, M.; Yin, Y. Fully Alloyed Ag/Au Nanospheres: Combining the Plasmonic Property of Ag with the Stability of Au. *J. Am. Chem. Soc.* **2014**, *136* (20), 7474–7479.

(53) Hambrock, J.; Schröter, M. K.; Birkner, A.; Wöll, C.; Fischer, R. A. Nano-Brass: Bimetallic Copper/Zinc Colloids by a Nonaqueous Organometallic Route Using [Cu(OCH(Me)CH2NMe2)2] and Et2Zn as Precursors. *Chem. Mater.* **2003**, *15* (22), 4217–4222.

(54) Armelles, G.; Cebollada, A.; García-Martín, A.; González, M. U. Magnetoplasmonics: Combining Magnetic and Plasmonic Functionalities. *Adv. Opt. Mater.* **2013**, *1* (1), 10–35.

(55) Temnov, V. V; Armelles, G.; Woggon, U.; Guzatov, D.; Cebollada, A.; Garcia-Martin, A.; Garcia-Martin, J.-M.; Thomay, T.; Leitenstorfer, A.; Bratschitsch, R. Active magneto-plasmonics in hybrid metal–ferromagnet structures. *Nat. Photonics* **2010**, *4*, 107.

(56) Lou, Z.; Wang, Z.; Huang, B.; Dai, Y. Synthesis and Activity of Plasmonic Photocatalysts. *ChemCatChem* **2014**, *6* (9), 2456–2476.

(57) Yu, J.; Zhou, L.; Wang, Y.; Tan, Y.; Wang, Z.; Zhu, S.; Zhu, J. Three-dimensional TiO2/Au nanoparticles for plasmon enhanced photocatalysis. *J. Opt.* **2018**, *20* (3), 34005.

(58) Seh, Z. W.; Liu, S.; Low, M.; Zhang, S.-Y.; Liu, Z.; Mlayah, A.; Han, M.-Y. Janus Au-TiO2 Photocatalysts with Strong Localization of Plasmonic Near-Fields for Efficient Visible-Light Hydrogen Generation. *Adv. Mater.* **2012**, *24* (17), 2310–2314.

(59) Bansal, A.; Sekhon, J. S.; Verma, S. S. Scattering Efficiency and LSPR Tunability of Bimetallic Ag, Au, and Cu Nanoparticles. *Plasmonics* **2014**, *9* (1), 143–150.

(60) Wu, Y.; Li, G.; Cherqui, C.; Bigelow, N. W.; Thakkar, N.; Masiello, D. J.; Camden, J. P.; Rack, P. D. Electron Energy Loss Spectroscopy Study of the Full Plasmonic Spectrum of Self-Assembled Au–Ag Alloy Nanoparticles: Unraveling Size, Composition, and Substrate Effects. *ACS Photonics* **2016**, *3* (1), 130–138.

(61) Hashimoto, Y.; Seniutinas, G.; Balčytis, A.; Juodkazis, S.; Nishijima, Y. Au-Ag-Cu nano-alloys: tailoring of permittivity. *Sci. Rep.* **2016**, *6*, 25010.

(62) Wu, Y.; Li, G.; Camden, J. P. Probing Nanoparticle Plasmons with Electron Energy Loss Spectroscopy. *Chem. Rev.* **2018**, *118* (6), 2994–3031.

(63) Kneipp, K.; Kneipp, H.; Kneipp, J. Probing plasmonic nanostructures by photons and electrons. *Chemical Science*. Royal Society of Chemistry Mei 1, 2015, bll 2721–2726.

(64) Howie, A. Electrons and photons: exploiting the connection. In *Inst. Phys. Conf. Ser. 161*; Sheffield, 1999; bl 311.

(65) García de Abajo, F. J.; Kociak, M. Electron energy-gain spectroscopy. *New J. Phys.* **2008**, *10* (7), 073035.

(66) Liu, C.; Wu, Y.; Hu, Z. Z.; Busche, J. A.; Beutler, E. K.; Montoni, N. P.; Moore, T. M.; Magel, G. A.; Camden, J. P.; Masiello, D. J.; et al. Continuous Wave Resonant Photon Stimulated Electron Energy-Gain and Electron Energy-Loss Spectroscopy of Individual Plasmonic Nanoparticles. *ACS Photonics* **2019**.

(67) Barwick, B.; Flannigan, D. J.; Zewail, A. H. Photon-induced near-field electron microscopy. *Nature* **2009**, *462* (7275), 902–906.

(68) Yurtsever, A.; Baskin, J. S.; Zewail, A. H. Entangled Nanoparticles: Discovery by Visualization in 4D Electron Microscopy. *Nano Lett.* **2012**, *12* (9), 5027–5032.

(69) Pomarico, E.; Madan, I.; Berruto, G.; Vanacore, G. M.; Wang, K.; Kaminer, I.; García de Abajo, F. J.; Carbone, F. meV Resolution in Laser-Assisted Energy-Filtered Transmission Electron Microscopy. *ACS Photonics* **2018**, *5* (3), 759–764.

(70) Kaplan, M.; Yoo, B. K.; Tang, J.; Karam, T. E.; Liao, B.; Majumdar, D.; Baltimore, D.; Jensen, G. J.; Zewail, A. H. Photon-Induced Near-Field Electron Microscopy of Eukaryotic Cells. *Angew. Chemie - Int. Ed.* **2017**, *56* (38), 11498–11501.

(71) García de Abajo, F. J.; Asenjo-Garcia, A.; Kociak, M. Multiphoton Absorption and Emission by Interaction of Swift Electrons with Evanescent Light Fields. *Nano Lett.* **2010**, *10* (5), 1859–1863.

(72) Park, S. T.; Lin, M.; Zewail, A. H. Photon-induced near-field electron microscopy (PINEM): theoretical and experimental. *New J. Phys.* **2010**, *12* (12), 123028.

(73) Asenjo-Garcia, A.; García de Abajo, F. J. Plasmon electron energy-gain spectroscopy. *New J. Phys.* **2013**, *15* (10), 103021.

(74) Barwick, B.; Zewail, A. H. Photonics and Plasmonics in 4D Ultrafast Electron Microscopy. *ACS Photonics* **2015**, *2* (10), 1391–1402.

(75) Shorokhov, D.; Zewail, A. H. Perspective: 4D ultrafast electron microscopy - Evolutions and revolutions. *J. Chem. Phys.* **2016**, *144* (8).

(76) Feist, A.; Bach, N.; Rubiano da Silva, N.; Danz, T.; Möller, M.; Priebe, K. E.; Domröse, T.; Gatzmann, J. G.; Rost, S.; Schauss, J.; et al. Ultrafast transmission electron microscopy using a laser-driven field emitter: Femtosecond resolution with a high coherence electron beam. *Ultramicroscopy* **2017**, *176*, 63–73.

(77) Losquin, A.; Lummen, T. T. A. Electron microscopy methods for space-, energy-, and time-resolved plasmonics. *Front. Phys.* **2017**, *12* (1).

(78) Zewail, A. H. Four-dimensional electron microscopy. *Science*. April 9, 2010, bll 187–193.

(79) Das, P.; Blazit, J. D.; Tencé, M.; Zagonel, L. F.; Auad, Y.; Lee, Y. H.; Ling, X. Y.; Losquin, A.; Colliex, C.; Stéphan, O.; et al. Stimulated electron energy loss and gain in an electron microscope without a pulsed electron gun. *Ultramicroscopy* **2019**, *203*, 44–51.

(80) Klein, K. L.; Melechko, A. V; Fowlkes, J. D.; Rack, P. D.; Hensley, D. K.; Meyer, H. M.; Allard, L. F.; McKnight, T. E.; Simpson, M. L. Formation of Ultrasharp Vertically Aligned Cu−Si Nanocones by a DC Plasma Process. *J. Phys. Chem. B* **2006**, *110* (10), 4766–4771.

(81) Klein, K. L.; Melechko, A. V; Rack, P. D.; Fowlkes, J. D.; Meyer, H. M.; Simpson, M. L. Cu–Ni composition gradient for the catalytic synthesis of vertically aligned carbon nanofibers. *Carbon N. Y.* **2005**, *43* (9), 1857–1863.

(82) Guo, Q.; Noh, J. H.; Liaw, P. K.; Rack, P. D.; Li, Y.; Thompson, C. V. Density change upon crystallization of amorphous Zr–Cu–Al thin films. *Acta Mater.* **2010**, *58* (10), 3633–3641.

(83) Guan, Y.; Wang, X.; Liu, Y.; Potter, M. D.; Sorge, K. D.; Rack, P. D. Combinatorial synthesis and characterization of magnetic FexAl1−xNyO1−y thin films. *Thin Solid Films* **2008**, *516* (18), 6063–6070.

(84) Wu, Y.; Fowlkes, J. D.; Rack, P. D. The optical properties of Cu-Ni nanoparticles produced via pulsed laser dewetting of ultrathin films: The effect of nanoparticle size and composition on the plasmon response. *J. Mater. Res.* **2011**, *26* (2), 277–287.

(85) Peak, J. D.; Melcher, C. L.; Rack, P. D. Combinatorial thin film sputtering investigation of cerium concentration in Lu2SiO5 scintillators. *J. Lumin.* **2010**, *130* (8), 1366–1370.

(86) Peak, J. D.; Melcher, C. L.; Rack, P. D. Combinatorial Thin Film Synthesis of Cerium Doped Scintillation Materials in the Lutetium Oxide—Silicon Oxide System. *IEEE Trans. Nucl. Sci.* **2008**, *55* (3), 1480–1483.

(87) Fowlkes, J. D.; Fitz-Gerald, J. M.; Rack, P. D. Ultraviolet emitting (Y1−xGdx)2O3−δ thin films deposited by radio frequency magnetron sputtering: Combinatorial modeling, synthesis, and rapid characterization. *Thin Solid Films* **2006**, *510* (1), 68–76.

(88) Deng, Y.; Fowlkes, J. D.; Rack, P. D.; Fitz-Gerald, J. M. Thin film rf magnetron sputtering of gadolinium-doped yttrium aluminum garnet ultraviolet emitting materials. *Opt. Mater. (Amst).* **2006**, *29* (2), 183–191.

(89) Fowlkes, J. D.; Fitz-Gerald, J. M.; Rack, P. D. Ultraviolet emitting (Y1−xGdx)2O3−δ thin films deposited by radio frequency magnetron sputtering; structure-property-thin film processing relationships. *Thin Solid Films* **2007**, *515* (7), 3488–3498.

(90) Deng, Y.; Fowlkes, J. D.; Fitz-Gerald, J. M.; Rack, P. D. Combinatorial thin film synthesis of Gd-doped Y3Al5O12 ultraviolet emitting materials. *Appl. Phys. A* **2005**, *80* (4), 787–789.

(91) Jun, S.-I.; Rack, P. D.; McKnight, T. E.; Melechko, A. V; Simpson, M. L. Electrical and microstructural characterization of molybdenum tungsten electrodes using a combinatorial thin film sputtering technique. *J. Appl. Phys.* **2005**, *97* (5), 54906.

(92) Deng, Y. P.; Guan, Y. F.; Fowlkes, J. D.; Wen, S. Q.; Liu, F. X.; Pharr, G. M.; Liaw, P. K.; Liu, C. T.; Rack, P. D. A combinatorial thin film sputtering approach for synthesizing and characterizing ternary ZrCuAl metallic glasses. *Intermetallics* **2007**, *15* (9), 1208–1216.

(93) Specht, E. D.; Rack, P. D.; Rar, A.; Pharr, G. M.; George, E. P.; Fowlkes, J. D.; Hong, H.; Karapetrova, E. Metastable phase evolution and grain growth in annealed nanocrystalline Cr–Fe–Ni films. *Thin Solid Films* **2005**, *493* (1), 307–312.

(94) Rar, A.; Frafjord, J. J.; Jason, D. F.; Specht, E. D.; Rack, P. D.; Santella, M. L.; Bei, H.; George, E. P.; Pharr, G. M. PVD synthesis and high-throughput property characterization of Ni–Fe–Cr alloy libraries. *Meas. Sci. Technol.* **2005**, *16* (1), 46.

(95) Nagase, T.; Anada, S.; Rack, P. D.; Noh, J. H.; Yasuda, H.; Mori, H.; Egami, T. MeV electron-irradiation-induced structural change in the bcc phase of Zr–Hf–Nb alloy with an approximately equiatomic ratio. *Intermetallics* **2013**, *38*, 70–79.

(96) Nagase, T.; Anada, S.; Rack, P. D.; Noh, J. H.; Yasuda, H.; Mori, H.; Egami, T. Electron-irradiation-induced structural change in Zr–Hf–Nb alloy. *Intermetallics* **2012**, *26*, 122–130.

(97) Li, G.; Zhou, L.; Guevarra, D.; Suram, S. K.; Shinde, A.; Li, G.; Zhou, L.; Guevarra, D.; Suram, S. K.; Toma, F. M.; et al. The role of the CeO 2 /BiVO 4 interface in optimized Fe–Ce oxide coatings for solar fuels photoanodes. *J. Mater. Chem. A.* **2016**, *4* (37), 14356–14363.

(98) Jeon, M. K.; Lee, C. H.; Park, G. Il; Kang, K. H. Combinatorial search for oxygen reduction reaction electrocatalysts: A review. *J. Power Sources* **2012**, *216*, 400–408.

(99) Yang, K.; Bedenbaugh, J.; Li, H.; Peralta, M.; Bunn, J. K.; Lauterbach, J.; Hattrick-Simpers, J. Development of a High-Throughput Methodology for Screening Coking Resistance of Modified Thin-Film Catalysts. *ACS Comb. Sci.* **2012**, *14* (6), 372–377.

(100) König, D.; Richter, K.; Siegel, A.; Mudring, A.-V.; Ludwig, A. High-Throughput Fabrication of Au–Cu Nanoparticle Libraries by Combinatorial Sputtering in Ionic Liquids. *Adv. Funct. Mater.* **2013**, *24* (14), 2049–2056.

(101) Liu, Y.; Padmanabhan, J.; Cheung, B.; Liu, J.; Chen, Z.; Scanley, B. E.; Wesolowski, D.; Pressley, M.; Broadbridge, C. C.; Altman, S.; et al. Combinatorial development of antibacterial Zr-Cu-Al-Ag thin film metallic glasses. *Sci. Rep.* **2016**, *6*, 26950.

(102) Alexandrakis, V.; Koenig, D.; Kusne, A. G.; Gao, T.; Fackler, S. W.; König, D.; Kusne, A. G.; Kramer, M. J.; Stasak, D.; Lopez, K.; et al. Combinatorial study of Fe-Co-V hard magnetic thin films. *Sci. Technol. Adv. Mater.* **2017**, *18* (1), 231–238.

(103) Suchoski, R.; Fackler, S.; Zhang, Y.; Pan, X.; Jin, K.; Greene, R. L.; Takeuchi, I. Combinatorial search of superconductivity in Fe-B composition spreads. *APL Mater.* **2013**, *1* (4), 42101.

(104) Liu, Y.; Gong, P.; Li, Y.; Moore, K. M.; Liu, J.; Moore, K. M.; Scanley, E.; Walker, F.; Broadbridge, C. C.; Schroers, J. Combinatorial exploration of color in gold-based alloys. *Gold Bull.* **2015**, *48* (3–4), 111–118.

(105) Han, Y.; Siol, S.; Zhang, Q.; Zakutayev, A. Optoelectronic Properties of Strontium and Barium Copper Sulfides Prepared by Combinatorial Sputtering. *Chem. Mater.* **2017**, *29* (19), 8239–8248.

(106) McCluskey, P. J.; Xiao, K.; Gregoire, J. M.; Dale, D.; Vlassak, J. J. Application of in-situ nano-scanning calorimetry and X-ray diffraction to characterize Ni–Ti–Hf high-temperature shape memory alloys. *Thermochim. Acta* **2015**, *603*, 53–62.

(107) Fioretti, A. N.; Zakutayev, A.; Moutinho, H.; Melamed, C.; Perkins, J. D.; Perkins, J. D.; Norman, A. G.; Al-Jassim, M.; Toberer, E. S.; Tamboli, A. C. Combinatorial insights into doping control and transport properties of zinc tin nitride. *J. Mater. Chem.* **2015**, *3* (42), 11017–11028.

(108) Chang, K. S.; Green, M. L.; Suehle, J.; Vogel, E. M.; Xiong, H.; Hattrick-Simpers, J.; Takeuchi, I.; Famodu, O.; Ohmori, K.; Ahmet, P.; et al. Combinatorial study of Ni–Ti–Pt ternary metal gate electrodes on HfO2 for the advanced gate stack. *Appl. Phys. Lett.* **2006**, *89* (14), 142108.

(109) Motemani, Y.; McCluskey, P. J.; Zhao, C.; Tan, M. J.; Vlassak, J. J. Analysis of Ti–Ni–Hf shape memory alloys by combinatorial nanocalorimetry. *Acta Mater.* **2011**, *59* (20), 7602–7614.

(110) Green, M. L.; Takeuchi, I.; Hattrick-Simpers, J. R. Applications of high throughput (combinatorial) methodologies to electronic, magnetic, optical, and energy-related materials. *J. Appl. Phys.* **2013**, *113* (23), 231101.

(111) Gebhardt, T.; Music, D.; Takahashi, T.; Schneider, J. M. Combinatorial thin film materials science: From alloy discovery and optimization to alloy design. *Thin Solid Films* **2012**, *520* (17), 5491–5499.

(112) Mao, S. S.; Burrows, P. E. Combinatorial screening of thin film materials: An overview. *J. Mater.* **2015**, *1* (2), 85–91.

(113) Potyrailo, R.; Rajan, K.; Stoewe, K.; Takeuchi, I.; Chisholm, B.; Lam, H. Combinatorial and High-Throughput Screening of Materials Libraries: Review of State of the Art. *ACS Comb. Sci.* **2011**, *13* (6), 579–633.

(114) Blaber, M. G.; Arnold, M. D.; Ford, M. J. A review of the optical properties of alloys and intermetallics for plasmonics. *J. Phys. Condens. Matter* **2010**, *22* (14), 143201.

(115) Peña-Rodríguez, O.; Caro, M.; Rivera, A.; Olivares, J.; Perlado, J. M.; Caro, A. Optical properties of Au-Ag alloys: An ellipsometric study. *Opt. Mater. Express* **2014**, *4* (2), 403–410.

(116) Yang, G.; Fu, X.; Zhou, J. Dielectric properties of the silver-copper alloy films deposited by magnetron sputtering. *J. Opt. Soc. Am. B* **2013**, *30* (2), 282–287.

(117) Keast, V. J.; Zwan, B.; Supansomboon, S.; Cortie, M. B.; Persson, P. O. Å. AuAl2 and PtAl2 as potential plasmonic materials. *J. Alloys Compd.* **2013**, *577* (Supplement C), 581–586.

(118) Keast, V. J.; Barnett, R. L.; Cortie, M. B. First principles calculations of the optical and plasmonic response of Au alloys and intermetallic compounds. *J. Phys. Condens. Matter* **2014**, *26* (30), 305501.

(119) De Silva, K. S. B.; Keast, V. J.; Cortie, M. B. Effect of Al additions on the optical properties of Au α-phase. *J. Alloys Compd.* **2016**, *679* (Supplement C), 225–230.

(120) Murray, J. L.; Okamoto, H.; Massalski, T. B. The Al−Au (Aluminum-gold) system. *Bull. Alloy Phase Diagrams* **1987**, *8* (1), 20–30.

(121) Bearden, J. A. X-Ray Wavelengths. *Rev. Mod. Phys.* **1967**, *39* (1), 78–124.

(122) Mitchell, D. R. G. DiffTools: Electron diffraction software tools for DigitalMicrograph™. *Microsc. Res. Tech.* **2008**, *71* (8), 588–593.

(123) Li, M.; Li, C.; Wang, F.; Luo, D.; Zhang, W. Thermodynamic assessment of the Al–Au system. *J. Alloys Compd.* **2004**, *385* (1), 199–206.

(124) Xu, C.; Sritharan, T.; Mhaisalkar, S. G. Thin film aluminum–gold interface interactions. *Scr. Mater.* **2007**, *56* (6), 549–552.

(125) Majni, G.; Nobili, C.; Ottaviani, G.; Costato, M.; Galli, E. Gold-aluminum thin-film interactions and compound formation. *J. Appl. Phys.* **1981**, *52* (6), 4047–4054.

(126) Chantler, C. T. Theoretical Form Factor, Attenuation, and Scattering Tabulation for Z=1–92 from E=1–10 eV to E=0.4–1.0 MeV. *J. Phys. Chem. Ref. Data* **1995**, *24* (1), 71–643.

(127) Keast, V. J.; Birt, K.; Koch, C. T.; Supansomboon, S.; Cortie, M. B. The role of plasmons and interband transitions in the color of AuAl2, AuIn2, and AuGa2. *Appl. Phys. Lett.* **2011**, *99* (11), 111908.

(128) Keast, V. J.; Wallace, J. W.; Wrightson, C. J.; Tai, M.; Gentle, A.; Arnold, M. D.; Cortie, M. B. The effect of vacancies on the optical properties of AuAl 2. *J. Phys. Condens. Matter* **2015**, *27* (50), 505501.

(129) Petri, E.; Otto, A. Direct Nonvertical Interband and Intraband Transitions in Al. *Phys. Rev. Lett.* **1975**, *34* (20), 1283–1286.

(130) Wu, Y.; Liu, C.; Moore, T. M.; Magel, G. A.; Garfinkel, D. A.; Camden, J. P.; Stanford, M. G.; Duscher, G.; Rack, P. D. Exploring Photothermal Pathways via in Situ Laser Heating in the Transmission Electron Microscope: Recrystallization, Grain Growth, Phase Separation, and Dewetting in Ag0.5Ni0.5 Thin Films. *Microsc. Microanal.* **2018**, *24* (6), 647–656.

(131) Langhammer, C.; Schwind, M.; Kasemo, B.; Zorić, I. Localized Surface Plasmon Resonances in Aluminum Nanodisks. *Nano Lett.* **2008**, *8* (5), 1461–1471.

(132) Chan, G. H.; Zhao, J.; Schatz, G. C.; Van Duyne, R. P. Localized Surface Plasmon Resonance Spectroscopy of Triangular Aluminum Nanoparticles. *J. Phys. Chem. C* **2008**, *112* (36), 13958–13963.

(133) Zorić, I.; Zäch, M.; Kasemo, B.; Langhammer, C. Gold, Platinum, and Aluminum Nanodisk Plasmons: Material Independence, Subradiance, and Damping Mechanisms. *ACS Nano* **2011**, *5* (4), 2535–2546.

(134) Jahn, M.; Patze, S.; Hidi, I. J.; Knipper, R.; Radu, A. I.; Mühlig, A.; Yüksel, S.; Peksa, V.; Weber, K.; Mayerhöfer, T.; et al. Plasmonic nanostructures for surface enhanced spectroscopic methods. *Analyst* **2016**, *141* (3), 756–793.

(135) Tian, S.; Neumann, O.; McClain, M. J.; Yang, X.; Zhou, L.; Zhang, C.; Nordlander, P.; Halas, N. J. Aluminum Nanocrystals: A Sustainable Substrate for Quantitative SERS-Based DNA Detection. *Nano Lett.* **2017**, *17* (8), 5071–5077.

(136) Huang, J.; Zhu, Y.; Lin, M.; Wang, Q.; Zhao, L.; Yang, Y.; Yao, K. X.; Han, Y. Site-Specific Growth of Au–Pd Alloy Horns on Au Nanorods: A Platform for Highly Sensitive Monitoring of Catalytic Reactions by Surface Enhancement Raman Spectroscopy. *J. Am. Chem. Soc.* **2013**, *135* (23), 8552–8561.

(137) Lee, Y. W.; Kim, N. H.; Lee, K. Y.; Kwon, K.; Kim, M.; Han, S. W. Synthesis and Characterization of Flower-Shaped Porous Au−Pd Alloy Nanoparticles. *J. Phys. Chem. C* **2008**, *112* (17), 6717–6722.

(138) Fan, M.; Lai, F.-J.; Chou, H.-L.; Lu, W.-T.; Hwang, B.-J.; Brolo, A. G. Surface-enhanced Raman scattering (SERS) from Au:Ag bimetallic nanoparticles: the effect of the molecular probe. *Chem. Sci.* **2013**, *4* (1), 509–515.

(139) Liu, Z.; Yang, Z.; Peng, B.; Cao, C.; Zhang, C.; You, H.; Xiong, Q.; Li, Z.; Fang, J. Highly Sensitive, Uniform, and Reproducible Surface-Enhanced Raman Spectroscopy from Hollow Au-Ag Alloy Nanourchins. *Adv. Mater.* **2014**, *26* (15), 2431–2439.

(140) Jiang, Z.; Zhang, Q.; Zong, C.; Liu, B.-J.; Ren, B.; Xie, Z.; Zheng, L. Cu–Au alloy nanotubes with five-fold twinned structure and their application in surface-enhanced Raman scattering. *J. Mater. Chem.* **2012**, *22* (35), 18192–18197.

(141) Shi, T.; Kong, J.; Wang, X.; Li, X. Preparation of multifunctional Al-Mg alloy surface with hierarchical micro/nanostructures by selective chemical etching processes. *Appl. Surf. Sci.* **2016**, *389*, 335–343.

(142) Cherepy, N. J.; Shen, T. H.; Esposito, A. P.; Tillotson, T. M. Characterization of an effective cleaning procedure for aluminum alloys: surface enhanced Raman spectroscopy and zeta potential analysis. *J. Colloid Interface Sci.* **2005**, *282* (1), 80–86.

(143) Joo, T. H.; Kim, M. S.; Kim, K. Surface-enhanced Raman scattering of benzenethiol in silver sol. *J. Raman Spectrosc.* **1987**, *18* (1), 57–60.

(144) Farcau, C.; Astilean, S. Mapping the SERS Efficiency and Hot-Spots Localization on Gold Film over Nanospheres Substrates. *J. Phys. Chem. C* **2010**, *114* (27), 11717–11722.

(145) Baia, L.; Baia, M.; Popp, J.; Astilean, S. Gold Films Deposited over Regular Arrays of Polystyrene Nanospheres as Highly Effective SERS Substrates from Visible to NIR. *J. Phys. Chem. B* **2006**, *110* (47), 23982–23986.

(146) Le Ru, E. C.; Blackie, E.; Meyer, M.; Etchegoin, P. G. Surface Enhanced Raman Scattering Enhancement Factors: A Comprehensive Study. *J. Phys. Chem. C* **2007**, *111* (37), 13794–13803.

(147) Camden, J. P.; Dieringer, J. A.; Zhao, J.; Van Duyne, R. P. Controlled Plasmonic Nanostructures for Surface-Enhanced Spectroscopy and Sensing. *Acc. Chem. Res.* **2008**, *41* (12), 1653–1661.

(148) Amendola, V.; Scaramuzza, S.; Agnoli, S.; Polizzi, S.; Meneghetti, M. Strong dependence of surface plasmon resonance and surface enhanced Raman scattering on the composition of Au–Fe nanoalloys. *Nanoscale* **2014**, *6* (3), 1423–1433.

(149) Amendola, V.; Meneghetti, M.; Bakr, O. M.; Riello, P.; Polizzi, S.; Anjum, D. H.; Fiameni, S.; Arosio, P.; Orlando, T.; de Julian Fernandez, C.; et al. Coexistence of plasmonic and magnetic properties in Au89Fe11 nanoalloys. *Nanoscale* **2013**, *5* (12), 5611–5619.

(150) McKeown, J. T.; Wu, Y.; Fowlkes, J. D.; Rack, P. D.; Campbell, G. H. Simultaneous In-Situ Synthesis and Characterization of Co@Cu Core-Shell Nanoparticle Arrays. *Adv. Mater.* **2015**, *27* (6), 1060–1065.

(151) Garcia, H.; Sachan, R.; Kalyanaraman, R. Optical Plasmon Properties of Co-Ag Nanocomposites Within the Mean-Field Approximation. *Plasmonics* **2012**, *7* (1), 137–141.

(152) Sachan, R.; Malasi, A.; Ge, J.; Yadavali, S.; Krishna, H.; Gangopadhyay, A.; Garcia, H.; Duscher, G.; Kalyanaraman, R. Ferroplasmons: Intense Localized Surface Plasmons in Metal-Ferromagnetic Nanoparticles. *ACS Nano* **2014**, *8* (10), 9790–9798.

(153) Messina, G. C.; Sinatra, M. G.; Bonanni, V.; Brescia, R.; Alabastri, A.; Pineider, F.; Campo, G.; Sangregorio, C.; Li-Destri, G.; Sfuncia, G.; et al. Tuning the Composition of Alloy Nanoparticles Through Laser Mixing: The Role of Surface Plasmon Resonance. *J. Phys. Chem. C* **2016**, *120* (23), 12810–12818.

(154) Yates, E. L. XLI. Precision measurements of crystal parameters AU - Owen, E.A. *London, Edinburgh, Dublin Philos. Mag. J. Sci.* **1933**, *15* (98), 472–488.

(155) Jette, E. R.; Foote, F. Precision Determination of Lattice Constants. *J. Chem. Phys.* **1935**, *3* (10), 605–616.

(156) Wang, J.; Lu, X.-G.; Sundman, B.; Su, X. Thermodynamic assessment of the Au–Ni system. *Calphad* **2005**, *29* (4), 263–268.

(157) Cen, X.; Zhang, X.; Thron, A. M.; van Benthem, K. Agglomeration and long-range edge retraction for Au/Ni bilayer films during thermal annealing. *Acta Mater.* **2016**, *119*, 167–176.

(158) Bassett, M.; Beaglehole, D. Optical studies of dilute AuNi alloys. *J. Phys. F Met. Phys.* **1976**, *6* (6), 1211–1221.

(159) McPherson, D. J.; Supansomboon, S.; Zwan, B.; Keast, V. J.; Cortie, D. L.; Gentle, A.; Dowd, A.; Cortie, M. B. Strategies to control the spectral properties of Au–Ni thin films. *Thin Solid Films* **2014**, *551*, 200–204.

(160) Kim, T. J.; Ghong, T. H.; Kim, Y. D.; Aspnes, D. E.; Klein, M. V; Ko, D.-S.; Kim, Y.-W.; Elarde, V. C.; Coleman, J. J. Investigation of effective-medium approximation, alloy, average-composition, and graded-composition models for interface analysis by spectroscopic ellipsometry. *J. Appl. Phys.* **2007**, *102* (6), 63512.

(161) Link, S.; Wang, Z. L.; El-Sayed, M. A. Alloy Formation of Gold−Silver Nanoparticles and the Dependence of the Plasmon Absorption on Their Composition. *J. Phys. Chem. B* **1999**, *103* (18), 3529–3533.

(162) Gaudry, M.; Lermé, J.; Cottancin, E.; Pellarin, M.; Vialle, J.-L.; Broyer, M.; Prével, B.; Treilleux, M.; Mélinon, P. Optical properties of AuxAg1-x clusters embedded in alumina: Evolution with size and stoichiometry. *Phys. Rev. B* **2001**, *64* (8), 85407.

(163) Orosco, J.; Coimbra, C. F. M. On a causal dispersion model for the optical properties of metals. *Appl. Opt.* **2018**, *57* (19), 5333–5347.

(164) Collette, R.; Wu, Y.; Olafsson, A.; Camden, J. P.; Rack, P. D. Combinatorial Thin Film Sputtering AuxAl1- x Alloys: Correlating Composition and Structure with Optical Properties. *ACS Comb. Sci.* **2018**, *20* (11).

(165) Peña-Rodríguez, O. Modelling the dielectric function of Au-Ag alloys. *J. Alloys Compd.* **2017**, *694*, 857–863.

(166) Olmon, R. L.; Slovick, B.; Johnson, T. W.; Shelton, D.; Oh, S.-H.; Boreman, G. D.; Raschke, M. B. Optical dielectric function of gold. *Phys. Rev. B* **2012**, *86* (23), 235147.

(167) Clavero, C. Plasmon-induced hot-electron generation at nanoparticle/metal-oxide interfaces for photovoltaic and photocatalytic devices. *Nat. Photonics* **2014**, *8* (2), 95–103.

(168) Ferry, V. E.; Munday, J. N.; Atwater, H. A. Design Considerations for Plasmonic Photovoltaics. *Adv. Mater.* **2010**, *22* (43), 4794–4808.

(169) Beck, F. J.; Polman, A.; Catchpole, K. R. Tunable light trapping for solar cells using localized surface plasmons. *J. Appl. Phys.* **2009**, *105* (11), 114310.

(170) Awazu, K.; Fujimaki, M.; Rockstuhl, C.; Tominaga, J.; Murakami, H.; Ohki, Y.; Yoshida, N.; Watanabe, T. A Plasmonic Photocatalyst Consisting of Silver Nanoparticles Embedded in Titanium Dioxide. *J. Am. Chem. Soc.* **2008**, *130* (5), 1676–1680.

(171) Hou, W.; Cronin, S. B. A Review of Surface Plasmon Resonance-Enhanced Photocatalysis. *Adv. Funct. Mater.* **2013**, *23* (13), 1612–1619.

(172) Anker, J. N.; Hall, W. P.; Lyandres, O.; Shah, N. C.; Zhao, J.; Van Duyne, R. P. Biosensing with plasmonic nanosensors. *Nat. Mater.* **2008**, *7* (6), 442–453.

(173) Unser, S.; Bruzas, I.; He, J.; Sagle, L. Localized Surface Plasmon Resonance Biosensing: Current Challenges and Approaches. *Sensors* **2015**, *15* (7), 15684–15716.

(174) Kumar, A.; Kim, S.; Nam, J.-M. Plasmonically Engineered Nanoprobes for Biomedical Applications. *J. Am. Chem. Soc.* **2016**, *138* (44), 14509–14525.

(175) Bozhevolnyi, S. I.; Mortensen, N. A. Plasmonics for emerging quantum technologies. *Nanophotonics* **2017**, *6* (5), 1185–1188.

(176) Andersen, M. L.; Stobbe, Sø.; SØrensen, A. Sø.; Lodahl, P. Strongly modified plasmon-matter interaction with mesoscopic quantum emitters. *Nat. Phys.* **2011**, *7* (3), 215–218.

(177) Shalaev, V. M.; Cai, W.; Chettiar, U.; Yuan, H. K.; Sarychev, A. K.; Drachev, V. P.; Kildishev, A. V. Negative index of refraction in optical metamaterials. In *Optics InfoBase Conference Papers*; Optical Society of America, 2005.

(178) Lezec, H. J.; Dionne, J. A.; Atwater, H. A. Negative refraction at visible frequencies. *Science (80-.).* **2007**, *316* (5823), 430–432.

(179) Ju, L.; Geng, B.; Horng, J.; Girit, C.; Martin, M.; Hao, Z.; Bechtel, H. A.; Liang, X.; Zettl, A.; Shen, Y. R.; et al. Graphene plasmonics for tunable terahertz metamaterials. *Nat. Nanotechnol.* **2011**, *6* (10), 630–634.

(180) Alù, A.; Salandrino, A.; Engheta, N. Negative effective permeability and left-handed materials at optical frequencies. *Opt. Express* **2006**, *14* (4), 1557.

(181) Shafiei, F.; Monticone, F.; Le, K. Q.; Liu, X. X.; Hartsfield, T.; Alù, A.; Li, X. A subwavelength plasmonic metamolecule exhibiting magnetic-based optical Fano resonance. *Nat. Nanotechnol.* **2013**, *8* (2), 95–99.

(182) Monticone, F.; Alù, A. The quest for optical magnetism: From split-ring resonators to plasmonic nanoparticles and nanoclusters. *J. Mater. Chem. C* **2014**, *2* (43), 9059–9072.

(183) Cherqui, C.; Wu, Y.; Li, G.; Quillin, S. C.; Busche, J. A.; Thakkar, N.; West, C. A.; Montoni, N. P.; Rack, P. D.; Camden, J. P.; et al. STEM/EELS Imaging of Magnetic Hybridization in Symmetric and Symmetry-Broken Plasmon Oligomer Dimers and All-Magnetic Fano Interference. *Nano Lett.* **2016**, *16* (10), 6668–6676.

(184) Gong, C.; Dias, M. R. S.; Wessler, G. C.; Taillon, J. A.; Salamanca-Riba, L. G.; Leite, M. S. Near-Field Optical Properties of Fully Alloyed Noble Metal Nanoparticles. *Adv. Opt. Mater.* **2017**, *5* (1), 1600568.

(185) Merlen, A.; Lagugné-Labarthet, F. Imaging the Optical Near Field in Plasmonic Nanostructures. *Appl. Spectrosc.* **2014**, *68* (12), 1307–1326.

(186) Pohl, D. W. Optics at the nanometre scale. *Philosophical Transactions of the Royal Society A: Mathematical, Physical and Engineering Sciences*. Royal Society April 15, 2004, bll 701–717.

(187) Hillenbrand, R.; Keilmann, F. Optical oscillation modes of plasmon particles observed in direct space by phase-contrast near-field microscopy. *Appl. Phys. B Lasers Opt.* **2001**, *73* (3), 239–243.

(188) Denkova, D.; Verellen, N.; Silhanek, A. V.; Valev, V. K.; Dorpe, P. Van; Moshchalkov, V. V. Mapping Magnetic Near-Field Distributions of Plasmonic Nanoantennas. *ACS Nano* **2013**, *7* (4), 3168–3176.

(189) Sun, Q.; Ueno, K.; Yu, H.; Kubo, A.; Matsuo, Y.; Misawa, H. Direct imaging of the near field and dynamics of surface plasmon resonance on gold nanostructures using photoemission electron microscopy. *Light Sci. Appl.* **2013**, *2* (12), e118–e118.

(190) Schertz, F.; Schmelzeisen, M.; Mohammadi, R.; Kreiter, M.; Elmers, H.-J.; Schönhense, G. Near Field of Strongly Coupled Plasmons: Uncovering Dark Modes. *Nano Lett.* **2012**, *12* (4), 1885–1890.

(191) García De Abajo, F. J. Optical excitations in electron microscopy. *Reviews of Modern Physics*. Februarie 3, 2010, bll 209–275.

(192) Colliex, C.; Kociak, M.; Stéphan, O. Electron Energy Loss Spectroscopy imaging of surface plasmons at the nanometer scale. *Ultramicroscopy*. Elsevier Maart 1, 2016, bll A1–A24.

(193) Rossouw, D.; Botton, G. A. Plasmonic response of bent silver nanowires for nanophotonic subwavelength waveguiding. *Phys. Rev. Lett.* **2013**, *110* (6).

(194) Rossouw, D.; Couillard, M.; Vickery, J.; Kumacheva, E.; Botton, G. A. Multipolar Plasmonic Resonances in Silver Nanowire Antennas Imaged with a Subnanometer Electron Probe. *Nano Lett.* **2011**, *11* (4), 1499–1504.

(195) Bosman, M.; Ye, E.; Tan, S. F.; Nijhuis, C. A.; Yang, J. K. W.; Marty, R.; Mlayah, A.; Arbouet, A.; Girard, C.; Han, M. Y. Surface plasmon damping quantified with an electron nanoprobe. *Sci. Rep.* **2013**, *3*.

(196) Rossouw, D.; Botton, G. A. Resonant optical excitations in complementary plasmonic nanostructures. *Opt. Express* **2012**, *20* (7), 6968–6973.

(197) Nicoletti, O.; Wubs, M.; Mortensen, N. A.; Sigle, W.; van Aken, P. A.; Midgley, P. A. Surface plasmon modes of a single silver nanorod: an electron energy loss study. *Opt. Express* **2011**, *19* (16), 15371–15379.

(198) Cubukcu, E.; Capasso, F. Optical nanorod antennas as dispersive one-dimensional Fabry-Ṕrot resonators for surface plasmons. *Appl. Phys. Lett.* **2009**, *95* (20).

(199) Martin, J.; Kociak, M.; Mahfoud, Z.; Proust, J.; Gérard, D.; Plain, J. High-Resolution Imaging and Spectroscopy of Multipolar Plasmonic Resonances in Aluminum Nanoantennas. *Nano Lett.* **2014**, *14* (10), 5517–5523.

(200) Saito, H.; Kurata, H. Direct measurement of dispersion relation for surface plasmon-polaritons on silver nanoantennas. *Microscopy* **2014**, *63* (2), 155–159.

(201) N'Gom, M.; Ringnalda, J.; Mansfield, J. F.; Agarwal, A.; Kotov, N.; Zaluzec, N. J.; Norris, T. B. Single Particle Plasmon Spectroscopy of Silver Nanowires and Gold Nanorods. *Nano Lett.* **2008**, *8* (10), 3200–3204.

(202) N'Gom, M.; Li, S.; Schatz, G.; Erni, R.; Agarwal, A.; Kotov, N.; Norris, T. B. Electron-beam mapping of plasmon resonances in electromagnetically interacting gold nanorods. *Phys. Rev. B - Condens. Matter Mater. Phys.* **2009**, *80* (11).

(203) Ditlbacher, H.; Hohenau, A.; Wagner, D.; Kreibig, U.; Rogers, M.; Hofer, F.; Aussenegg, F. R.; Krenn, J. R. Silver nanowires as surface plasmon resonators. *Phys. Rev. Lett.* **2005**, *95* (25).

(204) Chu, M.-W.; Myroshnychenko, V.; Chen, C. H.; Deng, J.-P.; Mou, C.-Y.; García de Abajo, F. J. Probing Bright and Dark Surface-Plasmon Modes in Individual and Coupled Noble Metal Nanoparticles Using an Electron Beam. *Nano Lett.* **2009**, *9* (1), 399–404.

(205) Flannigan, D. J.; Barwick, B.; Zewail, A. H. Biological imaging with 4D ultrafast electron microscopy. *Proc. Natl. Acad. Sci. U. S. A.* **2010**, *107* (22), 9933–9937.

(206) Schider, G.; Krenn, J. R.; Hohenau, A.; Ditlbacher, H.; Leitner, A.; Aussenegg, F. R.; Schaich, W. L.; Puscasu, I.; Monacelli, B.; Boreman, G. Plasmon dispersion relation of Au and Ag nanowires. *Phys. Rev. B* **2003**, *68* (15), 155427.

(207) Schaich, W. L.; Schider, G.; Krenn, J. R.; Leitner, A.; Aussenegg, F. R.; Puscasu, I.; Monacelli, B.; Boreman, G. Optical resonances in periodic surface arrays of metallic patches. *Appl. Opt.* **2003**, *42* (28), 5714–5721.

(208) Dorfmüller, J.; Vogelgesang, R.; Weitz, R. T.; Rockstuhl, C.; Etrich, C.; Pertsch, T.; Lederer, F.; Kern, K. Fabry-Pérot Resonances in One-Dimensional Plasmonic Nanostructures. *Nano Lett.* **2009**, *9* (6), 2372–2377.

(209) Draine, B. T.; Flatau, P. J. Discrete-Dipole Approximation For Scattering Calculations. *J. Opt. Soc. Am. A* **1994**, *11* (4), 1491.

(210) Purcell, E. M.; Pennypacker, C. R. Scattering and Absorption of Light by Nonspherical Dielectric Grains. *Astrophys. J.* **1973**, *186*, 705.

(211) Bigelow, N. W.; Vaschillo, A.; Iberi, V.; Camden, J. P.; Masiello, D. J. Characterization of the Electron- and Photon-Driven Plasmonic Excitations of Metal Nanorods. *ACS Nano* **2012**, *6* (8), 7497–7504.

(212) Bigelow, N. W.; Vaschillo, A.; Camden, J. P.; Masiello, D. J. Signatures of Fano Interferences in the Electron Energy Loss Spectroscopy and Cathodoluminescence of Symmetry-Broken Nanorod Dimers. *ACS Nano* **2013**, *7* (5), 4511–4519.

APPENDIX

Appendix A

List of Publications

1. **R. Collette**, D. A. Garfinkel, Z. Hu, D. J. Masiello, P. D. Rack, *Near Field Excited State Imaging via Stimulated Electron Energy Gain Spectroscopy of Localized Surface Plasmon Resonances in Plasmonic Nanorod Antennas*, Sci. Rep. (Submitted January 2020)
2. M.E. Moore, C. Delzer, J Watts, B.L. Muscicó, C. Xu, **R.M. Collette**, P.D. Rack, Y. Zhang, C.L. Melcher, S. McConchie, J.P. Hayward, *Studying the effects of thermally diffusing Ce into the surface of $YAlO_3$ for Associated Particle Imaging*, Nuclear Inst. and Methods in Physics Research, B (Accepted March 2020).
3. K. Aleshire, I. M. Pavlovetc, **R. Collette**, X.-T. Kong, P. D. Rack, S. Zhang, D. J. Masiello, J. P. Camden, G. V. Hartland, M. Kuno, *Far-Field Mid-Infrared Imaging and Spectroscopy of Single High Aspect Ratio Gold Nanowires*, Proc. Natl. Acad. Sci., Vol 117, no 5, pp 2288-2293 (February 2020)
4. K.C. Smith, A. Olafsson, X. Hu, S.C. Quillin, J.C. Idrobo, **R. Collette**, P.D. Rack, J.P. Camden, D.J. Masiello, *Direct Observation of Infrared Plasmonic Fano Antiresonances by a Nanoscale Electron Probe*, Physical Review Letters, Vol. 123, no. 17, pp 177401 (August 2019).
5. **R. Collette**, Y. Wu, P.D. Rack, *Correlating the Optical Property Evolution in the Au-Ni Binary Thin Films: From Metastable Solid Solution to Phase Separated Alloy*, J. Alloy Compd. Vol. 793, pp 695-704 (April 2019).
6. **R. Collette**, Y. Wu, A. Olafsson, J.P. Camden, P.D. Rack, *Combinatorial Thin Film Sputtering Au_xAl_{1-x} Alloys: Correlating Composition and Structure with Optical Properties*, ACS Comb. Sci., Vol. 20, no 11, pp 633-642 (October 2018).
7. D. Rutstrom, **R. Collette**, L. Stand, M. Loyd, Y. Wu, M. Koschan, C.L. Melcher, M. Zhuravleva, *Investigating new activators for small-bandgap LaX_3 (X = Br, I) scintillators*, Journal of Crystal Growth, Vol 483, pp 251-257 (December 2017).
8. N. Reynolds, J. Priyamvada, J.T. Heron, C.L. Jermain, J, Gibbons, **R. Collette**, R.A. Buhrman, D.G. Schlom, D.C. Ralph, *Spin Hall torques generated by rare-earth thin films*, Phys. Rev. B, Vol. 95, no 6, pp 064412 1-12 (February 2017).

VITA

Robyn Marie Collette was born in 1994 in New Brunswick, NJ to the parents John and Lisa Collette. She was raised by her parents in Bethlehem, PA with her sister and brother, Samantha and Cory. She obtained her B.S. degree in Physics with a certificate in Nanofabrication Manufacturing Technology from Shippensburg University of Pennsylvania in 2016. Throughout her undergraduate studies, Robyn worked with Dr. Kathryn Shirk on 3D printed microfluidic devices and was a research intern with the National Nanotechnology Infrastructure Network at Cornell University. Robyn pursued her Ph.D. in Materials Science and Engineering at The University of Tennessee, mentored by Dr. Philip D. Rack and graduated in August of 2020. Robyn's research interests during her graduate career centered on novel plasmonic materials and stimulated electron energy gain of plasmonic nanostructures.